2020-06-16

Performance of a full-scale Rammed Aggregate Pier group in silty sand based on blast-induced liquefaction testing in Emilia-Romagna, Italy

Paul Joseph Walsh Andersen
Brigham Young University

Performance of a Full-Scale Rammed Aggregate Pier Group in Silty Sand Based on Blast-Induced Liquefaction Testing in Emilia-Romagna, Italy

Paul Joseph Walsh Andersen

A thesis submitted to the faculty of
Brigham Young University
in partial fulfillment of the requirements for the degree of

Master of Science

Kyle M. Rollins, Chair
Norman L. Jones
Gus P. Williams

Department of Civil and Environmental Engineering

Brigham Young University

ABSTRACT

Performance of a Full-Scale Rammed Aggregate Pier Group in Silty Sand
Based on Blast-Induced Liquefaction Testing
in Emilia-Romagna, Italy

Paul Joseph Walsh Andersen
Department of Civil and Environmental Engineering, BYU
Master of Science

To investigate the liquefaction mitigation capability of Rammed Aggregate Piers® (RAP) in silty sand, blast liquefaction testing was performed at a soil profile treated with a full-scale RAP group relative to an untreated soil profile. The RAP group consisted of 16 piers in a 4x4 arrangement at 2 m center-to-center spacing extending to a depth of 9.5 m. Blasting around the untreated area induced liquefaction ($r_u \approx 1.0$) from 3 m to 11 m depth, producing several large sand boils, and causing settlement of 10 cm. In contrast, installation of the RAP group reduced excess pore water pressure ($r_u \approx 0.75$), eliminated sand ejecta, and reduced average settlement to between 2 to 5 cm when subjected to the same blast charges. Although the liquefaction-induced settlement in the untreated area could be accurately estimated using the CPT-based settlement approach proposed by Zhang et al. (2002), settlement in the RAP treated area was significantly overestimated with the same approach even after considering RAP treatment-induced densification. Analyses indicate that settlement after RAP treatment could be successfully estimated from elastic compression of the sand and RAP acting as a composite material. The composite reinforced soil mass, surrounded by liquefied soil, transferred load to the base of the RAP group inducing settlement in the non-liquefied sand below the group. This test program identifies a mechanism that explains how settlement was reduced for the RAP group despite the elevated r_u values in the silty sands that are often difficult to improve with vibratory methods.

Keywords: Rammed Aggregate Piers®, silty sand, liquefaction, liquefaction mitigation, liquefaction-induced settlement, blast-induced liquefaction

ACKNOWLEDGEMENTS

Financial support for this study was primarily provided by Geopier® Foundation Company (Davidson, North Carolina, United States) along with local affiliate Releo s.r.l. (Ferrara, Italy) who provided the installation of the Rammed Aggregate Piers free of charge. In addition, funding for my support was provided by an REU supplement to grant CMMI-1663288 from the National Science Foundation. I would like these sponsors to know that their contributions are gratefully acknowledged. However, the opinions, conclusions and recommendations in this paper do not necessarily represent those of the sponsors. From the Italian side, additional funding was provided by INGV-FIRB Abruzzo project ("Indagini ad alta risoluzione per la stimadella pericolosità e del rischio sismico nelle aree colpite dal terremoto del 6 aprile 2009", http://progettoabruzzo.rm.ingv.it/it), by the INGV-Abruzzo Region project ("Indagini di geologia,sismologia e geodesia per la mitigazione del rischio sismico", L.R. n. 37/2016), and by the CIRI Edilizia e Costruzioni, University of Bologna, Italy (TIRISICO PROJECT "Tecnologie Innovative per la riduzione del rischio sismico delle Costruzioni", Project no. PG/2015/ 737636, POR-FESR 2014-2020). I also express our appreciation to the Bondeno Municipality and to the Emilia-Romagna Region who provided all the necessary support to realize the research in collaboration with the other local authorities (Ferrara Prefecture, Ferrara Province, Local Civil Protection, Police).

I would like to acknowledge the National Institute of Geophysics and Volcanology in L'Aquila, Bologna, and Rome for their invaluable help in instrumenting the site. Brigham Young University for contributing technical equipment to monitor the blast test. Scan&Go srl provided the TLS surveying.

I would like to especially thank all of the technicians from the different universities and companies with which we labored in the field (Dave Anderson, Mario Marcolongo, Alessandro Lodi, Giovanni Bianchi, Gianni Petitti, Luigi Antonetti, Cristiano Prosperi, and all others who contributed). Thank you for your help, as well as your friendship. Those days in the field are cherished memories. Thank you also to Jared Baxter for your technical assistance.

I wish to express my deepest appreciation and gratitude towards Dr. Kyle M. Rollins and his family. It is thanks to Dr. Rollins that I even considered the possibility of continuing beyond my undergraduate education at Brigham Young University. I will always appreciate his invitation to continue that journey. The Ralph Rollins scholarship that his family provided is a treasured gift that enabled me and my family to continue my education. More importantly, I will forever be grateful for the chance to have worked with Dr. Rollins and the inspiring people with which he associates in the field of geotechnical engineering around the world. To associate with, and work with them has been an invaluable experience.

I owe a deep debt of gratitude to Dr. Sara Amoroso from the Università degli Studi G. d'Annunzio Chieti e Pescara. Dr. Amoroso was the maestro of the research project in Bondeno and its successful realization is thanks to her vision and leadership. I am grateful to have collaborated with such a well-respected, distinguished, and driven geotechnical researcher as herself.

I wish to express my gratitude to the graduate committee and department staff at Brigham Young University. I am grateful for their instruction and assistance in producing this thesis. My thanks are also extended to the previous students of Dr. Rollins whose work I follow.

Finally, I would like to thank my family for their unceasing support and encouragement. My wife for supporting me through my education, and for sharing this vision with me.

TABLE OF CONTENTS

LIST OF TABLES

LIST OF FIGURES

1 INTRODUCTION

Much has been learned about the phenomenon of liquefaction produced by earthquake events in the past 50 years. This phenomenon has demanded the attention of researchers during this time because it has caused substantial damage to infrastructure in many recorded earthquake events. This damage is often extensive and costly. During the 2010 to 2011 Canterbury Earthquake Sequence (CES) the city of Christchurch, New Zealand suffered liquefaction-induced damage to 51,000 residential properties, with approximately 15,000 residential houses damaged beyond repair (Wissmann et al., 2015). The 1989 Loma Prieta, California, earthquake ($M_w = 6.9$) is one of the costliest disasters in U.S. history, and resulted in estimated losses between US $7 and $9 billion. Liquefaction-induced settlements caused service outages of important lifelines such as sewer, water, and natural gas, damage to airport runways and city streets, and destruction of buildings. Further damage was incurred by several fires within the city's Marina district that could not be put out because of the water outages (Seed et al., 1991).

The potential for enormous damage and loss of life in seismic events motivates continuous study of ground improvement. Soil improvement techniques are commonly used at sites where the existing soil conditions are expected to lead to unsatisfactory performance. Many soil improvement techniques have been invented in an attempt to reduce the effects of liquefaction and

to conserve infrastructure. While ground improvement is not necessarily a new field of study, many new techniques are being invented and are often used in practice before a full academic understanding of their improvement mechanisms is known. This thesis will investigate the mechanics of improvement for one technique known as Rammed Aggregate Piers®, which was originally developed by Geopier Foundation Company® in 1989. This system has been used in practice to effectively mitigate liquefaction effects, yet there is still much to be learned about the increases in liquefaction resistance produced by increased lateral pressure during RAP installation, soil densification, reduced excess pore pressure generation, and increases in stiffness from soil and RAP composite response.

1.1 Objectives

Much empirical evidence exists to confirm the effectiveness of RAP in coarse-grained soils. Less research is available to demonstrate their effectiveness in fine-grained soil types. Generally, densification techniques are less effective as fines content increases. As such, this thesis aims to uncover the mechanism of improvement by RAP groups in sandy soils with higher fines content. The key objectives are listed below:

1. Investigate the ability of RAP groups to reduce the liquefaction potential of silty sand.
2. Determine the ability of RAP groups to prevent liquefaction-induced settlement in silty sands.
3. Improve understanding of the mechanisms involved in reducing liquefaction-induced settlement around RAP groups.

4. Develop a reliable, simple, and accurate settlement model that can provide realistic estimates to observed behavior.

1.2 Scope of work

To further investigate the potential of RAP columns to mitigate liquefaction hazard in silty sands, a full-scale test was performed in Bondeno, Italy, in conjunction with the National Institute of Geophysics and Volcanology in Italy (INGV). A site was chosen based on liquefaction observation from previous seismic events and the soil profile consisted of a clay to a depth of 3.4 m underlain by liquefiable sand and sandy silt. A four by four quadrangular grid of rammed aggregate piers was installed to a depth of approximately 9.5 m. The 0.5 m diameter piers were spaced at 2 m center-to-center, creating a replacement ratio (the ratio of pier area to the tributary soil area surrounding the pier) equal to 5%. A profilometer was installed in the center of the RAP grid in order to record settlement with depth. Surface stakes were installed across the test site to record settlements in the improved and natural panels. Surface settlements were further verified by Terrestrial Laser Scanning (TLS) and aerial photogrammetry. Pore pressure transducers were placed at various depths to monitor the liquefaction effects on the subsurface profile. Additionally, accelerometers were installed at 3.5 and 4.5 m to record blast data.

The liquefiable target layers at the test site in Bondeno contain higher fines content than other tests conducted on RAP columns. This experiment will further investigate the influence of soil densification, increased lateral earth pressures and increased profile stiffness from composite action on liquefaction resistance.

1.3 Statement of organization

This thesis presents the details regarding the development of the case study, actions to execute the test, and results and conclusions from the data obtained. The reminder of the thesis consists of 9 chapters. Chapter 2 explains the current research in the area of liquefaction effects on deep foundations and gives sufficient background to the conceptual behavior. Chapter 3 describes methodologies typically used to mitigate against liquefaction. This chapter also describes the process of RAP installation and treatment mechanics in depth. Chapter 4 describes the preliminary investigations and analysis to determine the optimal site for the test in Bondeno, Italy. Chapter 5 summarizes the site-specific installation details of the RAP installation. Chapter 6 offers details regarding the blast test procedure and instrumentation of the site. Chapter 7 describes the results from the blast test with respect to measured pore pressures, observed sand ejecta, measured settlements on the ground surface and with depth, as well as recorded accelerograms from blasting. Chapter 8 analyzes the results of blast-induced liquefaction with respect to settlements with depth, and the effects of lateral earth pressures. This chapter also examines the accelerogram data and attempts to use accelerations to estimate induced shear stresses and strains. Chapter 9 is a summary of the completed work and presents conclusions and areas of future research around these topics.

2 LIQUEFACTION

2.1 Introduction to liquefaction

Liquefaction is a broadly defined phenomenon that involves the reduction of stiffness and strength of a soil when excess pore water pressure builds up due to monotonically or cyclically applied strains to saturated cohesionless soil (Castro, 1969). As the pore water pressure increases, the soil structure collapses, and the soil starts to behave as a liquid. The rearrangement of soil particles results in a loss of effective stress and a decrease in shear strength due to the generation of excess pore water pressure (Narin van Court, 1997). Water pressure in the pore space of soil is directly correlated to the effective stress in cohesionless soil by the following equation:

$$\sigma'_v = \sigma - u_o \tag{2.1.1}$$

where σ'_v is effective stress, σ is total stress and u_o is pore pressure. As pore pressures increase, the effective strength of the soil decreases. When the pore pressure equals the confining stress, liquefaction is triggered. Studer and Kok (1980) have demonstrated that at pore pressure ratios of 80% confining stress liquefaction is incipient. Liquefaction phenomena that result from this process are divided into two main groups: *flow liquefaction* and *cyclic mobility* (Kramer, 1996).

Flow liquefaction occurs when the shear strength of the soil required to maintain static equilibrium is less than the existing static shear stress condition. Cyclic strains, or shock loading can temporarily reduce the shear strength of a soil mass and therefore cause flow liquefaction

failure. In the case of flow liquefaction failure, the applied shear strains will cause continuous deformations in the soil until the applied shear stresses are reduced to a level less than the viscous shear resistance of the liquefied material, or until dilatant action of the soil can arrest flow (Youd, 1973). Flow liquefaction is the responsible mechanism for breathtaking and devastating slope failures such as the 2010 landslide in the Calabrian town of Maierato, Italy, and the Fort Peck Dam in 1938.

Cyclic mobility is another liquefaction phenomenon that differs from flow liquefaction in that its occurrence is brought about when the static shear stress is less than the shear strength of the liquefied soil. The deformations are instead caused by a combination of static shear stresses, and cyclic shear stresses that develop incrementally during earthquake shaking (Kramer, 1996). Cyclic mobility can occur even on flat ground, and when this happens it is termed *level-ground liquefaction.* During level-ground liquefaction little to no lateral soil movement occurs, but as the cyclically induced pore pressures later dissipate, the soil experiences volumetric shrinkage which is manifested on the ground surface as settlement (Ishihara and Yoshimine, 1992).

The loss of effective strength and the settlements associated with dissipating pore pressures are primary causes of foundation failure and costly damages to structures and lifelines during liquefaction events. In 1964 two significant earthquake events led to the concentrated study of liquefaction behavior and its mollification. The first earthquake, known as the Great Alaskan earthquake (M_w = 9.2), occurred on Good Friday, March 27. The second earthquake occurred on June 16 in Niigata, Japan (M_w = 7.5). Both earthquake events caused heartbreaking deaths and expensive damages to structures and lifelines. These two earthquakes also provided evidence of liquefaction, such as landslides (flow liquefaction failure), and post-liquefaction settlement (cyclic mobility), among others. Much research has been performed since the mid-1960s to better

understand liquefaction. The interested reader may see Kramer (1996) for an in-depth summary of fundamental liquefaction behavior. His work provides a systematic approach that should be considered when evaluating liquefaction and its potential hazards. This systematic approach considers liquefaction susceptibility, liquefaction initiation, and liquefaction effects. Excerpts from his approach that pertain to level-ground liquefaction, or cyclic mobility, which is the subject of this thesis, will be shared.

Figure 2.1: Anchorage Alaska 1964 Earthquake. Right – Niigata Japan 1964 Earthquake (After Kramer, 1996).

2.2 Liquefaction susceptibility

Not all soils are liquefiable. In order to efficiently analyze liquefaction hazards it is important for geotechnical engineers to be able to determine if liquefaction is possible at a given site. If liquefaction is not possible at a given site, then the effects of liquefaction do not need to be considered in the engineered design. Kramer (1996) identifies several criteria by which susceptibility can be determined. These include historical, geologic, compositional, and state criteria.

Historical liquefaction criterion respect that soils that have liquefied in the past are certainly susceptible to liquefy again. A study by Youd (1984) shows that a soil that has liquefied previously is likely to liquefy again if soil and groundwater conditions remain unchanged. Historical records of liquefaction have been used to create maps of susceptible areas. Characteristics from liquefied soils can also be tabulated and used to determine susceptibility of other areas possibly prone to liquefaction. Researchers often use historical evidence of liquefaction to guide their selection of experimental test sites (Amoroso et al, 2018).

Only a narrow range of geologic environments will produce liquefiable soils (Youd, 1991). Liquefaction susceptibility is determined by the environment in which the soil was deposited, the hydrological conditions, and the age of the soil (Youd and Hoose, 1977). Alluvial, fluvial, and aeolian stratigraphic deposits have high liquefaction potential, because these soils were deposited in a loose state. For similar reasons, shallow (usually less than 15m deep) saturated soils with a young geologic age (deposited < 10,000 years ago), are susceptible. Since liquefaction is dependent on pore water pressure the susceptibility of liquefaction decreases with increasing groundwater table depth. Kramer (1996) points out that human-made soil deposits deserve consideration. Loose fills, such as those placed without compaction, are very likely susceptible to liquefaction.

Since pore pressure is directly related to volumetric change, the compositional characteristics associated with high volume change potential tend to be associated with high liquefaction susceptibility (Kramer, 1996). Low angularity, poor-gradation, and uniform grain size are positively correlated to liquefaction susceptibility. Initially it was believed that only sands were liquefiable. Over time research has shown that gravels and non-plastic silts are also capable of liquefaction (Ishihara, 1984, 1985, 1993; Coulter and Migliaccio, 1966; Chang, 1978; Wong,

1984). As a general rule liquefaction susceptibility increases with grain size uniformity and decreases with fines content and grain angularity.

Perhaps the most important determinant of liquefaction susceptibility is the state criteria of the soil. The initial state criteria consider the relationship between the effective confining stress, and the density of the soil. There are direct correlations between these parameters and the liquefaction susceptibility of a given soil.

2.3 Evaluation of initiation of liquefaction

In practicality, the amount of methods by which engineers and researchers assess site risks due to liquefaction is expanding, particularly as improvements are made in site exploration technologies. However, two main methods persist and will be discussed in this thesis: the *cyclic strain* and *cyclic stress* approaches.

Between these two approaches, the cyclic strain approach may be more theoretically correct. Research has shown that densification of dry sands is controlled by cyclic strains rather than cyclic stresses (Silver and Seed, 1971; Youd, 1972). Furthermore, the tendency of dry sands to densify is directly correlated with the generation of excess pore pressure when saturated, and therefore pore pressure generation is more related to cyclic strains than cyclic stresses (Kramer, 1996). The cyclic strain approach is considered reliable in that its predictions are insensitive to parametric changes other than cyclic strain amplitude. By this method, the cyclic strain during an earthquake is approximated by the following equation:

$$\gamma_{cyc} = 0.65 \frac{a_{max}}{g} \frac{\sigma_v r_d}{G(\gamma_{cyc})} \tag{2.3.1}$$

where a_{max} is the peak ground acceleration during the design earthquake, g is gravity, r_d is the stress reduction coefficient that accounts for the dynamic response of the soil profile, and $G(\Upsilon_{cyc})$ is the shear modulus of the soil at the given strain magnitude. As Υ_{cyc} influences both sides of the equation, its value must be determined iteratively from a measured G_{max} profile and appropriate modulus reduction curves (Kramer, 1996). Once Υ_{cyc} is determined it is compared with the threshold shear strain, that is, the shear strain corresponding to initiation of interparticle sliding. If the cyclic strain is greater than this threshold strain, liquefaction is possible and liquefaction resistance must be evaluated. While theoretically well founded, the cyclic strain approach is less commonly used by practicing engineers due to the difficulty in approximating cyclic strain. Since it is less commonly used in practice, this thesis will not explore the methods for estimating liquefaction resistance by this model, however, they can be further explored in the works of Dobry and Ladd, 1980; Dobry et. al, 1982; Dobry et al., 1984; and Vasquez-Herrera and Dobry, 1988.

The cyclic stress approach is the more commonly used approach in conducting a liquefaction initiation analysis. This approach compares with depth the cyclic shear stresses created by earthquake-induced loading, τ_{cyc}, (also called cyclic stress ratio, or CSR), and the liquefaction resistance of the soil, $\tau_{cyc,L}$ (also called cyclic resistance ratio, or CRR), which is the stress required to generate liquefaction within the profile. Liquefaction is anticipated at depths where the applied stress is greater than the resistance. The end result of this approach is a factor of safety against liquefaction which is calculated by dividing the resistance provided by the soil by the stress induced by the cyclic loading. A factor of safety less than or equal to one would indicate that liquefaction is likely to initiate under the designed conditions.

$$FS_L = \frac{\tau_{cyc,L}}{\tau_{cyc}} = \frac{CRR}{CSR} \tag{2.3.2}$$

Unlike the cyclic strain approach, the cyclic stress approach attempts to relate excess pore pressure with cyclic stresses instead of cyclic strains. While not as theoretically accurate, the relationship between cyclic stress and excess pore pressure is strong enough that good approximations can be made. At one point in time the shear stress required to trigger liquefaction was estimated from laboratory testing by subjecting specimens to uniform harmonic loading. During this period the only factors considered in liquefaction analysis were initial density and initial stress conditions. With time it was observed that many other factors affect liquefaction potential, such as: differences in soil structure produced by different methods of specimen preparation (Ladd, 1974; Mulilis et al., 1975; Toki et al., 1986; Tatsuoka et al., 1986); the history of prior seismic straining (Finn et al., 1970; Seed et al., 1975); overconsolidation ratio and lateral earth pressure coefficient (Seed and Peacock, 1971); length of time under sustained pressure (Ohsaki, 1969; Seed, 1979; Yoshimi et al., 1989). Furthermore, the correlations between unidirectional harmonic load testing in the laboratory and excess pore pressure ratio do not accurately reflect the pore pressure generated during multi-directional loading that occurs during seismic sequences (Seed et al., 1975). Due to the difficulty of characterizing liquefaction resistance by laboratory methods, other in-situ methods were eventually developed and are the primary basis for correlations today.

In 1971, Whitman described that liquefaction case histories could be used to characterize liquefaction resistance in terms of measured in-situ parameters. From this time forward in-situ testing processes have greatly developed and liquefaction characterization methods have been created for a variety of in-situ techniques, such as: cone penetration test (CPT) (Robertson, 2004, 2007, 2009; Robertson and Wride, 1998; Idriss and Boulanger, 2008; Olsen, 1997; Suzuki et al., 1995), shear wave velocity (Sykora, 1987; Kayen et al., 1992; Robertson et al., 1992; Andrus and

Stokoe, 1997, 2000; Andrus et al., 2004), dilatometer (DMT) index (Marchetti, 1982; Robertson and Campanella, 1986; Reyna and Chameau, 1991; Tsai et al., 2009), and standard penetration test (SPT) (Seed and Idriss, 1971, 1982; Seed et al., 1983; Seed et al., 1985; Cetin et al, 2004; Idriss and Boulanger, 2004, 2010, 2014). In many respects, the SPT approach is being overtaken by the more reliable CPT test, however the SPT approach remains popular in present practice. Correlations between CPT and SPT also allow for substitutions of parameters from either test into approximations (Robertson and Campanella, 1983). At the test site in Bondeno, Italy, in-situ explorations were primarily obtained using CPT and DMT, with liquefaction analysis being performed using CPT methods. As such, only the CPT method presented by Youd et al. (2001) will be discussed in this presentation.

The CPT test correlates well with liquefaction resistance since the factors that increase liquefaction resistance (e.g. density, prior seismic straining, overconsolidation ratio, lateral earth pressures, non-uniformity, and time under sustained pressure) also tend to increase CPT cone tip resistance (Kramer, 1996). Furthermore, the nearly continuous nature of the CPT sounding provides a more detailed estimation of liquefiable layers. As described by Youd et al. (2001) at the NCEER workshop on liquefaction resistance of soils, this stratigraphic capability of CPT makes it a particularly advantageous tool for determining liquefaction-resistance. In 1998, Robertson and Wride prepared curves (shown in Figure 2.2) for the direct determination of CRR for clean sands (FC≤5%) from case history CPT data obtained from several investigations. Figure 2.2 plots the normalized cone tip resistance against known values of CSR or CRR for case histories of magnitude 7.5 earthquakes, and depicted the line of separation between data indicative of liquefaction and nonliquefaction. Figure 2.2 provides the CRR against earthquakes of M_w =7.5 only, to obtain the CRR for earthquakes of different magnitude the additional application of a

magnitude scaling factor (MSF) must be applied. The MSF will be discussed in further detail in a later paragraph.

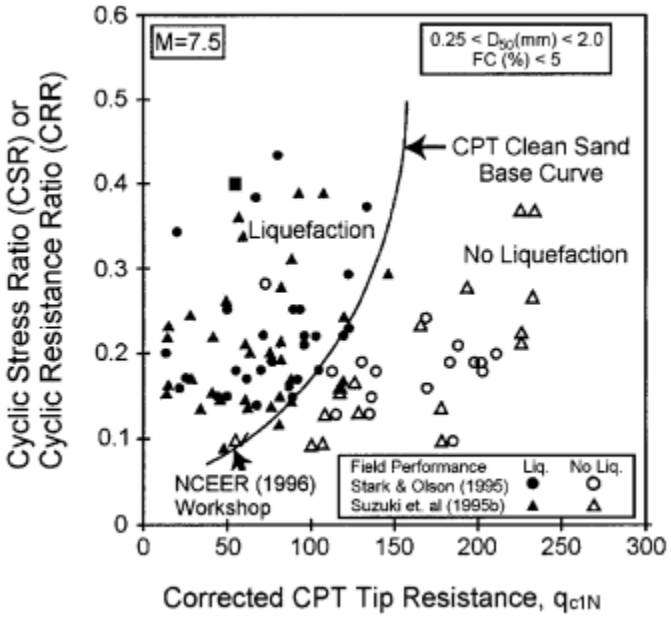

Figure 2.2: Curve recommended for calculation of CRR from CPT data along with liquefaction data compiled case histories (after Youd et al, 2001).

The clean-sand based curve from Figure 2.2, or rather, the CRR for M_w =7.5 ($CRR_{7.5}$), is given by the following equation(s):

$$if\ (q_{c1N})_{cs} < 50\ \ CRR_{7.5} = 0.833\left[\frac{(q_{c1N})_{cs}}{1000}\right] + 0.05 \tag{2.3.3}$$

$$if\ 50 \leq (q_{c1N})_{cs} < 160\ \ CRR_{7.5} = 93\left[\frac{(q_{c1N})_{cs}}{1000}\right]^3 + 0.08 \tag{2.3.4}$$

Where $(q_{c1N})_{cs}$ is the clean-sand cone penetration resistance normalized to approximately 100 kPa (1 atm).

The procedure for obtaining $(q_{c1N})_{cs}$ is comprised of several steps and is provided by Robertson and Wride (1998). The process is summarized as follows. First, the cone tip resistance

is normalized to one atmosphere of pressure, thus yielding a dimensionless cone penetration resistance, q_{c1N}.

$$q_{c1N} = C_Q(\frac{q_c}{P_a}) \tag{2.3.5}$$

where

$$C_Q = (\frac{P_a}{\sigma'_{v0}})^n < 1.7 \tag{2.3.6}$$

and where C_Q is the normalizing factor for cone penetration resistance, P_a is one atm of pressure in the same units as σ'_{v0}, n is an exponent that varies with soil type, and q_c is cone penetration resistance.

As discussed previously, the fines content and plasticity of soil greatly influence its liquefaction potential. This CPT method accounts for this by using the Robertson and Wride (1998) approach to estimating soil type by using cone tip resistance, q_c, and sleeve friction, f_s. The ratio of f_s/q_c is labeled the soil behavior type index, I_c, and can be used to account for effects of soil characteristics on q_{c1N} and CRR. I_c is especially useful because its value represents a concentric circle that serves as the boundary between different soil types. The different soil type zones presented by Robertson and Wride (1998) are shown in Figure 2.3. The soil behavior type index, I_c is computed as an intermediate step in determining $(q_{c1N})_{cs}$. I_c in general is computed using the following equations:

$$I_c = [(3.47 - \log(Q))^2 + (1.22 + \log(F))^2]^{0.5} \tag{2.3.7}$$

$$Q = \left[\frac{q_c - \sigma_{v0}}{P_a}\right][\frac{P_a}{\sigma'_{v0}}]^n \tag{2.3.8}$$

$$F = \left[\frac{f_s}{q_c - \sigma_{v0}}\right]X100\% \tag{2.3.9}$$

where Q is the dimensionless CPT tip resistance, F is the normalized friction ratio, q_c is CPT tip resistance, σ_{v0} is total vertical stress, P_a is 1 atm of pressure in the same units as σ, σ'_{v0} is vertical effective stress, and n is a stress exponent related to soil type. The plot in Figure 2.3 is developed assuming a value of 1.0 for n.

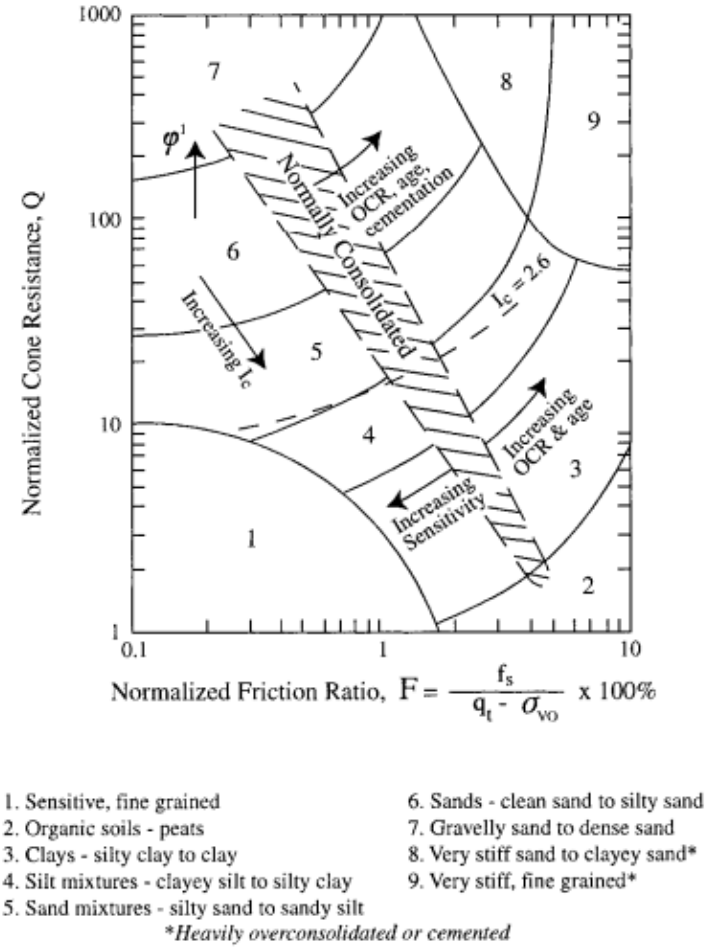

Figure 2.3: CPT-Based soil behavior type chart (after Youd et al, 2001).

Robertson and Wride (1998) recommend the following procedure for calculating I_c. The first step is to differentiate between clay type soils and sands or silts. This is done by first computing the dimensionless CPT tip resistance, Q, using a stress exponent of 1.0. If the resulting I_c value is > 2.6 the soil is classified as clayey and is considered too clay-rich to liquefy, and the

liquefaction susceptibility analysis is complete (Youd et al, 2001). The NCEER workshop guidelines specify that soils with high fines content should still be sampled and that liquefaction susceptibility should be verified using the criteria known as the 'Chinese' criteria which are defined by Seed and Idriss (1982). These criteria specify that liquefaction can only occur if the following three criteria are met: 1) the clay content is <15% by weight, 2) the liquid limit < 35%, 3) The in-situ moisture content > 0.9 times the liquid limit.

If, however, the resulting $I_c < 2.6$ then the soil is likely coarse grained, and C_q and Q are recalculated using a stress exponent, n, of 0.5. If after this calculation $I_c < 2.6$ then the soil is classified as nonplastic and granular. For these soils, this value of I_c is used in liquefaction resistance calculations. If, however, the recalculated $I_c < 2.6$, then the soil is likely silty and possibly plastic, and hence, I_c should be calculated using the value of q_{c1N} from equation 2.5.5 using a stress exponent, n, of 0.7. For these soils, this value of I_c is used to compute liquefaction resistance.

Finally, the normalized penetration resistance (q_{c1N}) for silty sands is corrected to an equivalent clean sand value $(q_{c1N})_{cs}$ using the following equation:

$$(q_{C1N})_{cs} = K_c q_{c1N} \tag{2.3.10}$$

where K_c is a correction factor for grain characteristics. The K_c term is defined by the following equation (Robertson and Wride, 1998):

$$for\ I_c \leq 1.64\ \ K_c = 1.0 \tag{2.3.11}$$

$$for\ I_c > 1.64\ \ K_c = -.403{I_c}^4 + 5.581{I_c}^3 - 21.63{I_c}^2 + 33.75I_c - 17.88 \tag{2.3.12}$$

Once the appropriate I_c, K_c, and $(q_{c1N})_{cs}$ values are obtained the $CRR_{7.5}$ can be computed using equations 2.5.3 and 2.5.4. The computed $CRR_{7.5}$ can then be adjusted by a magnitude scaling

factor for magnitudes other than 7.5 (Youd et al, 2001). Several MSF have been proposed, although the one considered in this thesis was developed for sands by Idriss (1999). At the time of the NCEER workshop in 2001 this MSF method was still new enough that it was not recommended in the workshop procedures. Since that time the Idriss (1999) method has gained much popularity in practical use. The equation is as follows:

$$MSF = 6.9 * \exp\left(\frac{-M}{4}\right) - 0.058 \leq 1.8 \tag{2.3.13}$$

where M is the moment magnitude of the earthquake. It is important that if this MSF is used that an accompanying set of equations be used when computing the cyclic stress amplitudes applied to the soil. In addition to the MSF, two additional scaling factors are applied to the CRR, an overburden correction factor, K_σ, and a correction factor for sloping ground, K_α. Since the test taken place in this thesis occurred on level ground, the K_α factor was neglected. The K_σ can be estimated from the following equations (Boulanger and Idriss, 2014):

$$K_\sigma = 1 - C_\sigma \ln\left(\frac{\sigma_v'}{P_a}\right) \leq 1.1 \tag{2.3.14}$$

$$C_\sigma = \frac{1}{18.9 - 2.55\sqrt{(N_1)_{60cs}}} \leq 0.3 \tag{2.3.15}$$

where σ_{v0}' is the vertical effective stress, and P_a is the one-ton atmospheric overburden pressure (≈2000 psf, 100 kpa). The final CRR value for a given earthquake magnitude is then:

$$CRR = CRR_{7.5} * MSF * K_\alpha * K_\sigma \tag{2.3.16}$$

The uniform cyclic shear stress amplitude for level ground is estimated using the simplified procedure put forth by Seed and Idriss (1971):

$$\tau_{cyc} = 0.65 \frac{a_{max}}{g} \sigma_v r_d \tag{2.3.17}$$

where a_{max} is the peak ground surface acceleration, g is the acceleration of gravity, σ_v is the total vertical stress, and r_d is a stress reduction factor for the depth of interest. The r_d term was studied by Idriss (1999), who extended the work of Golesorkhi and Seed (1989), by performing hundreds of parametric site response analyses, and determined that r_d could be expressed by the following equations:

$$\ln(r_d) = \alpha(z) + \beta(z) * M_w \tag{2.3.18}$$

$$\alpha(z) = -1.012 - 1.126 \sin\left(\frac{z}{11.73} + 5.133\right) \tag{2.3.19}$$

$$\beta(z) = 0.106 + 0.118 \sin\left(\frac{z}{11.28} + 5.142\right) \tag{2.3.20}$$

where z is the depth below the ground surface in meters, M_w is the moment magnitude of the earthquake, and the arguments inside the terms are in radians. These equations are valid for depths ≤ 34 m. For depths greater than 34 m, the following equation must be used:

$$r_d = .12 \exp(0.22 M_w) \tag{2.3.21}$$

The final expression for CSR by the Seed and Idriss (1971) simplified procedure is:

$$CSR_{M_w=7.5} = \frac{CSR}{MSF} = \frac{\tau_{cyc}}{\sigma'_{v0}(MSF)} = 0.65 \frac{\sigma_{v0} * a_{max}}{\sigma'_{v0} * g} * \frac{r_d}{MSF} \tag{2.3.22}$$

The factor of safety against liquefaction can then be written as:

$$FS_L = \frac{CRR_{M_w=7.5}}{CSR_{M_w=7.5}} \tag{2.3.23}$$

Plotting the FS_L with depth, or the CSR and CRR with depth, provides a visual of where liquefaction is anticipated within the soil profile. An example of CSR vs CRR with depth is provided in Figure 2.4.

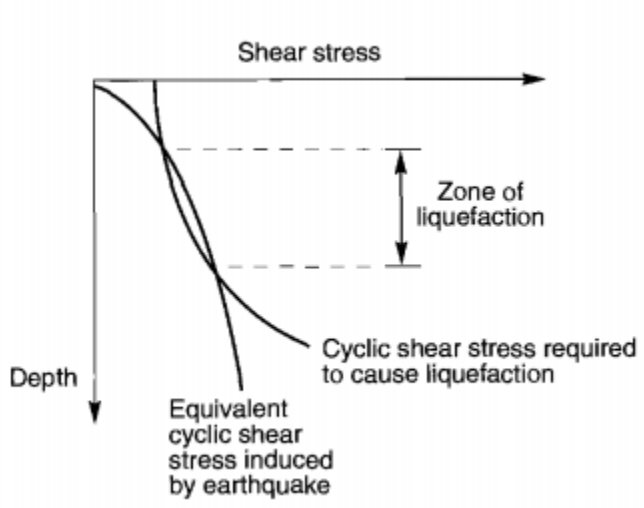

Figure 2.4: Plot of CSR vs CRR to determine zone of liquefaction with depth (After Kramer, 1996).

Approximations of FS_L have been correlated to excess pore pressure ratio, r_u, and these FS_L criteria can facilitate back-calculations where only pore pressure data is available. Several correlations have been proposed and are presented by Marcusson and Hynes (1990) in Figure 8.1. This figure provides engineers with a range of FS_L that varies with observed excess pore pressure generation. These correlations were integral to the post-processing work for this project.

A critical parameter to define for liquefied soils is the steady state strength, that is, the liquefied shear strength of the soil. Although of cardinal importance, the liquefied shear strength is difficult to obtain in practice. Three of the most general methods for its estimation are *laboratory techniques, in-situ techniques*, and *normalized strength techniques*.

The laboratory procedure for liquefaction evaluation outlines a series of five steps: i) Determine in-situ void ratio; ii) Determine steady-state void ratio, or density, as a function of effective stress using compacted specimens; iii) Determine undrained steady-state strengths for undisturbed specimens; iv) Correct measured undrained steady-state strengths to in-situ void ratio; v) Calculate in-situ driving shear stress and the factor of safety (Poulos et al., 1985). These steps represent a holistic approach to evaluating liquefaction potential, of which estimating the undrained steady state strength is but one step. These steps will not be further discussed in this thesis, though the reader is encouraged to reference the cited study for additional information.

In-situ methods are the most common way to estimate the residual undrained shear strength. In 1986 Seed suggested a method to back calculate the residual strength, S_r, from case histories of historical liquefaction, and to correlate S_r to equivalent clean sand SPT corrected blow counts $(N_1)_{60cs\text{-}Sr}$ (Seed, 1986). 18 case history sites were selected in this study, of which 13 had SPT data, while only four had available CPT data. As such, the correlation between S_r and SPT was first developed. Revisions were made to this method in a sequential study a few years later (Seed and Harder, 1990). The method requires that the soil have fewer than 10% fines content, or that the SPT blow count (N) value be corrected for fines. The corrected $(N_1)_{60\text{-}cs}$ is determined by summing the measured SPT blow count, corrected for hammer efficiency, $(N_1)_{60}$ value with the correction factor for fines content, N_{corr}. Values for N_{corr} have been suggested by Seed and Harder (1990), as well as Stark and Mesri (1992), and are given in Table 2.1. Once $(N_1)_{60\text{-}cs}$ is obtained the residual undrained shear strength can be estimated by Figure 2.5 proposed by Seed and Harder (1990). Correlations to S_r were then made using q_c as obtained by the CPT by way of converting to equivalent $(N_1)_{60\text{-}cs}$ (Idriss and Boulanger, 2007).

Table 2.1: Recommended fines correction for estimation of residual undrained shear strength by Seed-Harder and Stark-Mesri Procedures (After Kramer, 1996).

	N_{corr} (blows/ft)	
Percent Fines	Seed–Harder	Stark–Mesri
0	0	0
10	1	2.5
15	—	4
20	—	5
25	2	6
30	—	6.5
35	—	7
50	4	7
75	5	7

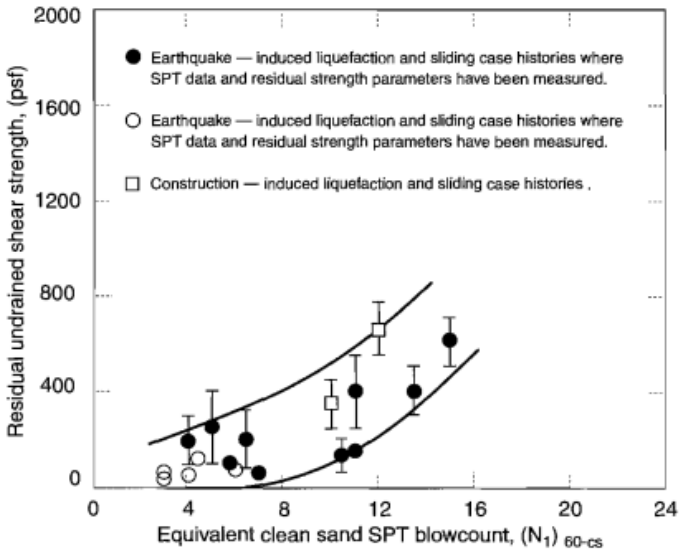

Figure 2.5: Correlation between $(N_1)_{60\text{-}cs}$ to residual undrained shear strength (After Seed and Harder, 1990).

Normalized strength methods allow for estimations of the residual undrained shear strength to be made from initial effective stresses. The theory is based on the premise that if, for a given soil, if the consolidation curve and the steady state line are parallel, then the steady state strength should be proportional to the consolidation stress (i.e., S_{su}/σ'_c = constant) (Kramer, 1996). A

number of studies found that if a specimen of soil could be prepared to resemble in-situ conditions and is tested in undrained shear, then the resulting residual strength ratio could be theorized to closely represent field conditions (Vasquez-Herrera et al., 1990; Baziar et al., 1992; Ishihara, 1993). Using this understanding Olson and Stark (2002) performed tests to back-calculate residual strength ratios from various case histories of flow liquefaction. They were able to generate an equation to relate the residual strength ratio (S_r) to SPT blow count. However, since large uncertainties are introduced into this method by the non-uniformity of a given sandy soil profile their correlation are only approximations and must be used with judgment.

With time research has continued to build upon engineers' ability to estimate the S_r for liquefied soils. In recent years more empirical relationships have been generated between the initial vertical effective stress and both the CPT q_c (Robertson, 1999; Olson and Stark, 2002), and the SPT $N1_{60}$ values (Idriss and Boulanger, 2007; Kramer and Wang, 2015; Olson, 2015). These relationships are consistent with behavior observed during laboratory testing, yet they are calibrated on the basis of back-calculated flow-slide case histories. Since the correlations are based on a limited number of case histories, the availability of multiple predictive models is of benefit to allow consideration of a variety of outcomes.

2.4 Liquefaction-induced settlement

When a $FS_L \leq 1$ liquefaction is expected, its effects must be considered in design. In the case study presented in this thesis, liquefaction (more correctly, cyclic mobility) was triggered in a level ground site with a silty sand and sandy silt profile to measure the effectiveness of a proprietary ground improvement technique, which will be discussed in a later section. Successful liquefaction mitigation was measured by considering the reductions of post-liquefaction settlement

and excess pore pressure generation. Settlement due to cyclic mobility can occur in both dry and saturated sands, though in this thesis only the saturated case will be examined. After porewater pressures dissipate the soil particles rearrange themselves into a denser configuration. This rearrangement, or volumetric strain, leads to ground settlement. Depending on their magnitude ground settlements can cause significant damage to buried lifelines, pavements, concrete, and building structures. Structures founded on deep foundation elements, such as piles, may experience significant settlement due to the development of negative skin friction, or dragload.

A number of prediction models have been developed for liquefaction-induced strains in saturated sands (Tokimatsu and Seed, 1987; Ishihara and Yoshimine, 1992; Zhang et al., 2002). The method proposed by Zhang et al. (2002) is an integrated CPT-based approach for level-ground sites and the total liquefaction-induced settlement throughout the profile can be computed by:

$$S = \sum_{i=1}^{j} \varepsilon_{vi} \Delta z_i \tag{2.4.1}$$

where ε_{vi} is the post-liquefaction volumetric strain for the soil sublayer *i*, and Δz_i is the thickness of the sublayer *i*, and *j* is the number of soil sublayers. The origins of this approach began when Nagase and Ishihara (1988) performed cyclic simple shear tests, on saturated loose, medium-dense, and dense samples of Fuji River sand. In their work they simulated both unidirectional and multidirectional loading conditions of earthquakes by employing irregular time histories of motions observed during major earthquakes in Japan between 1964 and 1983. They measured the volumetric strains in their samples as pore pressures dissipated following the undrained loading conditions. Based on the laboratory work of Nagase and Ishihara (1988), Ishihara and Yoshimine (1992) generated a family of curves, shown in Figure 2.6, which correlated the volumetric strain due to pore pressure dissipation with relative density (D_r), and the factor of safety against

liquefaction (FS_L) for clean sands. Using empirical correlations between D_r and cone tip resistance (q_c) (Jamiokowski et al., 1985; Tatsuoka et al., 1990), Zhang et al. (2002) were able to develop curves similar to those of Ishihara and Yoshimine (1992) for volumetric strain based on the parameter for clean sand normalized CPT resistance $(q_{c1N})_{cs}$. The set of curves is shown in Figure 2.7 and the accompanying equations for varying factors of safety are provided in Table A.1 of Appendix A. Layer by layer these equations are executed if the FS_L, as determined by the CPT approach (Robertson and Wride, 1998), is less than 1 in order to compute the overall settlement of the profile. The flowchart for evaluation of $CRR_{7.5}$ using Robertson and Wride's (1998) CPT-based method is also provided in Figure A.1 of Appendix A. The flowchart steps through the same computations outlined in the previous section, and assists the engineer in computing volumetric strains for only those soils deemed liquefiable.

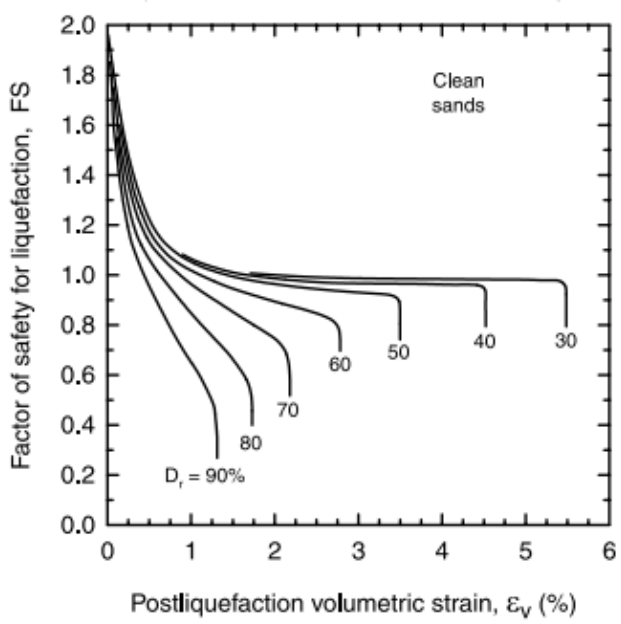

Figure 2.6: Curves for estimating the postliquefaction volumetric strain of clean sands (modified after Ishihara and Yoshimine, 1992).

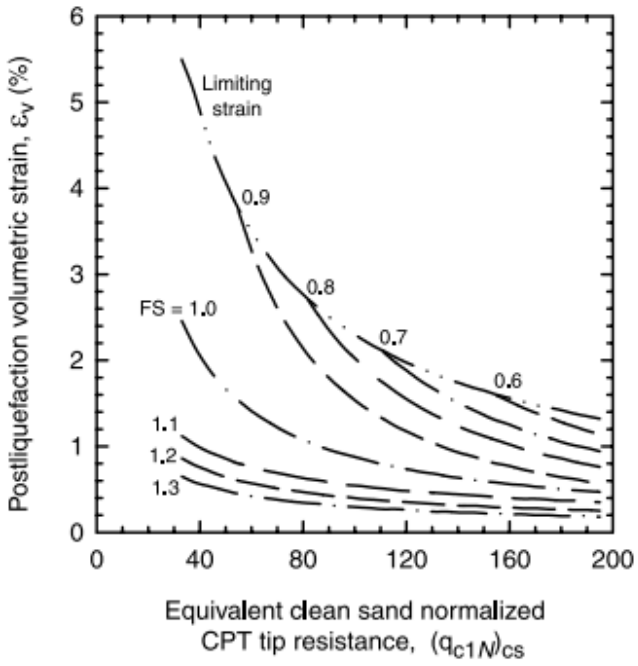

Figure 2.7: Relationship between postliquefaction volumetric strain and equivalent clean sand normalized CPT tip resistance for different factors of safety (FS_L) (after Zhang et al, 2002).

The Zhang et al. (2002) approach was used in this thesis as the basis for estimating the liquefaction induced volumetric strain and settlement in the untreated and treated soil profiles. As shown in Table A.1, the volumetric strain equations are only provided for FS_L of 0.5-2.0 at increments of 0.1. By interpolating between the equations for the discrete FS_L provided we were able to find good agreement with the observed settlement in the untreated soil profile, which will be discussed in greater detail in a later section.

2.5 Summary

Since the liquefaction awakening in the 1960's much has been learned about this phenomenon from both a theoretical and empirical standpoint. Engineers have tools to help make predictions about liquefaction-induced settlements and soil strengths. There is, however, still much

to be learned. Many of the existing relationships were made possible by the availability of case histories from which soil parameters were estimated using back-calculation methods. As more case histories are performed, their data can contribute to a more accurate predictive models, and a better understanding of the true behavior during liquefaction.

3 RAP AND LIQUEFACTION MITIGATION

The potential for enormous damage and loss of life in seismic events motivates continuous study for ground improvement. Soil improvement techniques are commonly used at sites where the existing soil conditions are expected to lead to unsatisfactory performance. Most generally, unsatisfactory performance involves large soil movements (Kramer, 1996). Under aseismic conditions most soil improvement techniques aim to increase the strength and stiffness of soil deposits. However, in a liquefaction event the strain potential of the soil is also directly tied to the excess porewater pressure generation. Consequently, mitigation techniques against seismically-induced settlement seek to reduce excess porewater pressure generation, while simultaneously increasing the strength and stiffness of the soil (Kramer, 1996).

Liquefaction-induced damage can be expensive, yet they are often difficult to predict. On the other hand, ground improvement is also expensive and can typically add between three and ten percent to the total project budget. For this reason, advances in soil improvement technologies are ongoing, and are generally led by specialty contractors aiming to reduce construction costs, or offer a better product. Kramer (1996) explains that research and explanatory "theories" often follow implementation of widely used techniques. While the methods of ground improvement technologies changes rapidly, liquefaction effects are typically reduced by one of four improvement mechanistic categories: drainage, grout and soil mixing, reinforcement, and densification.

3.1 Existing mitigation techniques

3.1.1 Drainage

The provision of drainage avenues for excess pore pressures reduces liquefaction potential, since liquefaction is triggered by the buildup of porewater pressures and a subsequent loss of effective stress in the soil. As such, much liquefaction potential can be removed if the groundwater table can be lowered below the area of interest prior to cyclic loading, or if pore pressures can be allowed to drain during the load cycle. Dewatering the ground can act as a temporary protection against liquefaction, however, this option is not a sustainable long-term solution as it requires constant expensive pumping. Furthermore, if the site is subject to recharge it could lead to a perched water table above the pump depth and negate the effectiveness of the pump altogether. An alternative solution is to provide drainage for excess pore pressures can rapidly dissipate, thereby preventing liquefaction from occurring. Drainage techniques utilizing vertical gravel columns to mitigate liquefaction effects were initially pioneered by Seed and Booker (1977). Stone columns and RAP piers are excellent examples of this type of gravel drains. Conservatively, designers typically rely more on the soil improvements implicit with densification rather than drainage associated with gravel piers. This may be because investigators have found that sand infiltration can reduce the hydraulic conductivity and flow capacity of gravel drains (Boulanger et al., 1997).

3.1.2 Grout and soil mixing

The engineering properties of the soil can be improved by injecting or mixing cementitious materials into the treatment area. *Grouting* techniques fill the void space and fractured zones of the soil while keeping the general soil particle structure intact. *Mixing* techniques disturb the soil structure and physically mix cementitious materials with the soil.

The term grouting is used to describe a variety of processes by which cementitious material is introduced into the ground. Low or high viscosity grout is introduced into the ground with, or without, high pressures. Depending on the chosen technique the soil structure can remain intact, or fractured in a controlled manner to improve densification. In addition, the grout strengthens the bonds between soil particles, creating a type of soil skeleton (Kramer, 1996).

Soil mixing techniques differ from grouting techniques because the soil is mechanically mixed, by large auger-mounted paddles, with the cementitious material being introduced into the profile. The cement can be introduced into the ground in the wet form (as a slurry), or in dry form (as a powder), which uses the water in the ground to complete the cement hydration process (Menard, 2020). Case histories involving the use of soil mixing for mitigation of seismic hazards have been presented by Ryan and Jasperse (1989), Babasaki et al., (1991), and Taki and Yang (1991).

3.1.3 Reinforcement

Often the most effective way to reduce liquefaction susceptibility is to replace the soil with a non-susceptible soil. Excavation and replacement of the susceptible soil is the surest way to remove the liquefaction hazard. Since this is often not possible, many reinforcement techniques have been developed to improve the strength and stiffness of in-situ soil deposits. Reinforcement generally consists of introducing rigid inclusions into the soil, such as steel, concrete, timber, or gravel.

Rigid inclusions are any structural element introduced to reinforce the soil profile by way of drilling or augering. With respect to liquefaction, drilled inclusions are most often used in slope stabilization to increase shear strength. Large drilled shafts placed close together form secant pile

walls that have often been used to stabilize slopes and dams. Other forms of drilled inclusions include tiebacks, soil nails, and micropiles (Kramer, 1996). Liquefaction-induced downdrag has also been proven to apply to drilled shafts (Ishimwe, 2018; Muhunthan et al., 2017).

3.1.4 Densification

Densification is the most commonly used technique for liquefaction mitigation. As discussed previously, looser soils have a greater void ratio and hence, a greater tendency to generate positive excess porewater pressure due to cyclic loading than do denser soils. These tendencies lead to a higher potential for volumetric change post-liquefaction in looser soils. Densification techniques reduce the void ratio of soil before the liquefaction event. A wide variety of techniques can be used depending upon the specific conditions of each project. Approaches to achieve densification range from basic vibratory methods to deep dynamic compaction (DDC) and controlled blasting. Only vibratory techniques will be discussed further as they are similar in nature to RAP.

3.1.4.1 Vibratory compaction and vibratory replacement

Most *vibro* techniques use probes that are vibrated through the soil in order to densify the soil deposit throughout its entire thickness. Castro (1969) explains that when strong vibratory disturbances act upon a sand mass it tends to produce a reduction of its volume irrespective of the density or the degree of saturation of the sand. Field experience on soil compaction has also indicated that vibration is the most efficient procedure to compact cohesionless materials. Vibro techniques can be effective by vibrating horizontally (vibroflotation) as well as vertically (vibro rod systems).

Vibroflotation has been used since 1930 and uses a horizontally vibrating probe, called a *vibroflot*, to densify cohesionless soils by simultaneous vibration and saturation (Brown, 1977). The vibroflot probe described by D'Appolonia (1954) is a long (approximately 12 ft.), slender (15 in. outside diameter) tube with an upper and lower compartment. The upper compartment houses a water-cooled electric motor that drives a 200-lb eccentric shaft held within the lower compartment. The 1-1/4 in. eccentric shaft spins at 1800 rpm., generating a centrifugal force of 10 tons which is responsible for the horizontal vibratory energy required for the compaction of loose sand. The vibroflot is initially lowered to the bottom of the soil deposit by vibration and water or air jetting through openings in the point of the cone that creates a "quick" condition, reducing the impedance of the cone into the soil under its self-weight of approximately 2 tons. When the probe reaches the desired depth for compaction, the water supply is transferred from the bottom of the cone to the top jets, which both aids in compaction and retrieval of the probe as it is withdrawn at a rate of about 1ft/min. As the soil is compacted a conical depression is created at the ground surface. Fill material can be added either from the ground surface or from a bottom fed probe in order to compensate for the settlements due to compaction (Kramer, 1996).

The vibroflot process is repeated in a grid formation across the construction site. Vibroflotation can be effective up to radial distances of 5 ft. from the probe, and has been successfully used to densify soils to depths of up to 115 ft. (Kramer, 1996; D'Appolonia, 1954). Vibroflotation becomes ineffective, however, as fines content increases. Silt and clay soils hold water and do not dissipate pore pressures when subjected to compaction. Hence, vibroflotation has been shown to be effective in soils with fines content less than 20% and clay contents below (3%) (Kramer, 1996).

The vibro rod system is similar to vibroflotation, but uses a vibratory pile driving hammer to produce vibrations in the vertical direction as it pushes a long probe to the desired depth of improvement. A variety of probes have been developed to maximize densification (see *Terraprobe*, *Vibro-Wing*, *Franki Y-Probe*, among others) and by adjusting the frequency of vibration, the probes can be tuned to the resonant frequency of the soil-probe system to increase vibration amplitudes and densify the soil more effectively (Kramer, 1996). As with vibroflotation, fill material is added to reduce densification-related surface settlements. Unlike vibroflotation, the rods use vertical vibratory energy, which is less influential radially than vibroflotation. The grid spacing of vibro rod improvement is often tighter than vibroflotation. Finally, the effectiveness of vibro rods has been shown to vary with depth (Janes, 1973).

3.1.4.2 Vibro replacement

Vibro replacement is the construction of aggregate piers within a soft soil profile. The piers are constructed using either the dry method or the wet method. In the dry method a vibratory shaft is probed into the ground at depth and aggregate is fed through the shaft as it is raised incrementally to the ground surface. Under certain conditions dry construction may require pre-drilling to achieve the required depth if the ground is too dense for the vibrator to penetrate. The wet method of construction introduces the fill aggregate at the surface and uses the same vibratory shaft, along with jetted water, to lower the aggregate through the net zero stress area around the shaft and create the pier. This process is repeated incrementally until the ground surface is reached.

Vibro replacement helps achieve higher soil density by introducing high modulus material into the profile. In cases where drilling is required the softer native soil is removed altogether, leaving more volume for the denser fill material. Vibro replacement piers do more than increase densification alone, some techniques also reinforce the soil properties. This is an added benefit in

soils with medium fines content since vibratory compaction methods are less effective when fines are present. Mitchell (1981) reports that vibrocompaction methods are generally ineffective when the percentage by weight of fines exceeds 20 to 25. Figure 3.1 shows the particle size distribution where vibrocompaction is effective.

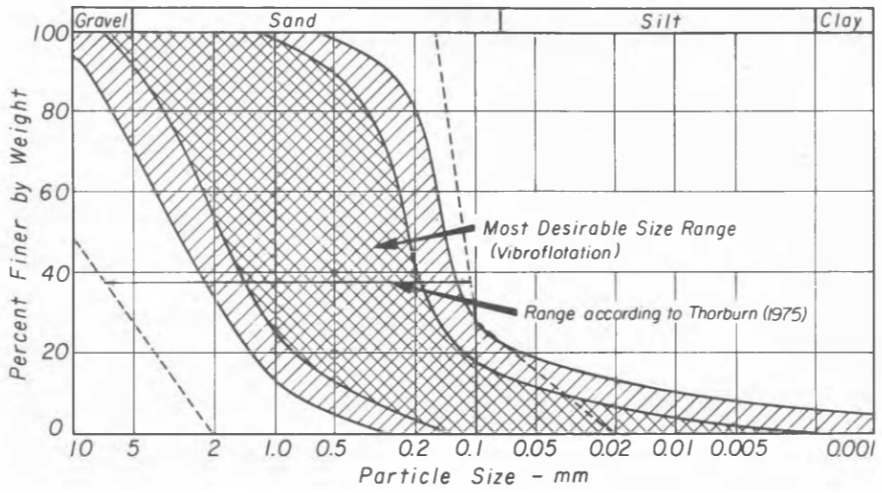

Figure 3.1: Range of particle size distributions suitable for densification by vibrocompaction (after Mitchell, 1981).

In general, soils with higher fines content are difficult to improve using vibratory methods because their low permeability makes it difficult to expel water quickly. Additionally, fines tend to strengthen the soil structure, making it more difficult to vibrate them into a denser state. Several studies have demonstrated the ineffectiveness of vibratory improvement in soils with $I_c > 2.6$ (Mitchell, 1982; Rollins et al., 2006; Rollins et al., 2012). At I_c values above 2.3 CPT tip resistance and SPT blow counts can, in fact, decrease after vibratory improvement is installed. Rollins et al. (2012) performed an interesting comparison of pre- and post-improvement CPT soundings for a bridge abutment constructed on stone columns near Roy, Utah. Their findings are presented in Figure 3.2 which shows the percentage change from the pre- and post-improvement CPT in both

the unaveraged, and averaged forms. This figure shows that vibratory improvement reduces CPT tip resistance above $I_c = 2.3$.

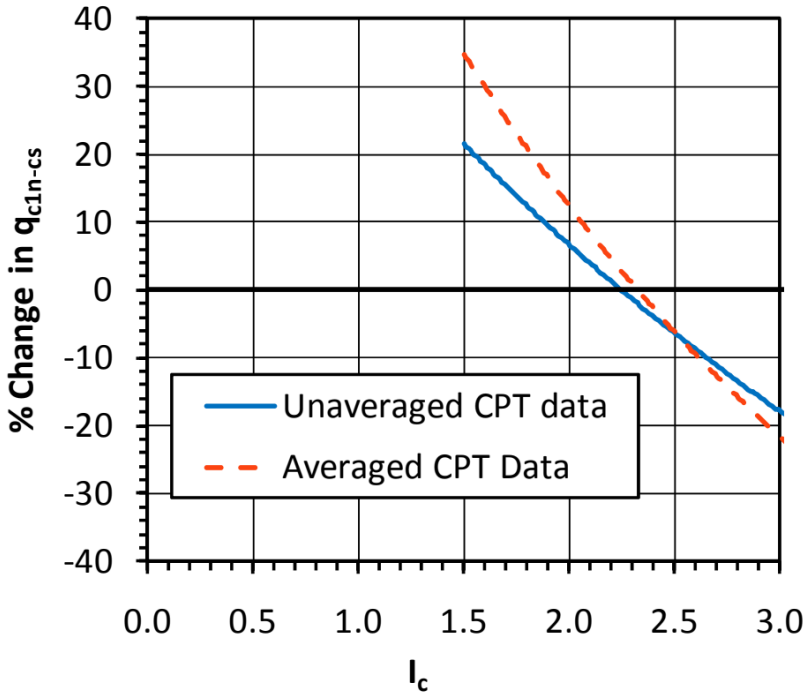

Figure 3.2: Plot showing the percentage change in q_{c1n-cs} after stone column treatment for averaged and unaveraged values (after Rollins et al., 2012).

3.1.4.3 Stone columns

Stone columns (SC) are a most common vibro replacement technique that consist of dense columns of gravel that can be used in both fine- and coarse-grained soils to improve soil density and shear strength. As discussed previously, SC can also increase liquefaction resistance by allowing for radial drainage of excess pore pressures. SC can be installed by the vibroflotation process described in an earlier section, or by another method called the *Franki method*. This process involves driving a steel casing, with an openable bottom, to the desired depth. Once the desired depth is reached the bottom of the steel casing is opened and gravel is inserted through the

steel casing. The gravel is pounded past the casing depth to form a bulb of gravel, after which the casing is raised in incremental lifts and the process is repeated to form a column (Kramer, 1996).

SC improve liquefiable soil deposits by at least four different mechanisms. First, the gravel adds stiffness, density, and strength to the existing profile. Second, they provide grid-spaced drainage paths for excess porewater pressures. Third, the installation process densifies the surrounding soil by the vibration and pounding required to construct the SC. Fourth, the process increases the lateral stresses in the soil surrounding the SC (Kramer, 1996). Stone columns are quite similar to the RAP improvement procedure that will be further explored in this thesis. Proponents of RAP believe RAP to be superior to SC because they have a higher friction angle, greater increase of lateral stress, and have historically outperformed SC.

3.2 RAP reinforcement

A final type of ground-improvement technique will be discussed, and which is the focus of this thesis. Rammed Aggregate Piers® (RAP) are a proprietary ground improvement technique which were originally developed by Geopier Foundation Company® in 1989. Like SC, RAP columns are more effective than vibratory densification techniques in soils with higher fines content because they increase soil density, provide drainage for excess porewater pressures, and increase shear stiffness and shear resistance of the soil (Priebe, 1998

In recent years RAP have been increasingly used as a cost-effective solution to increase the overall strength and stiffness of incompetent soil profiles. RAP are used to support footings ranging in column load from less than 200 kN (50 kips) to as large as 13,300 kN (3,000 kips). They are used to reinforce soils for landslide control, embankment support and retaining wall support (Wissmann et al., 2001). In this section I will describe the construction methodology of

RAP columns (as performed in accordance with Geopier® standards), explore current and past research that has explored the mechanisms of their improvement, and discuss any existing design models for predicting settlement in RAP treated soil.

3.2.1 Construction methodology

RAP columns are similar in nature to SC in that they install high density gravel aggregate in a grid pattern to improve the soil matrix. RAPs are constructed using either replacement or displacement techniques depending on the soil type which they are improving. This means they can be used to reinforce soils ranging from very soft clay and silt, to loose, or dense sand. Replacement techniques are similar to what were described in the SC construction section. Displacement techniques differ from replacement techniques in that they displace the non-replaced existing soil, densifying it in the process.

Displacement techniques are typically performed with an excavator mounted mobile ram base machine fitted with a high frequency (30 to 40 Hz) vibratory hammer as illustrated in Figure 3.3. The base machine drives a 250 to 300 mm outside diameter open-ended pipe mandrel fitted with a unique specially designed 350 to 400 mm diameter beveled tamper foot into the ground. A sacrificial cap or internal compaction mechanism prevents soil from entering the tamper foot and mandrel during driving. The tamper head includes restrictor elements that form a closed valve during downward driving and compaction.

Figure 3.3: A typical RAP vibratory power unit with hopper being loaded with granular backfill (http://www.releo.it/blast-test-impact-pier.php).

After driving to the designed depth, the hollow mandrel serves as a conduit for aggregate placement. Placed inside, the aggregate flows to the bottom of the mandrel. The tamper foot and mandrel are then raised approximately 0.9 m and then driven back down 0.6 m, forming a 0.3 m-thick compacted lift as shown in Figure 3.4. Compaction is achieved through static down force and dynamic vertical ramming from the hammer. The process densifies aggregate vertically and the beveled tamper foot forces aggregate laterally into cavity sidewalls. Crushed gravel (typically graded at 20 to 40 mm in particle size) is fed through the mandrel from a top mounted hopper and compacted in the displaced cavities to create approximately a 0.5 m diameter, dense, stiff, aggregate pier element (Amoroso et al., 2019). The construction methodology has been described in detail by Majchrzak et al. (2009) and Saftner et al. (2018).

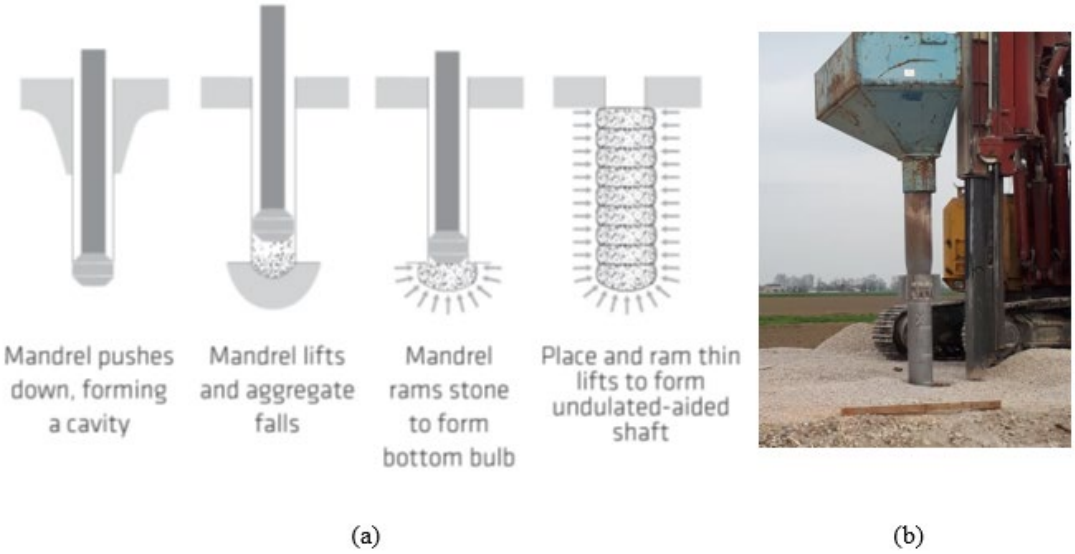

Figure 3.4: (a) Simplified representation of RAP construction process. (b) RAP installation at the Bondeno test site (after Amoroso et al., 2019).

The RAP installation process is designed to densify and increase the lateral earth pressure in the surrounding sand while constructing a dense aggregate column. The applied ramming energy increases the lateral stress and improves the soil surrounding the cavity left by the driven mandrel. Because of the aggregate introduced to the soil matrix from compaction and the significant lateral stress increase, the soil matrix is reported to increase the static allowable bearing pressure of footings on RAP-treated zones by a factor of two to four times the unreinforced allowable bearing pressure (Geopier.com). The benefits of RAP over other types of ground improvement can be large cost savings depending on the project. In one case a project owner of a parking garage in Washington County, Oregon saved $185,000 in foundation costs, which was greater than 50% of the bid price for driven piling (Wissmann et al., 2000).

3.2.2 Current state of RAP research

The principal advantages of RAP relative to SC are still somewhat controversial and are not acknowledged universally in the field of ground improvement. Supporters of RAP argue that there are several principal advantages: First, increased friction angle of the compacted columns, second, the increased lateral pressures generated from the ramming energy input to the aggregate to form the bulbs of each lift, and third, the RAP-soil composite stiffness in response to axial load. In this section, the current state of the practice for RAP ground improvement will be discussed, including well-known benefits of RAP installation, and case histories of their use in liquefaction mitigation.

3.2.2.1 Increased friction angle

One claimed benefit of RAP is their increased friction angle, with respect to friction angles of SC (Geopier.com). Two principal ideas support this claim. First, SC typically use stone that is roughly all the same size, since this facilitates the placement of gravel where no pre-drilling will occur. On the other hand, RAP use graded stone for maximum compaction. Secondly, the construction process for RAP differs from SC and naturally leads to higher friction angles of the aggregate material. The crushing of the aggregate which occurs due to ramming leads to denser configuration of the aggregate and higher internal friction angles. Fox and Cowell (1998) report that average internal friction angles of SC range between 35º-52º, and 48º-52º for RAP. The bounds of RAP friction angles are higher and narrower than for SC.

3.2.2.2 Lateral pressure effect

Stiff elements that have a high internal friction angle cause high lateral stress development in the surrounding matrix soil. As mentioned previously, the ramming action that takes place with the beveled tamper in RAP construction causes an increase in the lateral earth pressure in the soil

surrounding the column (Wissmann et al., 2001). Wissmann and Fox (2000) report that this lateral stress increasingly plays an important role in the deformation characteristics of the RAPs during compressive loading. In a scale model test in clayey soil, Demir et al., (2017) found that the degree to which lateral earth pressures are increased during RAP construction in clayey soil is related to the undrained shear strength of the soil and proximity to the RAP center. Their results from a single RAP test are shown in Figure 3.5 in which they found that lateral earth pressures were increased by up to four times the in-situ pressures. Figure 3.5 shows that the increased pressures tend to dissipate at a distance of approximately 4.5 times the diameter of the RAP from its center. In Figure 3.5 the computed numerical results are plotted with the red line, and the experimental results are shown with the measured blue points. These researchers repeated this test with a triangulated group of three RAPs and found, in this case, that the lateral stress increments were 1.7-4.0 times higher than in the case of a single RAP.

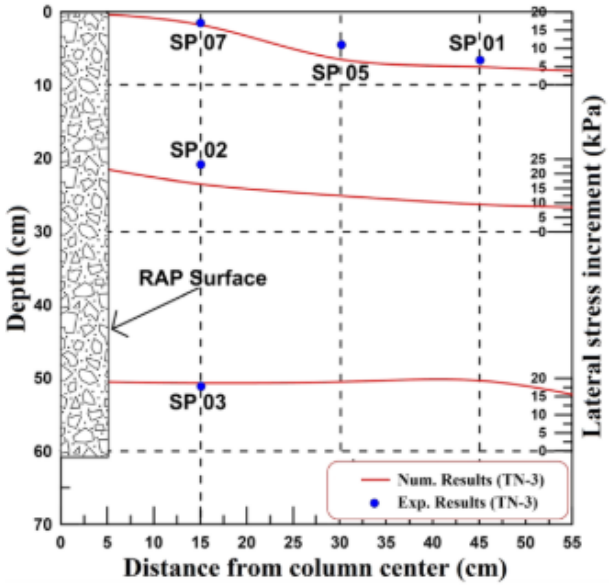

Figure 3.5: Decrease of lateral earth pressure with distance from the RAP center. The red lines represent the measured lateral stresses in the soil matrix (after Demir et al., 2017).

Handy and White (2006) measured the lateral stresses induced near displacement piers during their construction at four different test sites. They found that during ramming, transient liquefaction can occur in saturated soil near the rammer if the lateral stress exerted by ramming exceeds the compressive strength of the soil. The liquefied state allows the ramming strength to be transmitted outward with little or no reduction in pressure. The pressures exerted by the ram create a plastic condition in the soil, which enlarges the longer ramming continues. Excess pore pressures from liquefaction dissipate outward from the plastically deformed area into the elastic zone, which allows the transiently liquefied soil to be compacted during ramming of subsequent lifts.

As discussed in section 2.2, improvements to relative density can reduce liquefaction susceptibility. The introduction of rigid inclusions, or vibrated sand columns into a loose soil will reduce liquefaction potential through improved relative density. A less considered by-product of this type of soil improvement is the increase in lateral earth pressure coefficient, K_0. It is typical when performing a liquefaction analysis, as described in section 2.3, to ignore any explicit improvement due to K_0 because any increase in K_0 is positively correlated with increasing cone tip resistance, q_c, and relative density, D_r, each of which increase liquefaction resistance.

A topic of ongoing research is whether the effects of increased K_0 increase liquefaction resistance independent of its effect on q_c and D_r. As of yet, no conclusive analysis has been performed to demonstrate that liquefaction correlations are independent of K_0. There are, however, varying schools of thought on this topic. Some work has demonstrated that increased lateral earth pressures reduce liquefaction potential independent of other factors (Harada et al., 2010). Others argue that effects of K_0 are completely accounted for by the increased cone tip resistance that results from RAP installation (Salgado et al., 1997). Their work suggests that it may be important

to consider K_0 effects when performing liquefaction potential analysis for any sand deposit that has been improved using compactive methods.

Ishihara and Takatsu (1979) found from a series of cyclic torsional shear tests that the in-situ cyclic resistance ratio (CRR) increases with increasing K_0 in normally consolidated sands by the following relationship

$$\frac{R}{R_0} = \frac{1 + 2K_0}{1 + 2K_{0,NC}} \tag{3.5.1}$$

where R represents the CRR with the improved K_0, R_0 is the original CRR, K_0 is the improved lateral earth pressure coefficient, and $K_{0,NC}$ is the normally consolidated lateral earth pressure coefficient.

Building upon the work of Ishihara and Takatsu (1979), Salgado et al. (1997) aimed to better understand the isolated effects of K_0. Traditionally, q_c is normalized to q_{c1}, as an intermediate step for a number of CPT-based correlations, by considering only the vertical effective stress. To isolate the effects of K_0 Salgado et al. (1997) normalized q_c by the in-situ mean effective stress to obtain an equivalent 1D, normally consolidated form, called $K_{0,NC}$. With the equivalent, normalized q_{c1}, a baseline correlation was established between the CRR pre-improvement and the normalized $K_{0,NC}$ as shown in Figure 3.6. By establishing this baseline correlation these researchers were then able to evaluate the effects of K_0 alone on the prevention of liquefaction triggering. Figure 3.6 shows that two distinct segment exist along the curves: a flatter, and a steeper portion. Over the flatter portion, where $q_{c1} \leq 12$ MPa, the curves shift upwards slightly with increasing values of K_0, and that for a given value of q_{c1} the CRR obtained for K_0=0.68 and K_0=0.90 are at most 7 and 14% greater than for $K_{0,NC}$. Over the steeper portion the curves shift to the right with increasing values of K_0, by as much as 12 and 18%, for K_0=0.68 and K_0=0.90, respectively. These

findings indicate that over the flatter portion of the curve neglecting the effects of K_0 would be slightly conservative, where over the steeper portion neglecting the effects of K_0 would be unconservative (Salgado et al, 1997).

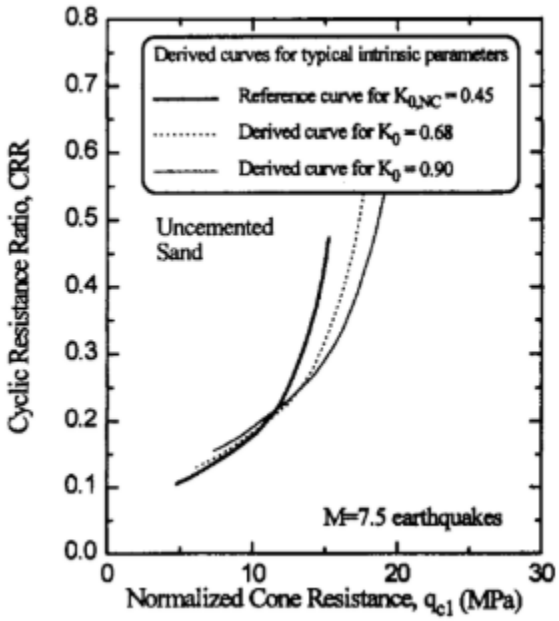

Figure 3.6: Derived CRR-q_{c1} curve for $K_0 = 1.5K_{0,NC}$ and $K_0 = 2K_{0,NC}$ (after Salgado et al, 1997).

The results from Figure 3.6 show the effects of K_0 alone. Salgado et al. (1997) also describe that overconsolidation (OCR) effects enhance the K_0 effects in Figure 3.6. Ignoring the additional benefits of OCR on cyclic strength yields conservatism that increases with increasing OCR. For deep ground improvement techniques that induce high prestressing (OCR), such as RAP, the upward shift of the CRR-q_{c1} curves could be a significant benefit that is currently unaccounted for in design practice. The ability to account for these effects is dependent on further developing techniques that reliably determine lateral stresses and stress history in-situ.

Harada et al. (2010) continued studying the mitigating effects of K_0 against liquefaction. Their work centered on observing K_0 effects from sand compaction piles, which share similar

characteristics with RAP columns. They identified that an increase in liquefaction resistance came from increasing penetration resistance, as well as increased K_0 values. Isolating the effects of K_0, they generated a plot showing the relationship between q_{c1}, K_0 and CRR, similar to that of Salgado et al. (1997). Figure 3.7 shows their findings compared against similar findings by Roberson et al. (1998) and the Architectural Institute of Japan (AIJ) (2001). Figure 3.7 shows that as K_0 increases, so does cyclic resistance, although the curves tend to converged at high q_c values. This suggests that the effect of K_0 tends to decrease in denser soil deposits. Harada et al. (2010) further explained that in loose soil deposits, or those with low q_c values, the incremental increase of CRR from K_0 is greater than the gradient coming from penetration resistance. On the contrary, in denser soil deposits the effect of penetration resistance is more significant than K_0. They summarize their findings by stating that with increasing K_0 the liquefaction resistance increases, but its effect becomes smaller at higher density.

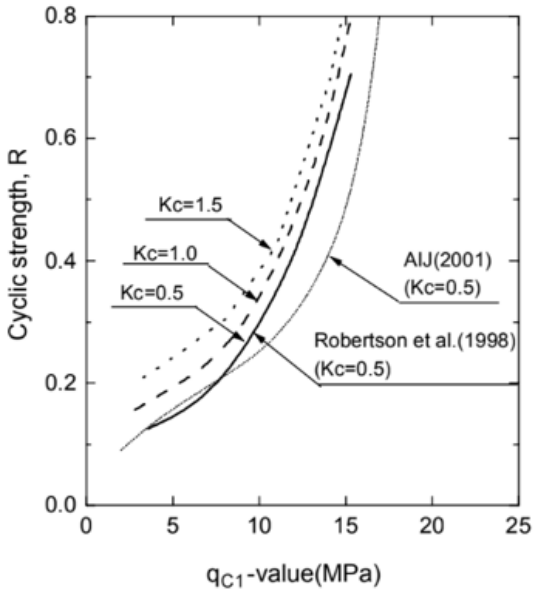

Figure 3.7: Recommended chart correlating corrected q_c value and liquefaction strength with varying K_0 (after Harada et al., 2010).

Increasing lateral earth pressures has therefore been demonstrated to increase liquefaction resistance. Salgado et al. (1997) found that for low SPT-N values, doubling K_0 from 0.45 to 0.90 increased liquefaction resistance by 14%, with the rate of improvement lessening with increasing SPT-N. Harada et al. (2010) found that K_0 was less influential in increasing CPT tip resistance than the research by Salgado et al. (1997). Harada et al. (2010) determined that K_0 had a larger effect on liquefaction resistance than previously believed. They found that in loose soils K_0 was responsible for 46% of the total increased liquefaction resistance by improving K_0 from 0.5 to 1.0. The benefits of K_0 appear to be limited to loose soils, as density increases it can actually become unconservative to include K_0 effects. These benefits are substantial, yet they are often neglected in current practice because the improvements from penetration resistance are more significant (accounting for 50-80% of increased liquefaction resistance). Further exploration of K_0 effects could lead to significant changes in the design approach of ground improvement techniques.

3.2.2.3 RAP-soil composite response

Researchers have attempted to quantify the effects of RAP reinforcement when treated soils are subjected loading. Research has been done to investigate composite action under both axial and shear loading. To this point, evidence shows real positive effects from axial composite action, though many studies have shown that a lack of data exists to support any theory of shear strain compatibility.

Green et al. (2008) studied the shear stiffening effects of RAPs in liquefiable soils using a finite element approach. These researchers suggest that one way in which the RAPs mitigate liquefaction risk is by redistributing the seismically induced shear stresses from the soil to the RAP columns. Smith and Wissmann (2018) report, however, that the level of shear stress reduction in the surrounding soil due to in-situ installation of RAPs has not been demonstrated by field data.

Smith and Wissmann suggest that it may be possible that the increase in composite shear stiffness may be explained by a well-coupled pier-soil response that transfers shear stresses effectively across the soil-pier interface (2018). Field tests have shown that some load sharing does occur at the RAP-soil interface.

The hypothesis of shear stiffening has been explored using theoretical studies done using equivalent beam analysis (Goughnor and Pestana, 1998), 2D plane-strain finite element (FE) analysis (Green et al., 2008), and 3D FE analysis (Olgun and Martin, 2008). These tests have all shown that flexure of discrete columns significantly reduces the effectiveness of columns to reduce shear stresses in the soil matrix. Centrifuge testing peformed by Rayamahji et al. (2015) also demonstrates that columns are ineffective at reducing induced shear stresses during cyclic shaking. This is important because shear strain is directly related to pore pressure generation which causes liquefaction.

On the other hand, axial composite action works by principle, since the materials settle together, the load received by the soil or RAP, respectively, would be in proportion to the material's stiffness. Demir et al. (2017) measured the load sharing between soil and a single RAP in their scale model study. Using pressure plates centered on the RAP and on the surrounding soil bed they measured the contact stress on the RAP and the contact stress on the surrounding soil bed as load was applied uniformly by a loading plate. The ratio between the recorded stress in the RAP and the surrounding soil they labeled the stress ratio. Their results are provided in Figure 3.8 and it can be seen that initially the stress concentration ratio spikes to 8.5, yet as the composite material continues to settle the stress ratio levels off at about 6.

Demir et al. (2017) performed the same load tests on a triangulated group of three RAPs. They found that the stress concentration ratio in a group to be between 2 and 4 as shown in Figure

3.9, or approximately one-half to one-third the stress concentration ratio in the single RAP case. In Figure 3.9 the red, green, and black plotted lines represent the measured stress concentration ratios in each one of the three test RAPs, respectively.

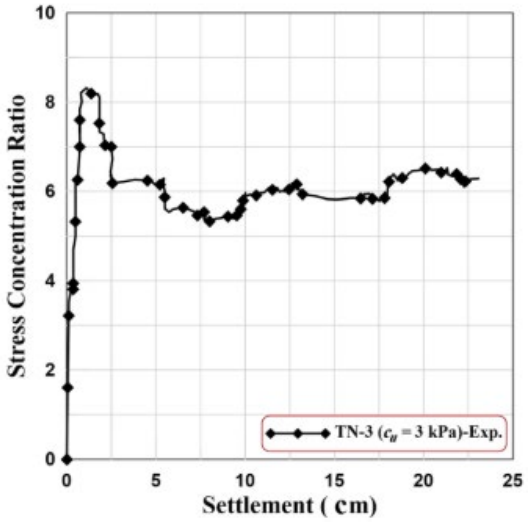

Figure 3.8: Stress concentration variation with respect to settlement. The stress concentration ratio is the measured stress on the RAP cell divided by the measured stress in the cell on the surrounding soil (after Demir et al, 2017).

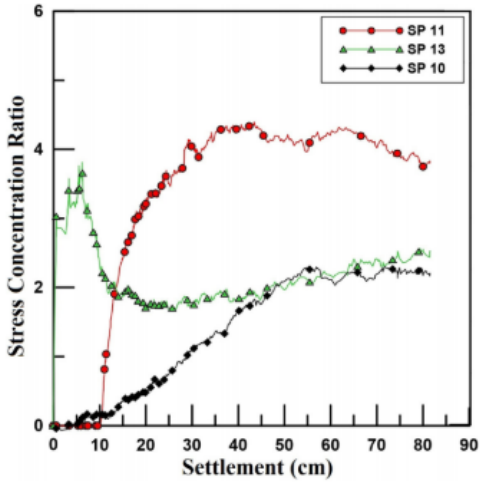

Figure 3.9: Variation of stress concentration with respect to settlement for group RAP tests (after Demir et al., 2017).

Wissmann et al. (2001) provided evidence for the theory of vertical axial composite action during their full-scale modulus load tests of 31 piers throughout the Piedmont region of the United States. During their modulus load tests a telltale metal plate was placed at the bottom of each pier prior to construction. Two vertical metal bars, encased within PVC pipes to reduce friction between the bars and the aggregate, were attached to the metal plate to provide measurements of deflection at the bottom of the pier during load tests. A load was then applied at the top of the pier through a pressure plate and deflections were measured at both the top and the bottom of the pier.

The response behavior, or the deflection in response to loading in both the bottom and the top plate, to the modulus load tests is shown in Figure 3.10 (A) and (B), respectively. Figure 3.10 (A) shows the bulging type behavior observed in a number of the tests. As the pressure applied at the top of the pier increases, the difference between the deflection of the top plate and the bottom plate grows larger. Since the metal plates at the top and bottom of the pier are constitutively equivalent, it can be inferred from the difference in their deflections that the load applied at the top of the pier dissipates before reaching the bottom of the pier. The researchers attribute this behavior to a bulging behavior of the pier as it expands into the surrounding matrix soil. The applied load is then transferred between the RAP and the matrix soil, such that a small percentage of the load reaches the base of the pier.

In contrast, Figure 3.10 (B) illustrates a different behavior, one in which a much larger percentage of the load reaches the base of the pier. The load transferred to the base of the pier acts first to compress the bottom bulb and then is distributed by end bearing to the soil underneath the bulb. The linear deflection prior to the inflection point in either plot represents the settlement of the pier before the bulging behavior begins. The steeper portion of the deflection curve after the inflection point indicates the bulging of aggregate pier. The vertical difference between the top

plate and the bottom plate is indicative of the load transferring that occurs between the RAP and the matrix soil.

In either case (A) or (B) the performance of the soil profile is improved. The bulging behavior in case (A), while it leads to increased settlement, is still considered to be an advantage of aggregate piers over stiffer inclusions because the bulging behavior acts as a cushion that distributes the load among a pier group instead of concentrating it on the most resistant pier within the group (Wissman et. al, 2001). In case (B) a larger percentage of the load applied at the top of the RAP is transferred to a load bearing stratum at depth.

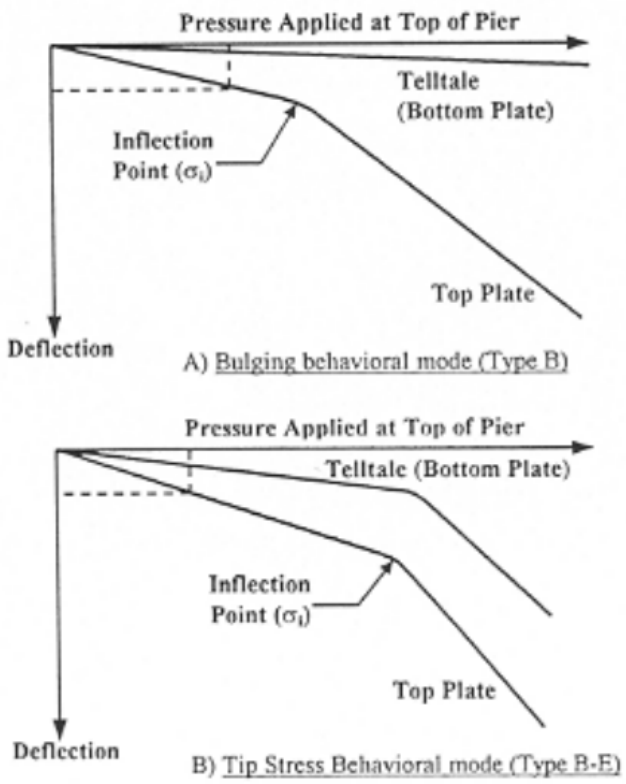

Figure 3.10: A) Bulging behavior. The matrix soil carries much of the load, thus the telltale plate at the bottom of the pier experiences little deflection, B) Tip stress behavior. A significant portion of the load applied to the RAP reaches the bottom bulb (after Wissmann et al, 2001).

3.2.2.4 RAP for liquefaction mitigation

RAP elements have been used on projects around the world for liquefaction mitigation. Their effectiveness in mitigating liquefaction in clean sandy soils has been well documented. Extensive research was performed in Christchurch, New Zealand, following the Canterbury Earthquake Sequence in 2010-2011 (Wissmann et al., 2015; Vautherin et al., 2017; Amoroso et al., 2018). Takeaways from these research studies show that RAPs are effective at mitigating liquefaction potential through densification in soils with a soil behavior index, I_c, < 1.8. Several experimental and constructed case histories, however, provide evidence that RAP provide more liquefaction protection than from densification alone.

In Ecuador, for instance, an interesting case study was performed after the Muisne earthquake (M_W 7.8) of 2016. Major damages occurred during this earthquake to the embankments of the Mejia bridge, which experienced measured peak ground accelerations of 0.32g. The embankments of this bridge were placed on unsupported soil consisting of loose to medium dense silty and clayey sands. Meanwhile, the embankments of the nearby Boca de Briceño bridge experienced higher peak ground accelerations of 0.38, yet suffered only minor and easily repairable damages. The Boca de Briceño bridge is supported on soil similar to the Mejia bridge, but is RAP treated. Evidence of liquefaction was present at both the Mejia bridge, and the Boca de Briceño bridge outside of the footprint of the RAP treated area. Liquefaction susceptibility analyses for the Boca de Briceño bridge embankment showed that the site should have been susceptible both before and after RAP installation, yet there was no evidence of liquefaction in the RAP treated zone (Smith and Wissmann, 2018). This case history suggests that the combined benefits of increased confinement and increased densification were not the only mechanisms of improvement provided by the RAP in this event.

Another case study was performed during the Christchurch testing program in New Zealand. Wissmann et al. (2015) report that large-strain T-Rex testing showed that the composite reinforced ground exhibited shear stiffness values greater than the unimproved soil by a factor of 3 to 5. The results of this test suggest that RAP improve liquefaction resistance by an increase in shear stiffness response of the reinforced ground.

3.2.3 Existing RAP settlement design models

In practice, a number of methods have been used to estimate settlements of soil profiles treated with rigid inclusions. Several settlement models in use for RAP are also used for SC profiles. Existing settlement methods have been covered well by Özgür (2008) and the interested reader may see his work for a comprehensive discussion of these methods.

In practice, finite-element models are most widely used for predicting RAP settlements. However, one simple procedure which will be discussed in this literature review is the subgrade modulus approach suggested by Lawton and Fox (1994). They suggest that when design engineers plan for settlements in RAP treated soil, the settlements should be considered in two distinct zones. The first is the upper zone, or the zone of matrix soil reinforced by the aggregate piers. The second, or lower zone, is the zone beneath the RAP group that is subjected to compression due to footing stresses at the tip of the piers. Within the upper zone, settlements have been computed in the past based on a spring analogy. By this method the footing is assumed to be perfectly rigid relative to the foundation materials. Hence, the stress applied to the composite foundation materials (RAP pier and soil) depend on their relative stiffness (R_s), as mentioned in section 3.2.2.3, and area coverage. The total downward force (Q) on the footing is resisted by a total upward force in the RAP (Q_g) and soil (Q_s) as shown in the following equation:

$$Q = qA = Q_g + Q_s = q_g A_g + q_s A_s \tag{3.2.3.1}$$

where q_g is the stress at the top of RAP elements beneath the footing, and A_g is the area of the pier elements below the footing, q_s and A_s are the stress in the soil matrix below the footing, and the area of soil below the footing, respectively.

Since the footing is essentially rigid compared to the bearing materials, the settlement of the pier will equal the settlement of the matrix soil. The settlement of the foundation (s) can be written in terms of RAP stress and RAP stiffness modulus (k_g) or in terms of the matrix soil stress and matrix soil stiffness modulus (k_s):

$$s = \frac{q_g}{k_g} = \frac{q_s}{k_s} \tag{3.2.3.2}$$

Equation 3.5.3.2 can be rewritten to express the matrix soil stress in terms of the aggregate pier stress and the ratio of the pier and matrix soil modulus values (R_s):

$$q_s = q_g \left(\frac{k_s}{k_g}\right) = \frac{q_g}{\frac{k_g}{k_s}} = q_g / R_s \tag{3.2.3.3}$$

Combining Equations 3.5.3.1 and 3.5.3.3 and defining area ratio (R_a) as the ratio of A_g to A:

$$q = \frac{q_g A_g}{A} + \frac{q_g A_s}{A R_s} = q_g R_a + \frac{q_g (1 - R_a)}{R_s} = q_g \left[R_a + \frac{1}{R_s} - \frac{R_a}{R_s}\right] \tag{3.2.3.4}$$

$$= \frac{q_g [R_a R_s + 1 - R_a]}{R_s}$$

Rewriting q_g in terms of q:

$$q_g = \frac{q R_s}{R_a R_s + 1 - R_a} \tag{3.2.3.5}$$

Settlements in the upper zone are then computed using Equations 3.2.3.2 and 3.2.3.5, which depend on the applied composite footing stress, the relative stiffness of the aggregate pier and soil

materials, the area ratio of the aggregate pier elements, and the aggregate pier stiffness modulus (Lawton and Fox, 1994; Lawton et al., 1994).

Settlements in the lower zone can be estimated using conventional geotechnical settlement analysis procedures (Terzaghi and Peck, 1967; Das, 2014).

3.2.4 Knowledge gaps relative to RAP treatment for liquefaction hazard mitigation

To this point, the present state of RAP research has been examined. The results of practical performance, as well as full-scale tests have demonstrated that RAPs improve axial stiffness in sandy and silty soils. The quantitative data of these case histories indicate that the level of improved performance cannot be accounted for by densification alone. Researchers have shown that the additional improvement can be accounted for by increased densification. It has been hypothesized that further improvement must be considered as a result of increased lateral stresses, however, these claims remain to be fully validated.

The literature demonstrates that further study of RAP improvement is necessary to better understand their effectiveness in soils with higher fines content, namely, is it possible to improve soils with $I_c > 2.3$. As shown in other studies, the ability to improve these soil types would be advantageous over other vibratory methods. In addition, there is a lack of consensus over whether the effects of increased K0 reduce ground settlements from liquefaction. These effects require further examination. Finally, this thesis will aim to develop a predictive settlement model that can be used reliably for design purposes in silty sand soils.

The liquefiable target layers at the test site in Bondeno contain higher fines content than other aforementioned tests conducted on RAP columns. This experiment will further investigate

the influence of soil densification, increased lateral earth pressures and increased profile stiffness from composite action on liquefaction resistance.

4 PRELIMINARY INVESTIGATIONS AND SITE CHARACTERIZATION

4.1 Geotechnical conditions

To locate a site for the field tests, INGV, a research team from the University of Bologna (UNIBO), and local geologist Luca Minarelli performed geologic investigations within 15 km of a site in Mirabello (Italy) where a similar blast test was performed in 2016 to measure liquefaction-induced downdrag on micropiles (Amoroso et al., 2017). The selection of the test site was chosen with respect to the 2012 Emilia Romagna seismic sequence that resulted in observable liquefaction across the region. The moment magnitudes of the earthquakes were 6.1 occurring on May 20, 2012 and 5.9 on the 29th of the same month (ISIDe working group 2016). The selected test site is located 15 km to the northeast, and 24 km to the northeast of the epicenters of these respective earthquakes (Pondrelli et al., 2012). The eventual test site was selected from among several locations where physical evidences of liquefaction were found (Emergeo Working Group, 2013). In addition, a soil profile with moderate fines content with low plasticity was desired to evaluate RAP effectiveness in these soils.

After considering an acceptable limit of vibrations for human perception and building damage (PPC & PPV), a site located on agricultural land was chosen near Bondeno situated in Emilia-Romagna region of Italy (anals). The site particularly satisfied the requirements for

liquefaction potential since sand boils and sand-filled cracks were observed shortly after the 2012 earthquake (Anals and Obs). Sand boils and sand cracks are a result of increased pore pressure below ground. When a saturated sand layer liquefies, the excess pore pressure causes the water to push through cracks often taking sand sediment with it as it moves to the surface. Due to the well documented observance in the area, the test site was deemed a reliable location to perform the full-scale experiment.

According to geologic journals the location of the test site outside of Bondeno, Italy, was formed by naturally accumulated Holocene and late Pleistocene Age sediments deposited by the Po river (Regione Emilia-Romagna 1998). The in-situ investigations found that the silty sand layers from 3.5 to 12.6 m consists of Holocene alluvial deposits in a paleo channel of the Po river, while the deeper sand and silty sand layers are late Pleistocene glacial braided Po river deposits. Several generations of fluvial channel deposits, fed from the south by the Appenine streams, and from the west by the Po river appear at the outcrop of the younger soil unit (Amoroso et al., 2019).

Following site selection, the subsoil profile of the test site was characterized by INGV and UNIBO by a thorough review of geologic records, as well as by geo-testing methods. Cone penetration tests, standard penetration tests, geophysical tests, disturbed sampling, downhole characterizations, trenches and dilatometer testing were utilized along with historical data to create an accurate profile at the site (Amoroso et al., 2019). Invasive and non-invasive tests were performed by UNIBO and GEO before and after ground-improvement, and before and after blasting to observe the respective variations in the physical properties of the soil from each activity. The pre-improvement in-situ site investigations are shown in Figure 4.1, and comprehensively consisted of two boreholes, one 15 m deep borehole in the improved panel, and one 7.1 m borehole

in the natural panel. Six SPTs were performed within the borehole in the improved panel. No SPTs were performed within the borehole in the natural panel.

Two undisturbed samples were obtained by from the natural panel with a Shelby tube sampler for static and cyclic laboratory tests by UNIBO. Six disturbed samples from the natural panel, and 14 disturbed samples from the improved panel were also obtained for grain size distribution analyses, Atterberg limits, petrographic analyses and radiocarbon dating. Piezocone (CPTU) and seismic dilatometer (SDMT) tests were also performed in both the natural panel and the improved panel 15-20 m deep.

Geophysical tests were performed by INGV prior to improvement consisted of: five electrical resistivity tomography (ERT) lines crossing both IP and NP, 63 m long, spaced at 2 to 5 m (P1A-P1B, P2A-P2B, P3A-P3B, P4A-P4B, P5A-P5B); one active P-wave and S-wave tomography, 71 m long with 72 P-wave and S-wave geophones per line; and one passive 2D-rectangular array of 72 P-wave geophones spaced at 3 m, and centered in IP.

As shown in Figure 4.2, the profile consists of a surface layer composed of silty clay and clay (CL) to a depth of 3.5 m, underlain by silty sand (SM) to a depth of 12.6 m, which is in turn underlain by sands and silty sands (SP-SM). The topsoil consists of an agriculturally worked mixture of liquefied sand extrusions and silty-clayey fines down to 0.8 m below the surface. The Ravenna Subsynthem contains clays and silts (0.8-3.4m) overlaying a silty sand (3.4-12.6m), a sandy silt (12.6-13.6m) and sands and silty sands (13.6-15.6m). The highest fines content ($D < 0.075$ mm) of the soil profile came within the silty layer between 2-3.4 m depth and was between 75 and 93%. The range of fines content beneath this layer was typically between 20 and 40% (Amoroso et al., 2019).

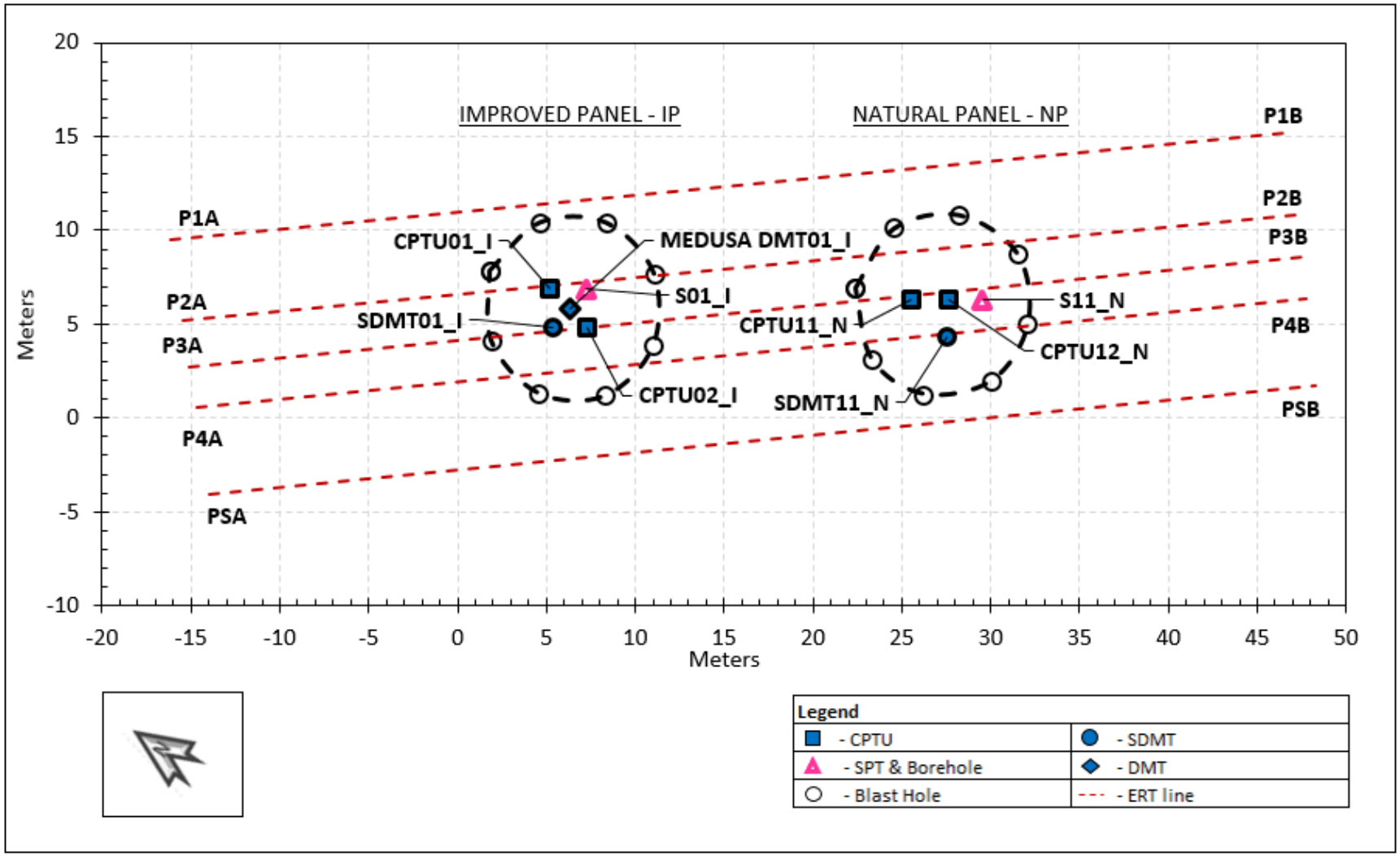

Figure 4.1: Map of the in-situ site investigations performed prior to RAP installation and blast-testing.

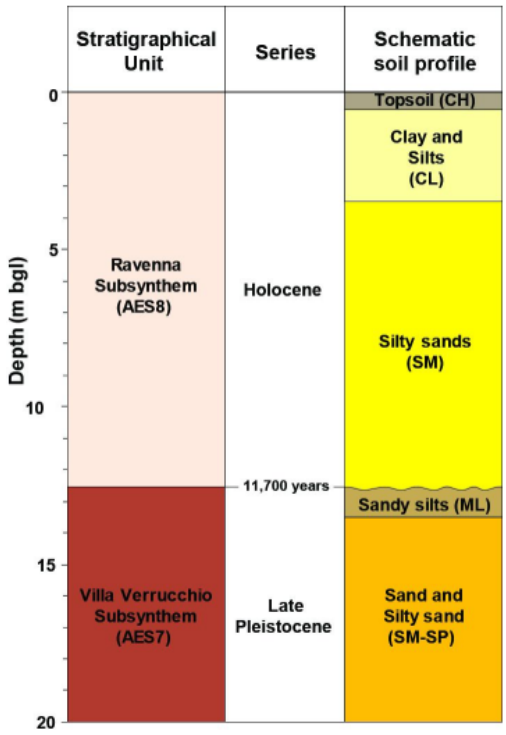

Figure 4.2: Simplified soil profile of the test site in Bondeno, Italy (after Amoroso et. al, 2019).

The results from the CPTu and SDMT in-situ testing at the natural panel (NP) and improved panel (IP) before RAP installation (pre-treatment) were plotted by our BYU research team and are shown in Figure 4.3 and Figure 4.4, respectively. Both surveys indicate that, generally speaking, the profile consists of a surface layer composed of silty clay and clay (CL) to a depth of 3.5 m, underlain by silty sand (SM) to a depth of 12.6 m, which is in turn underlain by sands and silty sands (SP-SM). Past geological investigations found that the silty sand layers from 3.5 to 12.6 m consist of Holocene alluvial deposits in a paleo channel of the Po river, while the deeper sand and silty sand layers are late Pleistocene glacial braided Po river deposits (Regione Emilia-Romagna 1998, Amoroso et al., 2019). The parameters obtained from the CPTu as shown in Figure 4.3 are very similar for the NP and IP sites. Figure 4.4 also shows that the SDMT survey

of the two profiles show good agreement, with some minor variations in constrained modulus, *M*, and horizontal stress index, K_D. The fines contents were estimated using a correlation proposed by Robertson & Wride (1988). However, laboratory measured fines contents in the sand layers are typically between 20 and 40% and are considerably higher than interpreted from the correlation.

Our BYU research team plotted the CPTu data from the IP with depth on the normalized soil behavior type chart (see explanation in section 2.5 of this work) in Figure 4.5 (Robertson, 1990). Figure 4.5 clearly depicts the distinct stratification of the profile into two primary layers. Between 0-3 m depth the profile behaviorally consists of clayey and silty soil with $I_c > 2.6$. Recall that for liquefaction assessment per Robertson and Wride (1998) soils with $I_c \geq 2.6$ are considered non-liquefiable. Beyond 3 m depth the profile consists of sands and sandy mixtures with $I_c < 2.6$. This stark division of soil layers greatly facilitated the liquefaction assessment in this study.

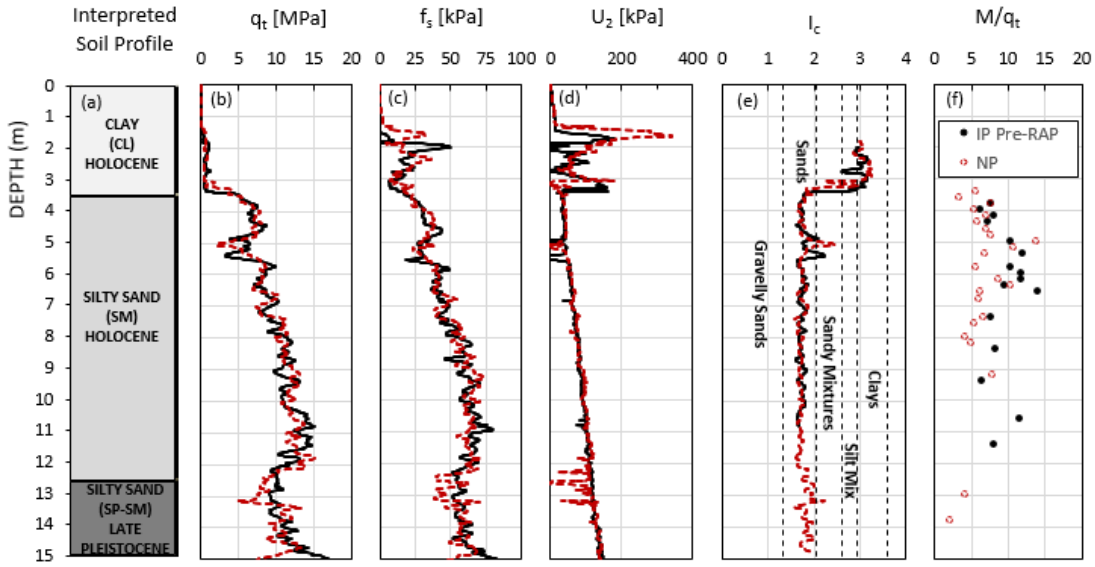

Figure 4.3: (a) Interpreted soil profile and comparisons of CPTu test results at the Natural Panel (NP) and the Improved Panel (IP) prior to RAP treatment with respect to (b) cone resistance, q_t, (c) sleeve friction, f_s, (d) porewater pressure, U_2, (e) soil behavior type, I_c, and (f) ratio of constrained modulus to cone tip resistance M/q_t.

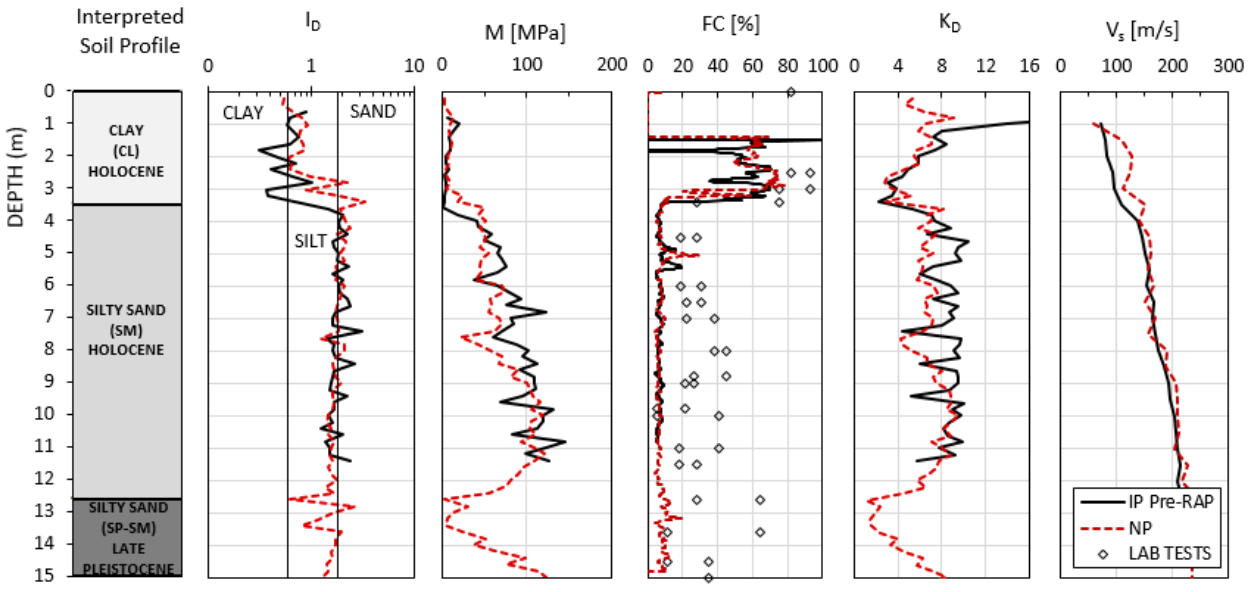

Figure 4.4: (a) Interpreted soil profile and comparisons of SDMT test results at the Natural Panel (NP) and the Improved Panel (IP) prior to RAP treatment with respect to (b) soil material index, I_D, (c) constrained modulus, M, (d) fines content, FC (e) horizontal stress index, K_D, and (f) shear wave velocity, V_s.

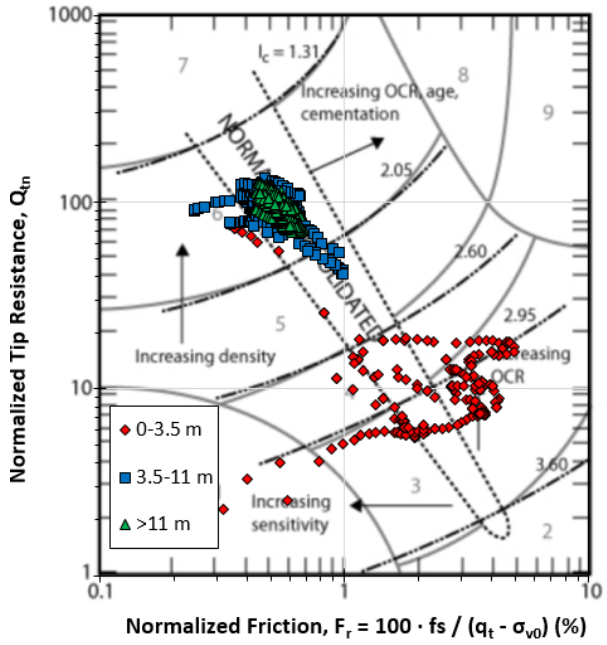

Figure 4.5: Soil behavior type plot consisting of CPTu data from a sounding in the IP prior to treatment.

4.2 Liquefaction assessment

Researchers from the University of Bologna (UNIBO) used piezocone test data to determine liquefaction susceptibility at the test site. By applying the well-established CPTU-based procedure proposed by Idriss and Boulanger (2008), a liquefaction susceptibility analysis was performed for a moment magnitude M_w = 6.14 (Meletti et al., 2008) and peak ground acceleration a_{max} = 0.22g (Stucchi et al., 2011). These values correspond to values used in ongoing seismic microzonation studies of the Bondeno municipality. The ground water table (GWT), which seasonally fluctuates between 0.5 and 1.5 m, was assumed at a worst-case depth of 0.5 m for the design ground motion. Based on this analysis, the researchers identified a potential liquefiable layer from 3 to 8 m in depth (Amoroso et al, 2019). The UNIBO researchers determined that the site yielded a high risk for liquefaction especially for the thick layer of saturated apenninic deposits between 6 and 8 m which confirmed the prior observations from the 2012 seismic event.

In this study, our BYU research team also performed an additional liquefaction potential assessment using the Idriss and Boulanger (2008) CPTu method, with the same earthquake magnitude and acceleration as the researchers from UNIBO. This was done in order to verify the UNIBO results. This assessment was done using CLiq V. 3.0, a commercial liquefaction program developed by GeoLogismiki, in collaboration with Gregg Drilling and Professor Peter Robertson. Our resulting analysis also showed that the layer between 3 to 8 m depth was expected liquefy for the given earthquake and ground acceleration. The CSR and CRR are each plotted with depth in the pre-treated soil in Figure 4.6 (a). Areas where the CSR exceeds the CRR are zones of FS_L<1.0 and potentially liquefiable when subjected to the given earthquake parameters. The FS_L is plotted with depth through the pre-treated soil profile in Figure 4.6 (b). This figure confirms the work of the UNIBO researchers and identifies the target zone of susceptibility between 3 and 8 m depth.

Using the computed FS_L from Figure 4.6 we estimated the predicted settlement using the volumetric strain approach proposed by Ishihara and Yoshimine (1992). This method is the precursor to the integrated CPT approach by Zhang et al. (2002) which predictive settlement will be shown in Chapter 8 of this work. The Ishihara and Yoshimine (1992) method requires both D_r and FS_L as inputs to estimate volumetric strain as shown by Figure 2.6. We used different pairs of D_r and FS_L to obtain a range of anticipated settlement values. Relative density was approximated using both the Jamiolkowski (2003) and the Tatsuoka (1990) approaches. In addition to the FS_L computed in Figure 4.6 constant values of $FS_L = 1.0$ and $FS_L = 0.93$ were also evaluated between the depths of 3-11 m. The results of these settlement approximations are shown in Figure 4.7.

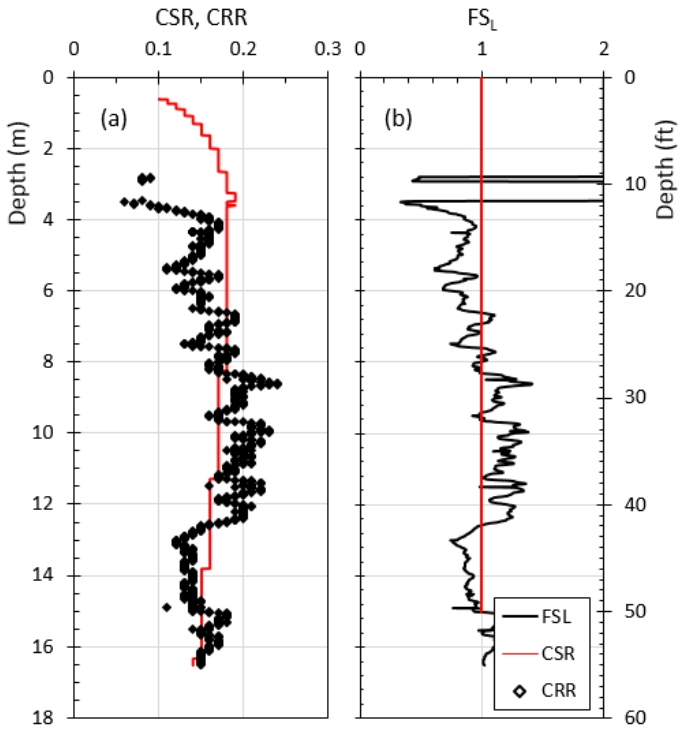

Figure 4.6: (a) Cyclic stress ratio (CSR) and cyclic resistance ratio (CRR), (b) Factor of safety against liquefaction in the natural soil.

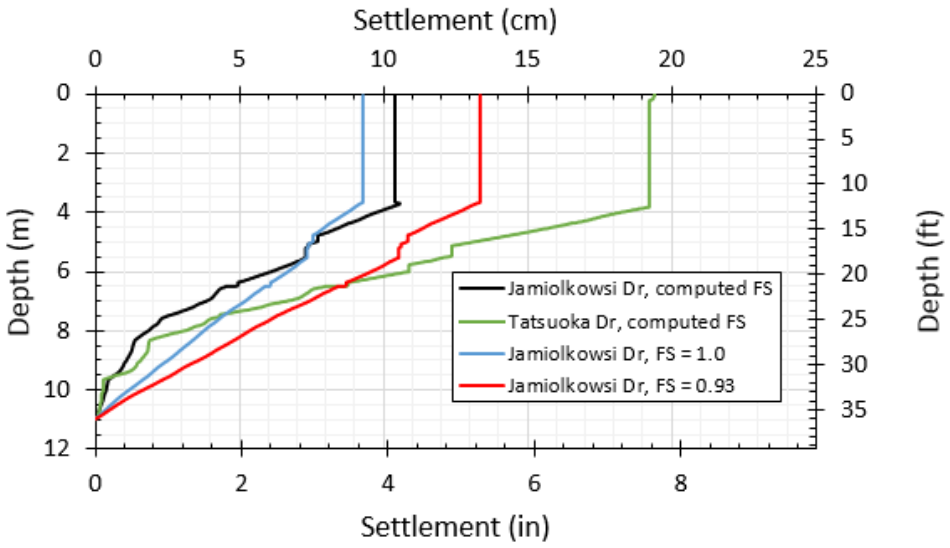

Figure 4.7: Predictive settlement for the design earthquake using the Ishihara and Yoshimine (1992) settlement approach with pairs of D_r (computed by Jamiolkowski [2003] and Tatsuoka [1990]) and FS_L (computed by Idriss and Boulanger [2008] or using fixed FS_L).

5 GROUND IMPROVEMENT PROCEDURE

5.1 Construction of RAP columns

RAP construction at the test site was performed by Releo, a licensed local affiliate of Geopier®, carried out in accordance with the procedure described in section 3.2.1. This section describes the details of the actual construction performed at the test site. Prior to RAP installation, a 0.5-m thick working platform was constructed over the site to facilitate transit of the construction equipment over the clayey surface layer. The working platform consisted of sandy gravel with some construction debris. Figure 5.1 is an aerial photograph taken of the test site during RAP construction and shows the ramming hammer on a track-mounted RAP column installer, with its hopper being loaded with granular backfill. The working platform is the lighter colored soil and was removed before the test date.

Over a three-day period between the end of March and the beginning of April 2018, a 4x4 quadrangular grid (2 m center-to-center spacing) of RAP columns was installed to a depth of approximately 9.5 m. This depth was chosen because the anticipated liquefiable layer was between 3 and 8 m, as described in section 4.2. The pier diameter was 0.5 m with an associated area replacement ratio, defined as the ratio of the pier area to the tributary soil area surrounding the pier, equal to 5%. Ten RAPs were subjected to flow rate tests and crowd stabilization tests for a quality control of the ground improvement work. The results of the crowd stabilization tests of the 16 piers is provided in Table 5.1.

Figure 5.1: (Left) Aerial photograph at the Bondeno test site showing the track mounted ramming hammer with a hopper being loaded with gravel aggregate. (Right) Photo of a typical hopper and mandrel being compacted by the vibratory power unit (http://www.releo.it/blast-test-impact-pier.php).

The pier number in Table 5.1 corresponds to the order in which the pier was installed. The order number of installation of the piers is shown in Figure 5.2. The first three installed piers (1, 2 and 3) were placed on the northeast end of the improved area. The crowd tests results of these piers from Table 5.1 show that settlement during the crowd test was much higher on piers 1, 2 and 3 than for the latter installed piers. The larger crowd test settlements are attributable to the inconsistencies during construction. It appears that the quality of RAP construction improved as the crew practiced and became familiar with the site, since crowd test settlements become more consistent and lessen with time.

Table 5.1: Summary of RAP installation details and crowd test results for each pier.

Pier No.	Installation Date	Driven Depth (m)	Platform Thickness (m)	Total Meters Built	Crowd Test (mm)[c]		
					Bottom[a]	Middle (4,5m)[b]	Top (0,5m)[b]
1	3/30/2018	9.9	0.5	9.4	0	350	35
2	3/30/2018	9.9	0.5	9.4	0	420	160
3	3/30/2018	10.1	0.5	9.6	0	135	10
4	3/30/2018	10.0	0.5	9.5	0	50	10
5	3/30/2018	10.0	0.5	9.5	0	40	0
6	3/30/2018	8.3	0.5	7.8	-	-	-
7	3/31/2018	10.0	0.5	9.5	-	-	-
8	3/31/2018	9.0	0.5	8.5	-	-	-
9	3/31/2018	10.0	0.5	9.5	-	-	-
10	3/31/2018	9.85	0.5	9.35	-	-	-
11	3/31/2018	9.0	0.5	8.5	-	-	-
12	3/31/2018	6.0	0.5	5.5	0	45	0
13	31/03/2018-03/04/2018	10.0	0.5	9.5	10	95	13
14	4/3/2018	10.0	0.5	9.5	0	10	0
15	4/3/2018	10.0	0.5	9.5	0	12.5	0
16	4/3/2018	10.0	0.5	9.5	0	85	0

[a]test performed on top of bottom bulb

[b]depth from natural grade

[c]max crowd force sustained for 20 seconds

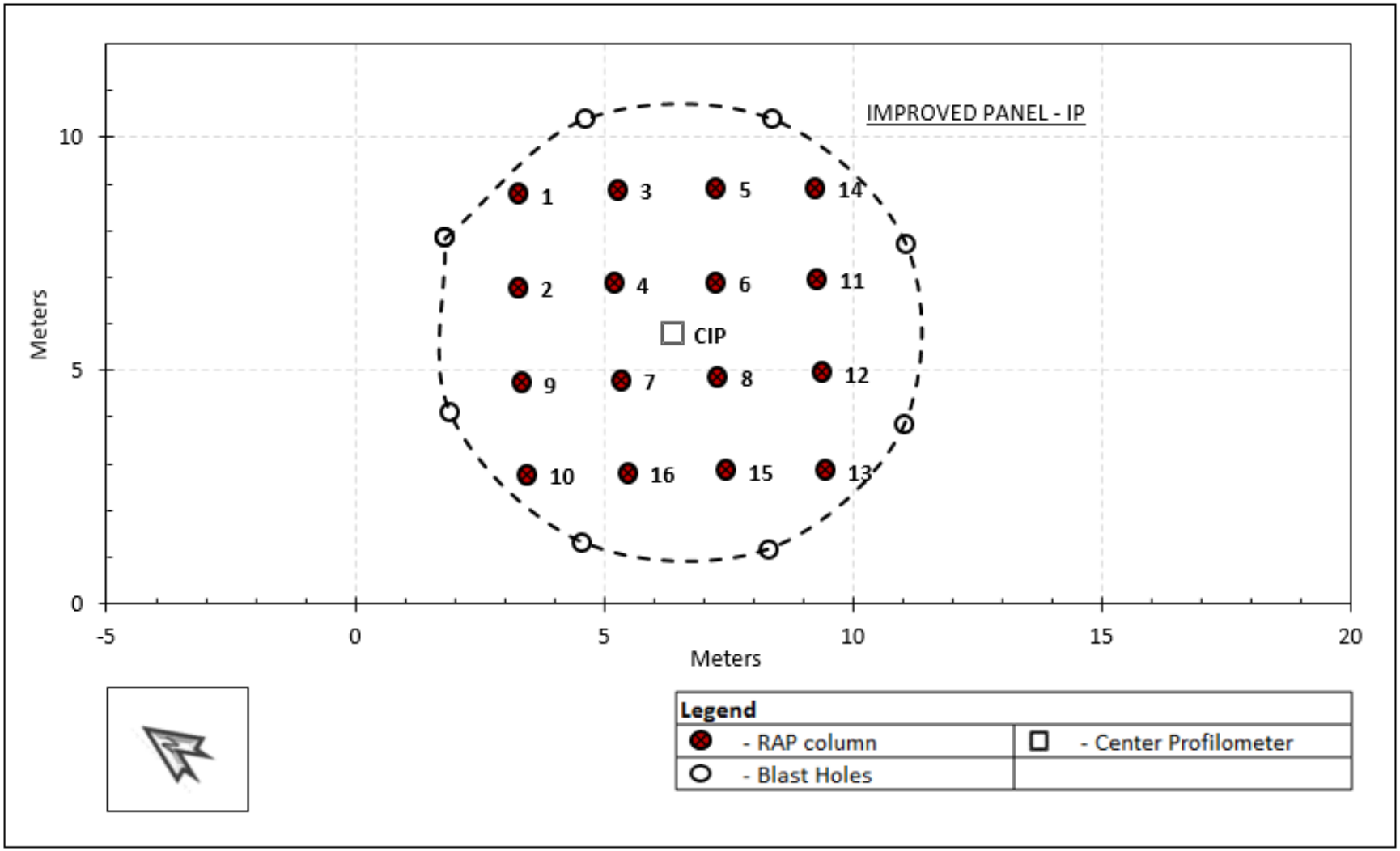

Figure 5.2: Order and placement of RAP installation corresponding to Table 5.1.

5.2 Post-RAP ground improvement evaluation

At the end of April 2018 supplementary geotechnical tests were carried out by UNIBO in the middle of four piers to quantify the improvement. The location of these tests are shown in Figure 5.3 namely CPTU01bis (15 m deep), MEDUSA DMT01bis (from a depth of 5 to 11 m) and SDMT 01bis (15 m deep), to evaluate the RAP effectiveness one month after the construction. At the beginning of May 2018 the working platform was removed to allow the geophysical surveys that were performed prior to ground improvement to be repeated. The pre-improvement plots are from one seismic dilatometer SDMT01_I, performed to 11.4 m depth, and the post-improvement characteristics are plotted from two tests: seismic dilatometer SDMT01bis_I, performed between 0 m and 4.8 m depth, and medusa dilatometer MDMT01bis_I, performed between 4.6 m and 11.2 m depth.

The CPTu and DMT test results were plotted by our BYU research team and are shown in Figure 5.4 and Figure 5.5. These figures summarize the profiles with depth after RAP installation from the post-improvement CPTu and SDMT surveys. Figure 5.4 shows the improvement in terms of the corrected cone tip resistance q_t, cone sleeve friction, f_s, relative density, D_r, soil friction angle, ϕ, and ratio of constrained modulus to cone tip resistance, M/q_t. The constrained modulus, M, is inversely proportional to settlement and generally increases with increasing density and the confinement provided by the RAP grid. Figure 5.5 shows the improvement in terms of the constrained modulus, M, lateral earth pressure coefficient K_D, at rest lateral earth pressure coefficient, K_0, and shear wave velocity V_s.

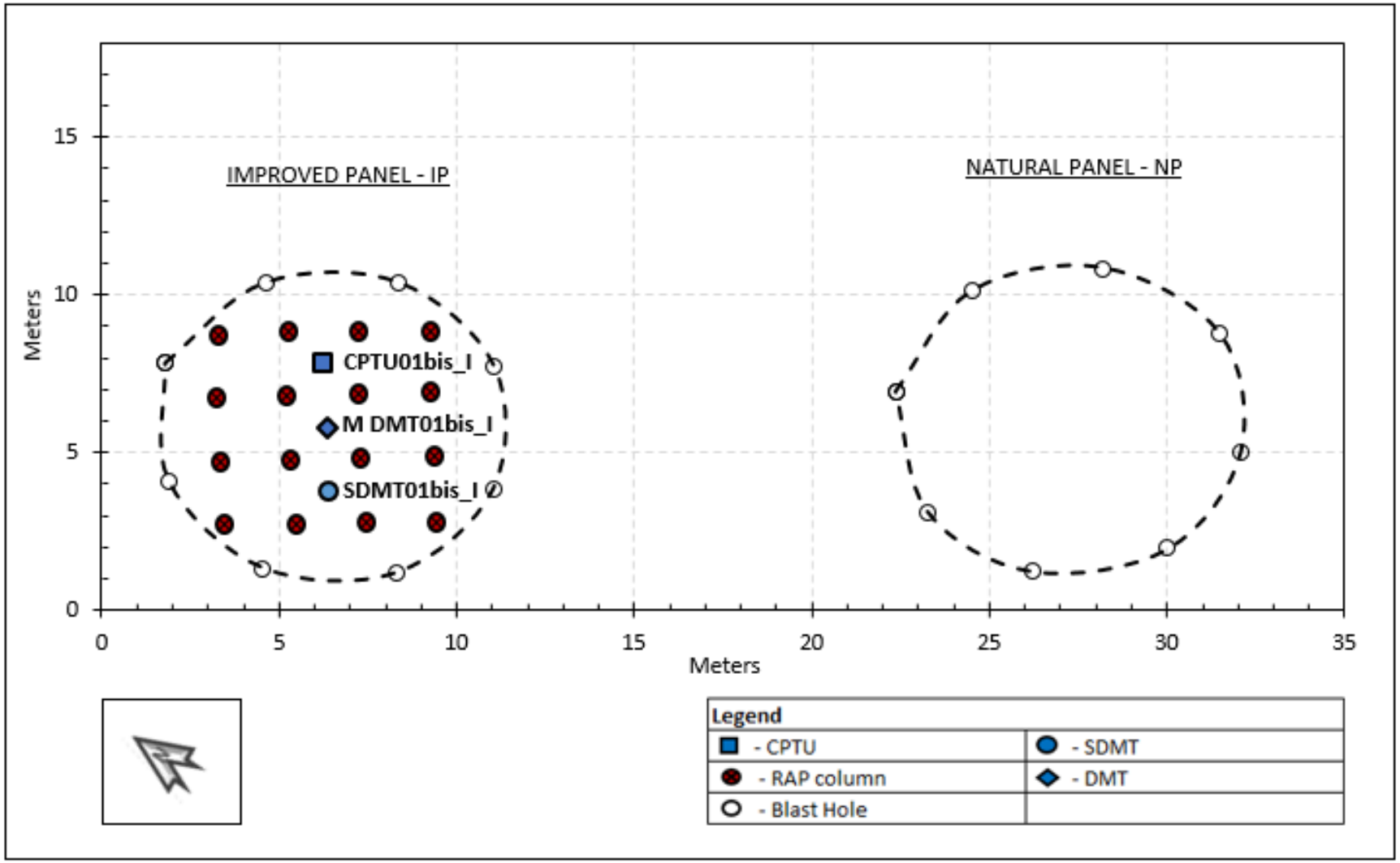

Figure 5.3: Map of the in-situ site investigations performed after RAP installation and prior to blast-testing.

As anticipated, little to no improvement occurred from RAP installment in the clay layer between 0 m and 3 m depth. Between the depths of 4 and 9.5 m the corrected cone tip resistance, sleeve friction, were significantly improved. The relative density, which we computed using a correlation with CPT cone resistance (Jamiolkowski et al., 2003), also shows moderate improvement in this region. The Jamiolkowsi et al. (2003) relative density equation is provided below:

$$D_r = A'_0 + B_0 \ln\left(\frac{q_c}{\sqrt{\sigma'_{mo}}}\right) \tag{5.2.1}$$

Where A'_0 and B_0 are constants dependent on soil type, and σ'_{m0} is the mean effective stress. The layer of soil between 3-8 m depth was called the target zone due to its susceptibility to liquefaction, as the FS_L was less than 1 in this zone. Within the target zone (3-8 m depth) we attained a relative density of 75%, which is comparable to other deep foundation improvement techniques, as discussed in chapter 3. M, K_D, and K_0 also experienced large improvement which is consistent with expectations based on the installation process. The constrained modulus, M, is a telling parameter as it is inversely related to settlement. Between 4-8 m depth the average percent improvement to M was 25%. The dilatometer test results in Figure 5.5 clearly show that soil parameters representing in-situ lateral earth pressures were dramatically increased, within some layers by as much as 100%. Between 3-8 m the average K_D was improved from 7.6 to 10.9, where the average K_0 was improved from 1.1 to 1.4 within the same zone. For both parameters the layer between 4-5 m depth saw the least improvement. It is possible that this is due to the higher percentage of fines in this layer. This layer also plotted within the sandy mixtures on the soil behavior type (SBT) chart, indicating that the soil behavior was more towards silt than sand. The

V_S profiles show a smaller increase after treatment within the same depths of interest. This is to be expected because Vs is less affected by increases in density and lateral earth pressure.

We plotted the post-RAP profile again on Dr. Robertson's soil behavior type chart shown in Figure 5.6. It can be seen that the distinct layers have remained, however, several interesting changes are present. First, there are fewer data points that plot within the sand-mixture category of group 5. It appears that the improvement caused some of these data points to move into group 4, indicating sand. Secondly, the spread of the data pairs in group 4 is wider than the pre-improved state. Many data points plot to the left of the normally consolidated (NC) window, indicating increasing sensitivity. Some of the data pairs plot to the right of the NC window, indicating increasing overconsolidation, or increased lateral earth pressures. From this record it appears that RAP installation may have caused similar behavior to that observed by Rollins et al (2012), where some layers experienced increased lateral earth pressures, while other layers experienced reduced horizontal stresses. Finally, it appears that the surficial clay layer experienced increasing overconsolidation, meaning that RAP were effective at increasing lateral earth pressure in the clay.

As part of this study, our BYU research team also performed the same liquefaction potential assessment on the post-improved soil. Using the same input parameters and the Idriss and Boulanger (2008) approach, as given in section 4.2 (M_w=6.12 and a_{max}=0.22g), the liquefaction potential was computed and is plotted with depth in Figure 5.7 (a). Prior to improvement the FS_L was less than one throughout the 3-8 m depth. After improvement the FS_L was increased above one for all but the layer between 4.5-5.5 m, within which the magnitude of improvement was lessened due I_c values greater than two. Figure 5.7 (b) shows that the ratio of liquefaction potential of the post-RAP to pre-RAP was between one and two, with an average increase of 43% within this zone.

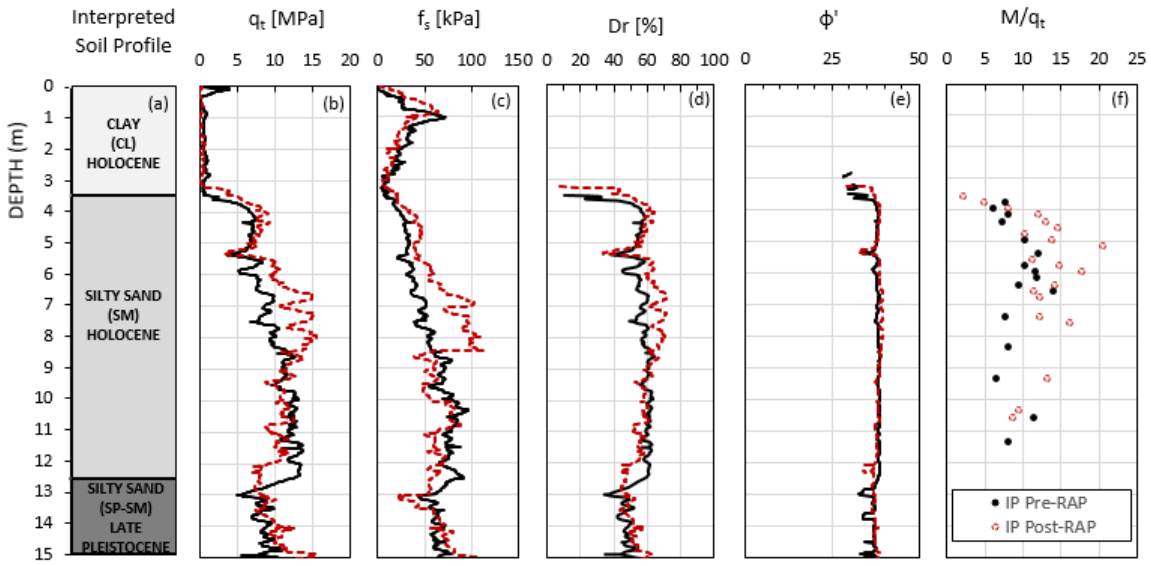

Figure 5.4: (a) Interpreted soil profile and comparisons of effects of RAP improvement as measured by CPTu test results with respect to (b) cone resistance, q_t, (c) sleeve friction, f_s, (d) relative density, Dr, (e) soil friction angle, ϕ, and (f) ratio of constrained modulus to cone tip resistance M/q_t.

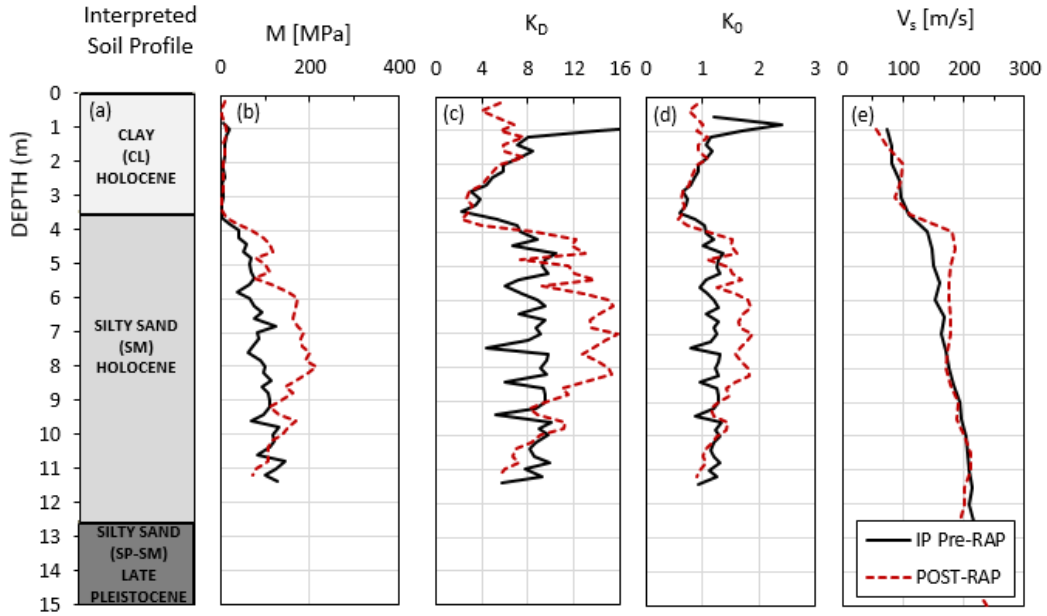

Figure 5.5: (a) Interpreted soil profile and comparisons of effects of RAP improvement as measured by SDMT test results with respect to (b) constrained modulus, M, (c) horizontal stress index, K_D, (d) at rest earth pressure coefficient, K_0, and (e) shear wave velocity, V_s.

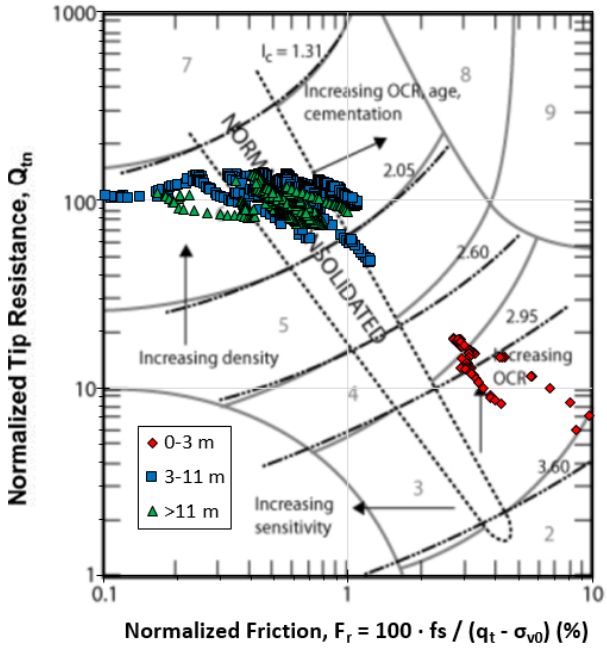

Figure 5.6: Soil behavior type plot consisting of CPTu data from a sounding in the IP after treatment.

We also computed the FS_L for both the pre-RAP and post-RAP profiles using a larger earthquake magnitude and peak ground acceleration. We did this, firstly, because predicting the size of a blast large enough to produce liquefaction is difficult to do; and secondly, to quantify the effects of RAP improvement in the event of a larger seismic event. Our research team also wanted to evaluate whether the relationship between the FS_L pre- and post-improvement would change with increasing earthquake intensity. Thus, we performed the assessment again using a M_W=7.5 and a_{max}=0.3. Figure 5.8 shows that the RAP improved soil would have outperformed the untreated soil between 6 and 8.5 m depth. It is clear from Figure 5.8 (a), however, that given the larger earthquake the treated soil would likely not have prevented liquefaction outside of the 6 to 8.5 m range. Figure 5.8 (b) shows that the relationship of the post-pre improvement ratio did not change drastically with the increasing magnitude of the design ground motions. From this we can infer that if the blast charges do cause a ground motion that significantly differs from the design motion, the ratio of the effects should be the same between the pre- and post-RAP treated soil profiles.

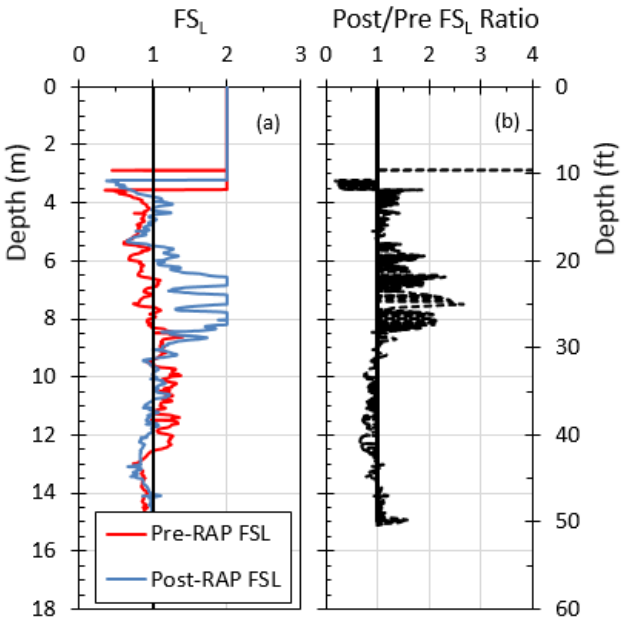

Figure 5.7: (a) Factor of safety against liquefaction pre- and post-RAP improvement, (b) ratio of post-RAP/pre-RAP FS_L, assuming M_W=6.14, a_{max}=0.22 g.

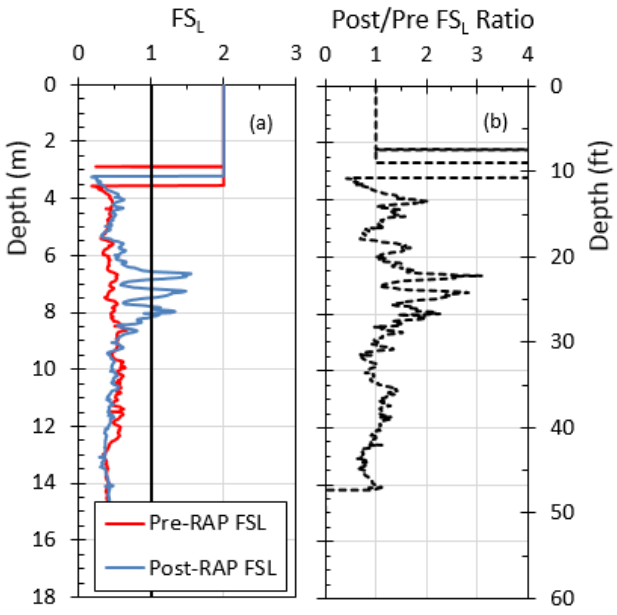

Figure 5.8: (a) Factor of safety against liquefaction pre- and post-RAP improvement, (b) ratio of post-RAP/pre-RAP FS_L, assuming M_W=7.5, a_{max}=0.3 g.

6 BLAST TEST PROCEDURE AND SITE INSTRUMENTATION

6.1 Explosives setup and blast procedure

Liquefaction was induced using a blasting procedure that had previously been shown to successfully produce liquefaction for full-scale foundation testing (Gohl et al., 2001; Finn, 2001; Ashford et al., 2004; Ishimwe, 2018; Amoroso et al., 2018). Previous tests have shown that blast induced liquefaction can be used to evaluate performance of deep foundation and ground improvement systems over large areas and at significant depths (Ashford et al., 2000; Ashour and Norris, 2003; Ashford et al., 2004; Rollins, 2004; Rollins and Strand, 2006; Strand, 2008; Rollins and Hollenbaugh, 2015; Stuedlein et al., 2016; Amoroso et al., 2017; Amoroso et al., 2018). Blast-induced liquefaction can also produce settlements similar to those observed from liquefaction induced by earthquakes (Amoroso et. al, 2019).

One limitation of this approach is that the mechanisms of pore pressure generation are not identical to those in earthquakes. In an earthquake event, the porewater pressure is increased slowly as shear waves propagate vertically through the soil. By contrast, during blasting the porewater pressure is increased by a combination of compression and shear waves generated by the explosion. Blasting produces higher ground accelerations and higher frequency ground motions than an earthquake, yet the velocity and strain levels are comparable (Ashford et al, 2004).

To give relevancy to the test data, we performed tests around the natural panel and the improved panel with identical blast charge weights and detonation sequences. Blast holes were drilled up to 7 m deep by GEO to place charges at two different levels (or decks) within the liquefiable layer: 0.5 kg at 3.5 m and 2.0 kg at 6.5 m as shown in Figure 6.1. Each blast hole was cased with a 75 mm diameter PVC pipe. Each charge was buried inside the PVC pipe with sand backfill (stemming) and topped off with sandbags to direct the blasting forces radially into the surrounding soil at depth, rather than vertically upward through the blast pipe. For each panel eight blast holes were equally distributed around a 5 m-radius ring at 45° intervals, considering that the center-to-center distance of the two panels is approximately 20 m. The blasts of the two panels were conducted separately (i.e. blast 1 for the NP and blast 2 for the IP) to limit effects of superposition and simplify the comparison of the effects of the blast induced liquefaction on the IP and the NP, separately.

The explosive charges were detonated sequentially at one second intervals with detonation of the bottom charge followed by the upper charge in each blast hole. The sequence of blasting was the same for both the NP and the IP, and is indicated by the blast hole number shown in Figure 6.2 with blast hole alternating from opposite sides of the ring. Explosives were installed on the day of the blast (June 4, 2018) for safety reasons.

The perimeter of the circle formed by the blast holes is considered the blast circle as often mentioned in this report. However, liquefaction and associated settlements extended beyond the blast rings. Liquefaction was recorded by the furthest accelerometers at our test site, which were

located midway between the two blast rings at 12 m from the blast center. We anticipated that the blast forces would be the largest nearest the blast holes. We also expected that the cyclic forces would be the greatest at the center of the blast circle with an equidistance to the surrounding blast holes assuming uniformity in the soil stratigraphy. As the distance increases from the blast center and blast zone we expect that the forces from blasting dissipate.

The blasts of the two panels were designed separately by INGV (i.e. blast 1 for the NP and blast 2 for the IP) to limit effects of superposition and simplify the comparison of the effects of the blast induced liquefaction on the IP and the NP, separately. The first blast test occurred on June 4, 2018 at 12:16:43 and the second blast occurred at 15:20:41 the same day (as recorded by Dave Anderson, the Civil Engineering lab manager at Brigham Young University).

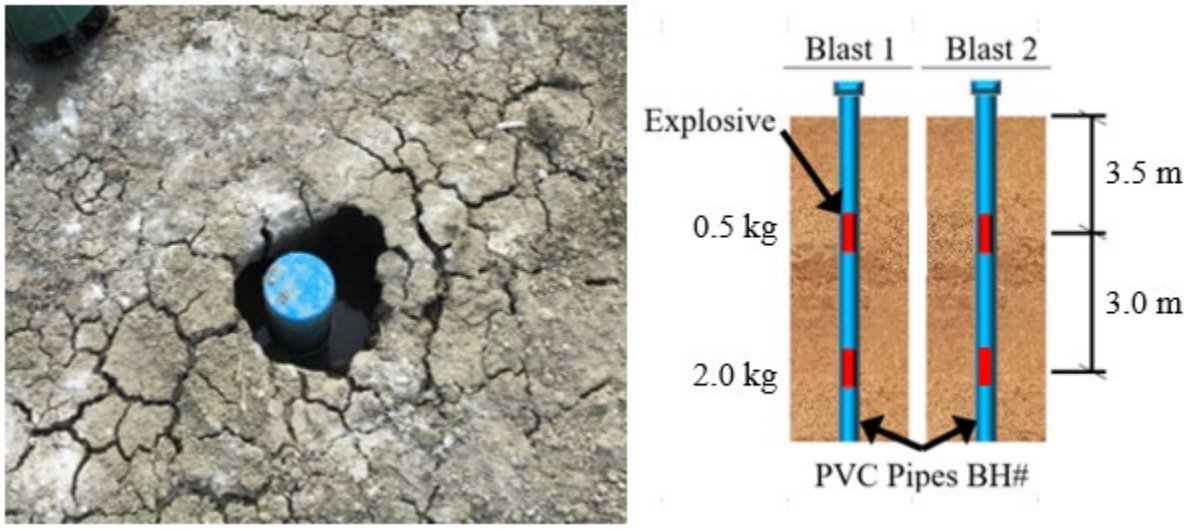

Figure 6.1: Blue PVC pipe with cap where charges were lowered to the appropriate depths (modified after Lusvardi, 2019).

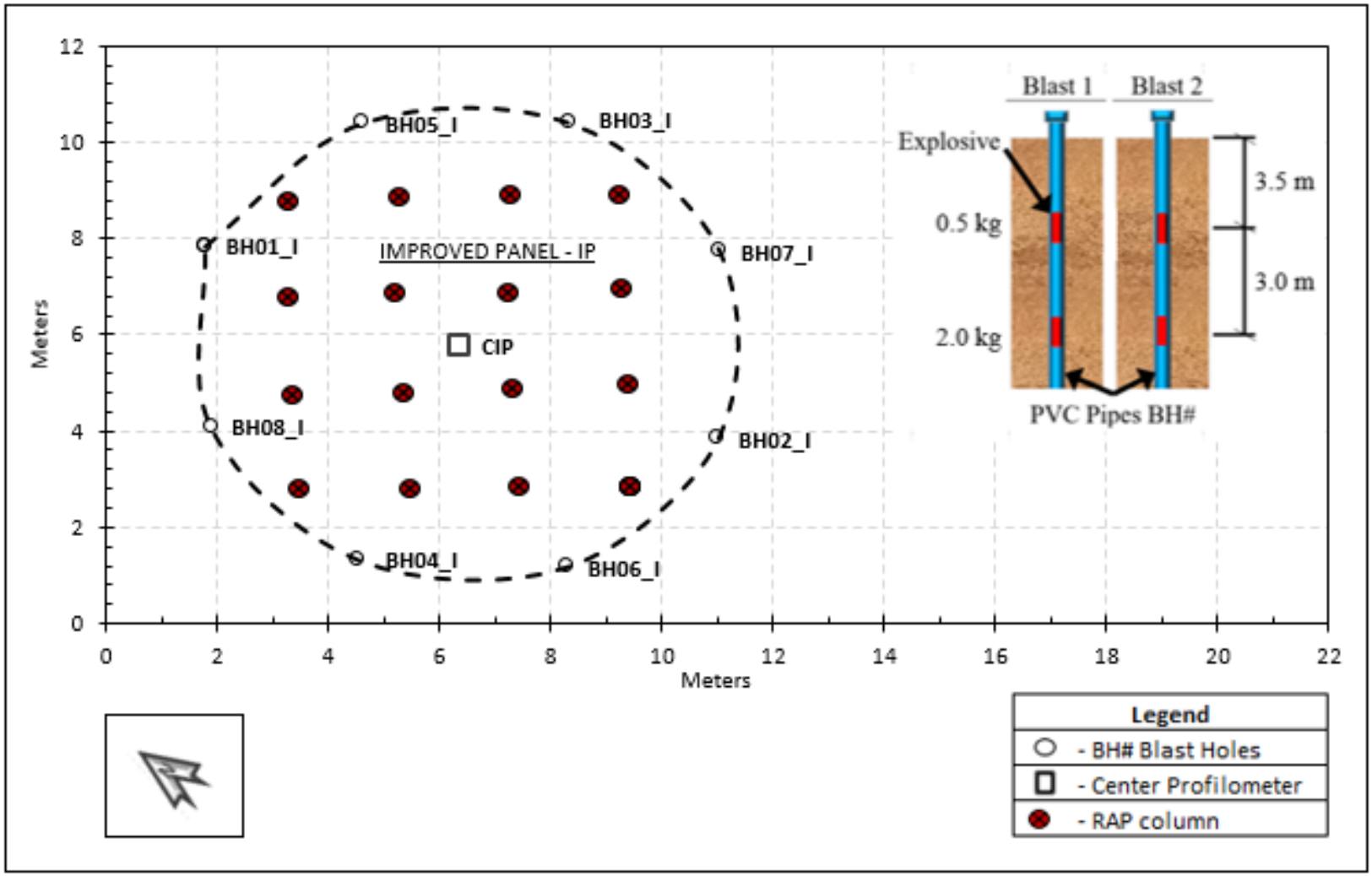

Figure 6.2: Blast hole placement in the IP with respect to the RAP columns.

6.2 Pore pressure instrumentation layout

Our BYU research team, together with GEO Geotecnica e Geognostica, installed pore pressure transducers (PPT) from 4 to 9 m at each meter of depth, within the liquefiable layer (1 or 2 m distance from the center of each panel). The PPTs obtained readings at a 100 Hz sampling rate and were used to measure the generation, and subsequent dissipation, of the excess pore pressures induced by the blasts at discrete depths within each of the panels. We set an extra PPT at a depth of 4 m near the middle of an accelerometer array mid-way between the two blast rings to study the non-linear soil behavior induced by the blast-liquefaction, coupling the shear strains with the excess pore pressures. Pore pressure data was necessary because the calculation of the excess pore pressure ratio (r_u), defined as the excess pore pressure (Δu) divided by the initial vertical effective stress (σ'_{vo}), can help determine if the soil layer has been liquefied. We installed the PPTs using the procedure described by Rollins et al. (2005), as follows. Six pore pressure transducers were placed around each center profilometer at depths of 4, 5, 6, 7, 8 and 9 m as shown in Figure 6.4. One PPT was placed at the center of the test field to observe pore pressures at a distance from the blast energy.

The transducers were housed in a protective cone-shaped casing to prevent damage to the fragile measurement diaphragm. We drilled holes into the cone tip before installation to allow pressure to easily reach the transducer. A rubber membrane was used when inserting the transducer into the bentonite slurry filled borehole to prevent any material of clogging the holes in the casing.

Amoroso et al. (2018) reported that the use of the rubber membrane did not prevent all instrument error due to clogging. In order to remedy this, we forced cotton into the drill holes in the casing. The pressure was still able to reach the membrane through the cotton, which provided a filter against clogging. Each PPT was installed by drilling a borehole filled with bentonite slurry to a depth 0.3 m above the intended PPT depth. Once the bottom of the borehole was reached, we pushed the PPT about 0.3 m which placed the transducer in the native soil as well as breaking the rubber membrane to allow the pressures to access the transducer. We kept each transducer connected to the computer program LabView throughout the duration of the blast activities Figure 6.3 below shows the typical installation diagram for the pore pressure transducers.

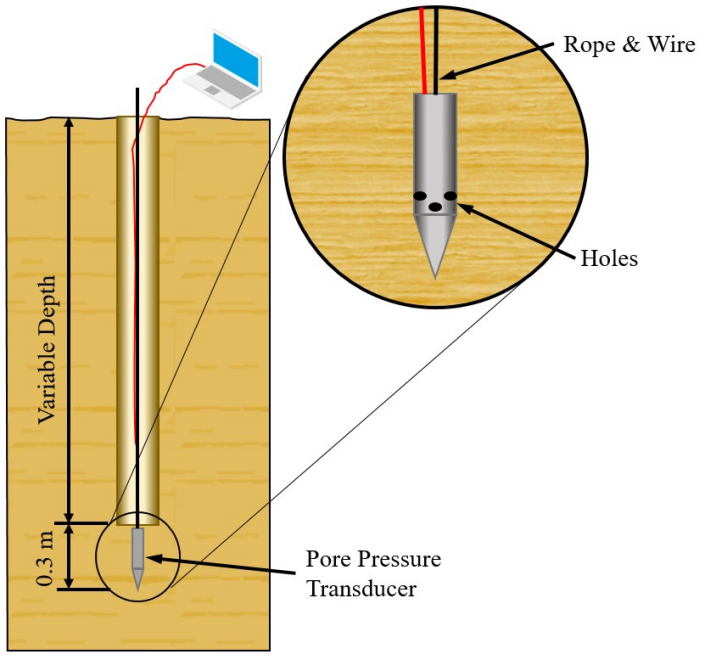

Figure 6.3: Typical PPT configuration showing the encapsulated PPT being placed at depth within a borehole encased with bentonite slurry (Modified after Lusvardi, 2019).

We selected the depths of the pore pressure transducers to attempt to quantify the pore pressures throughout the potentially liquefiable layers. Using measurements provided from two flat dilatometer test (DMT, Test: SDMT01_I, SDMT11_N) the following vertical effective stresses were determined for the various depths of the pore pressure transducers (PPT). The information gathered from the test is shown in Table 6.1 below. A plan view of the PPT placement in the NP and IP is provided in Figure 6.4.

Table 6.1: Initial vertical effective stress readings at each pore pressure transducer, in the NP and the IP, that were used in the computation of r_u during blast activities.

Natural Panel		Vertical Effective Stress	
Depth (m)	Soil Type	(kpa)	(psi)
4	Silty Sands	35.7	5.18
5	Silty Sands	44.5	6.45
6	Silty Sands	53.2	7.72
7	Silty Sands	62.9	9.13
8	Silty Sands	72.2	10.47
9	Silty Sands	81.6	11.83
Improved Panel		Vertical Effective Stress	
Depth (m)	Soil Type	(kpa)	(psi)
4	Silty Sands	35.7	5.18
5	Silty Sands	44.5	6.45
6	Silty Sands	53.2	7.72
7.3	Silty Sands	66.7	9.67
8	Silty Sands	72.2	10.47
9.2	Silty Sands	83.5	12.11

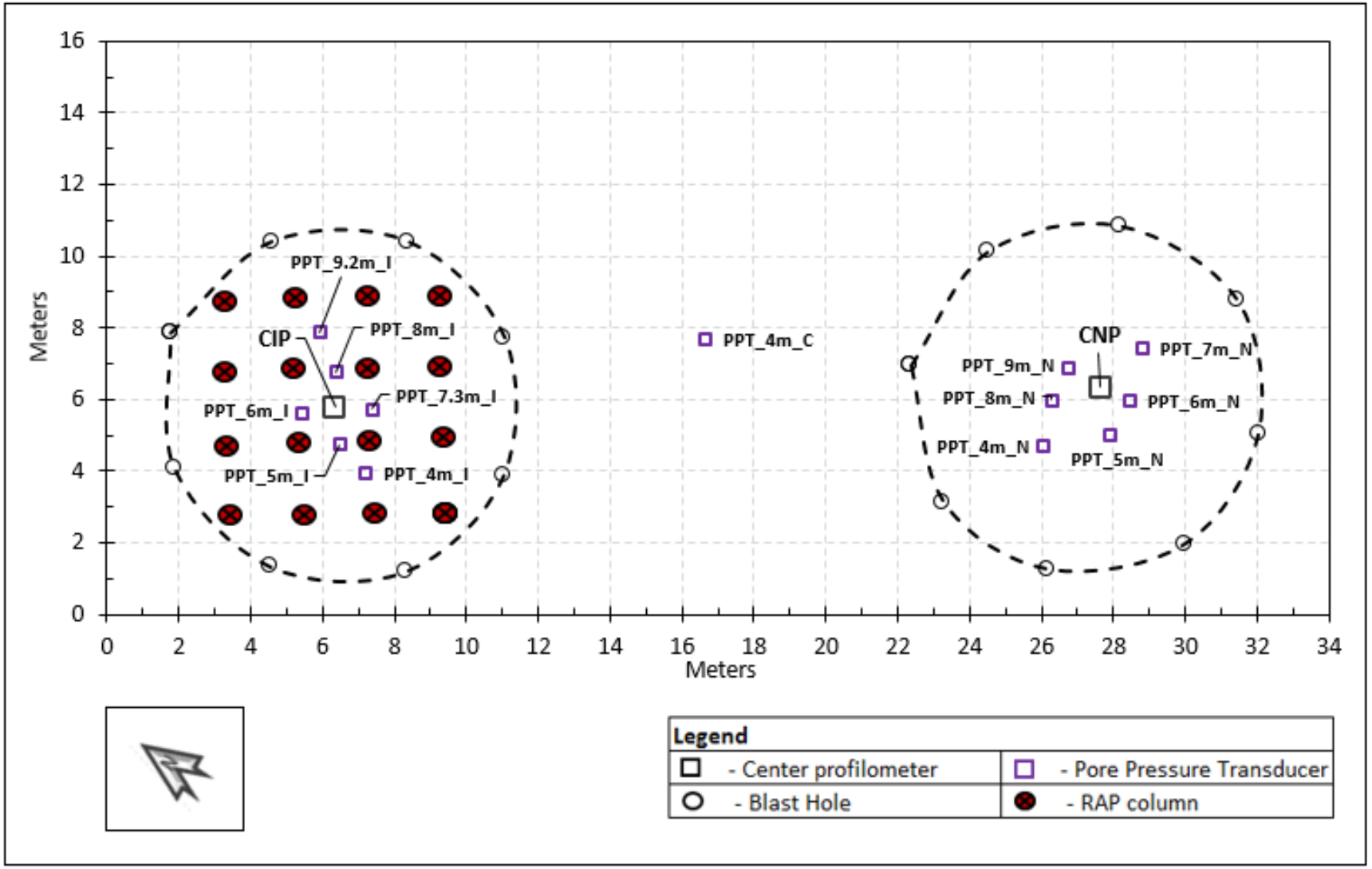

Figure 6.4: Plan view of PPT placement and their associated depth across the test site.

6.3 Settlement instrumentation and layout

Due to the nature of the study it was imperative to obtain accurate measurements of settlements caused by both blast sequences. We used monitoring systems to measure ground surface settlements, settlement vs. depth, and ground settlement vs. time. I will discuss the instrumentation for each separately.

6.3.1 Ground surface settlement

We monitored ground surface settlements across both the IP and the NP by means of sixty-two fixed elevation indicators, or stakes (ST), placed in a straight line through the center of both panels, which we surveyed manually at the site. We spaced the stakes at 1-m intervals across the site; however, within the blast rings (5 m of the center) we placed the stakes at 0.5 m intervals. We also used the PVC housing for the profilometer as an additional survey point so that the settlement at the very center of the panel was obtained as well. We used a barcode-type survey rod with an automatic survey level that provided 0.0305 cm (0.001 ft) accuracy. We surveyed these stakes prior to blasting and then approximately one half-hour after each blast sequence so as to record the incremental settlement caused by each blast sequence independently. Before each round of measurements was taken, two back-sight elevations were taken to ensure that the elevation of the tripod did not change. We assumed data points that oscillated around the origin by less than 2 mm to be zero to simply the settlement profile and account for minor movements in the survey stakes.

6.3.2 Settlement vs. depth

The arrangement of the blast charges was such that the maximum imparted energy would be felt in the center of the respective blast ring, and we anticipated that this would be the point of maximum settlement in both blast sequences. Within the IP, the point of maximum imparted blast energy also corresponds to the theoretical location of maximum improvement due to the RAP columns. At this location, in the very center of the RAP grid, we installed a profilometer as shown in Figure 6.5 to measure settlement with depth through the profile. The profilometer consists of a corrugated PVC drainage pipe prepared with circular steel zip ties that were attached to the outside of the tube at 0.5 m intervals. Using rotary drilling, GEO created a cased hole just wide enough to insert the corrugated tubing vertically to the hole's depth. Before insertion, an anchor was attached to the end of the tube. After the tube was installed, we inserted a PVC pipe smaller than the corrugated tubing vertically inside the length of the tube.

After installation, saturated sand naturally collapses around the corrugated pipe. During blasting and subsequent re-consolidation of the sand the corrugated pile can elongate or shorten with the strain of the soil surrounding it. The PVC pipe placed inside the corrugated tubing allowed the profilometer to remain vertical and aided in taking measurements with a Sondex measurement probe. The Sondex probe detects the elevation of the metal rings as it is lowered into the access pipe before and after blasting to define the liquefaction-induced settlement (Lusvardi, 2019). We labeled the profilometers as CNP for the NP and CIP for the IP. Each profilometer was outfitted with 30 rings and was embedded to approximately 15 m depth.

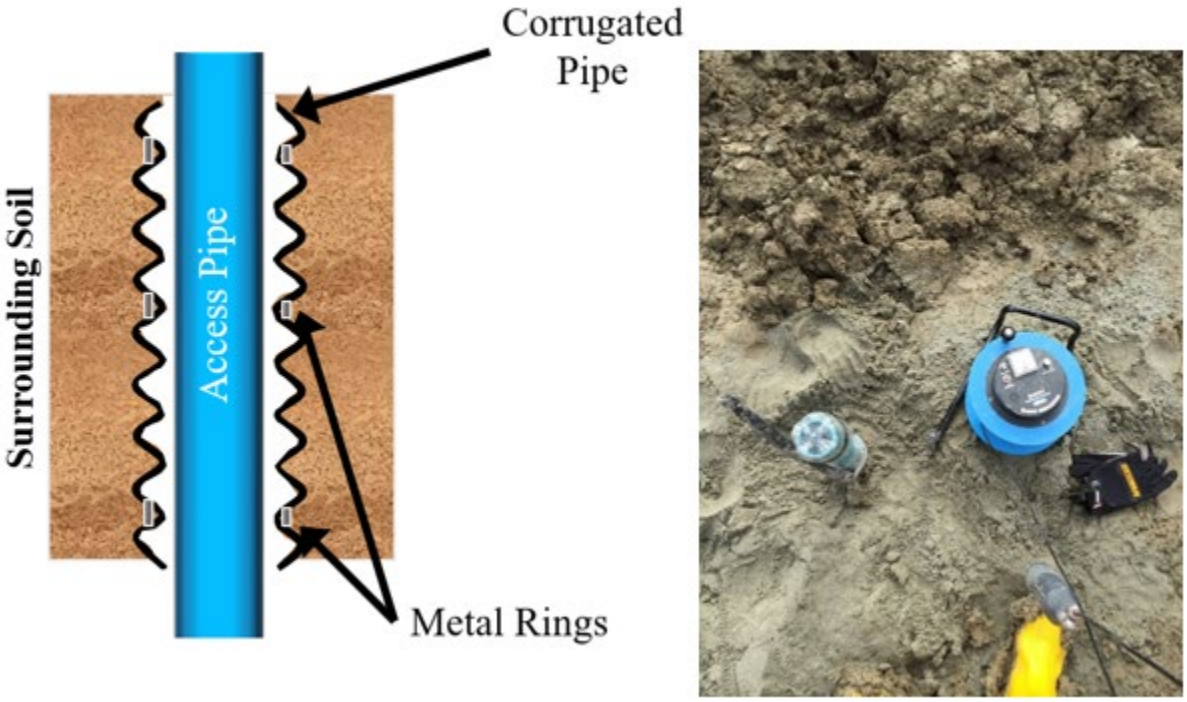

Figure 6.5: (Left) Cross-sectional view of the sondex profilometer, (Right) PVC access tube and magnet used to measure the depth of the metal rings (modified after Lusvardi, 2019).

6.3.3 Settlement vs. time

We also monitored ground surface settlements in real-time during and immediately following the blast sequence. We made these observations to provide some correlation between the rate of dissipating porewater pressures and the rate of settlement. To accomplish this real-time monitoring, we placed six blue PVC pipes perpendicular to the ground within the blast zone as shown in Figure 6.6 below.

Figure 6.6: Oblique view of the six blue PVC surface settlement rods, and the sixty-two surface settlements stakes, across the test field.

We embedded each survey rod approximately 0.8 m into the moderately compacted soil. We embedded the posts only within the surface clay layer inside the blast ring. To compact immediately surrounding the pipes we used hand tools in an attempt to minimize the disturbance of the natural condition of the soil, however settlement due to liquefaction within the clay layer was expected to be minimal, regardless of disturbance. We taped bar code segments to each pipe that could be read using automatic survey level. We positioned the autolevel tripod far enough from the blast rings to be unaffected by pore pressure induced settlement, and at what we determined to be a safe distance during and after the blasts. The accuracy that could be reasonably read from the survey level scope was to 0.0305 cm (0.001 ft). Before and after we recorded each round of measurements, back-sight elevations were recorded to adjust, if necessary, for any movement of the ground surface upon which the level tripod was placed. We labeled the six blue PVC surface settlement rods as shown in Table 6.2 below. We recorded the layout of the settlement

instruments, as herein described, using a high resolution GPS unit and can be seen in Figure 6.7 with respect to the blast rings of the NP and the IP.

Table 6.2: Locations of the six blue PVC surface settlement rods, and their respective distances from the Unimproved and Improved panels.

Marker	Distance from Center of Unimproved panel ft (m)
P1	1.64 (0.5)
P2	8.2 (2.5)
P3	16.4 (5)
Marker	**Distance from Center of Improved panel ft (m)**
P4	16.4 (5)
P5	8.2 (2.5)
P6	1.64 (0.5)

Finally, INGV also measured surface movements induced by the blast charge explosions and resulting liquefaction effects by means of Telestial Laser Scanning (TLS) and Structure from Motion (SfM) surveys performed before and after each blast test. In this way, multi-temporal point clouds before and after the blasts were obtained, leading to multi-temporal Digital Terrain Models (DTMs) whose comparison provided a well-defined pattern of ground subsidence. While the survey stakes provide a more accurate measurement of ground settlement along a line through the site, the TLS provided ground surface settlement contours over the entire surface of the test site. The TLS data were acquired by means of a Teledyne Polaris instrument (Teledyne 2019) mounted on a pole at about 6 m above the ground, using the Level Lift Roof device provided by Scan&Go srl (www.scan-go.eu).

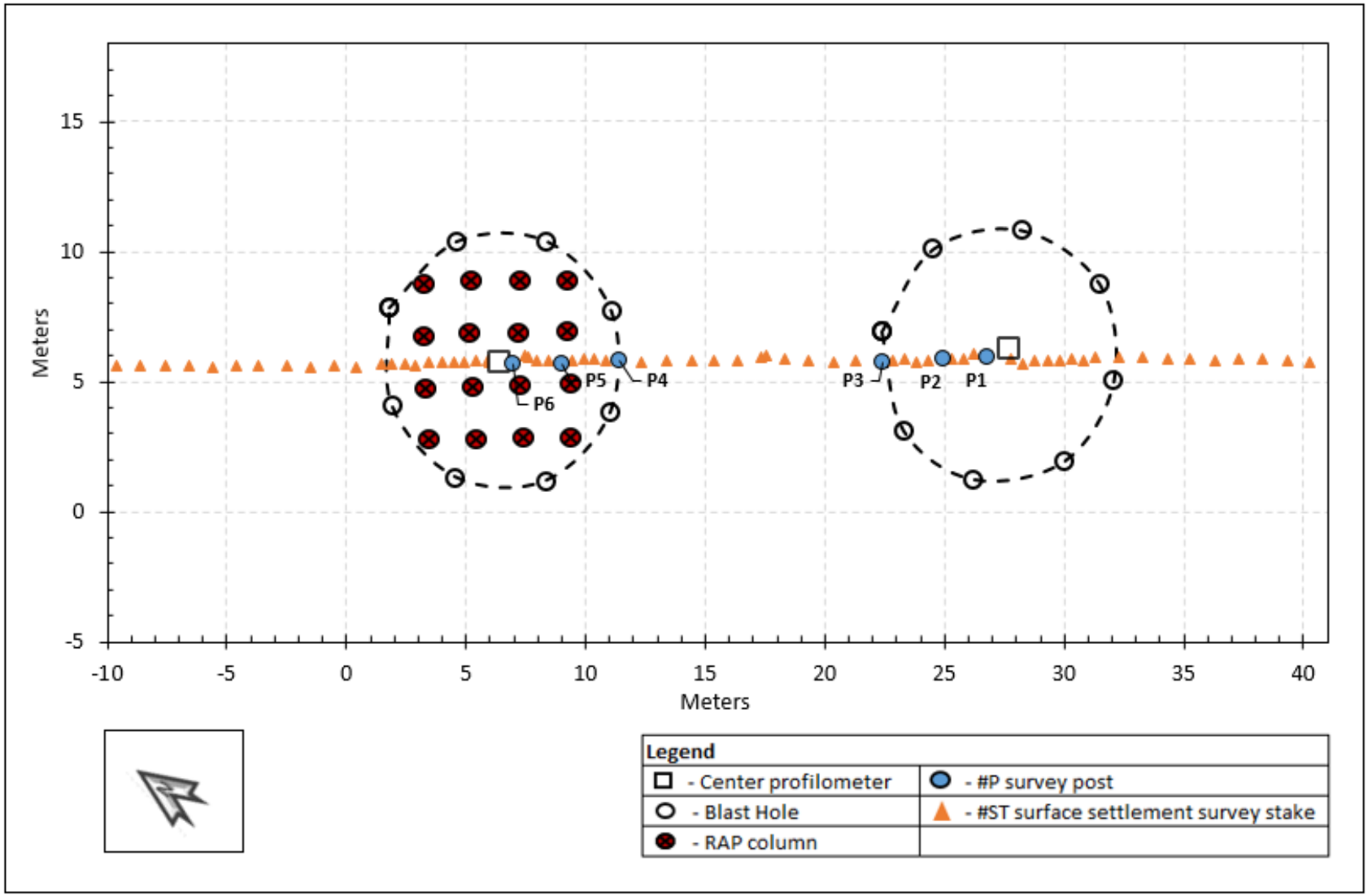

Figure 6.7: Locations of the surface settlement stakes and surface settlement rods across both the NP and the IP.

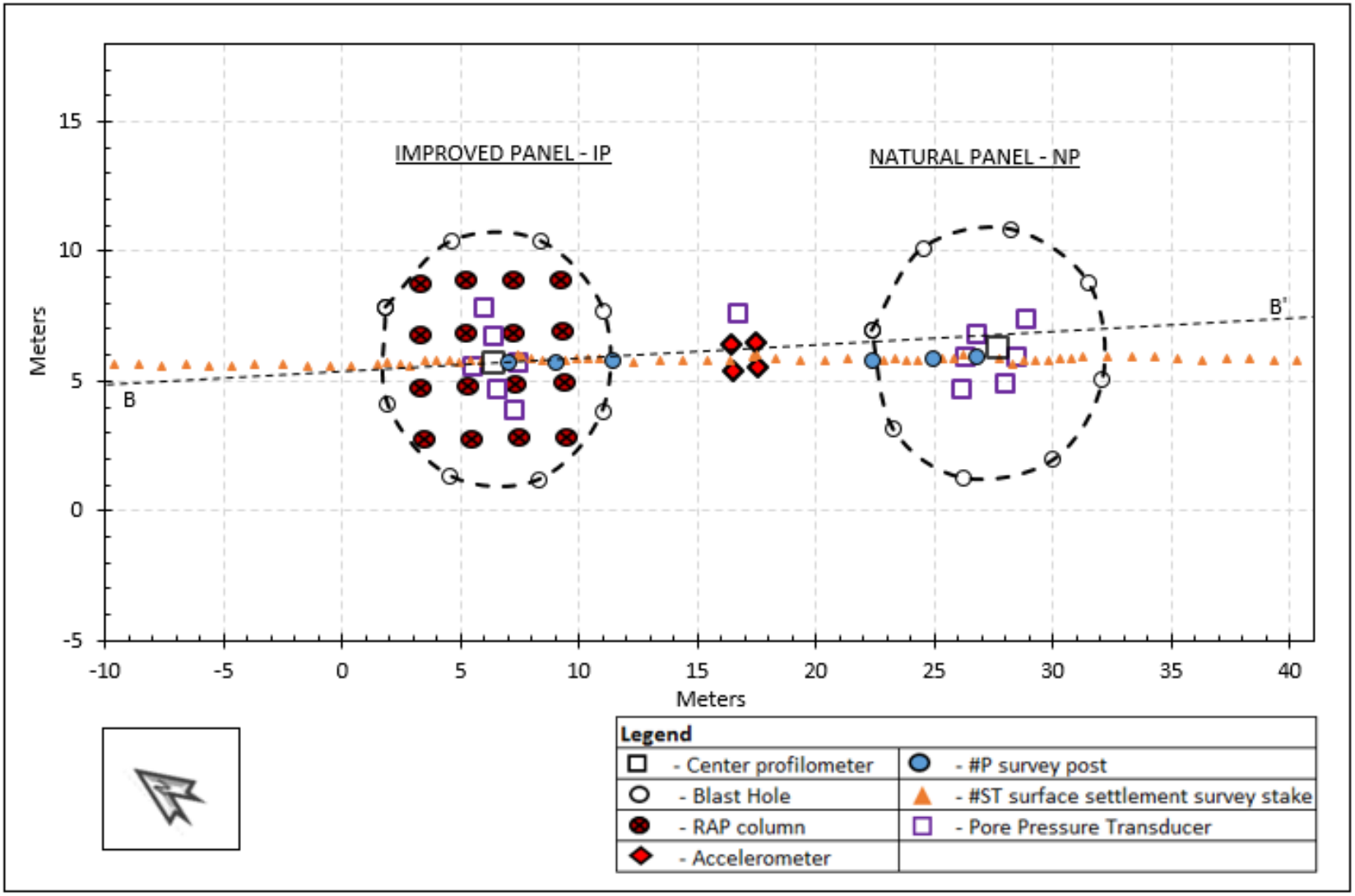

Figure 6.8: Locations of blast holes, RAP columns, pore pressure transducers, accelerometers, settlement instruments.

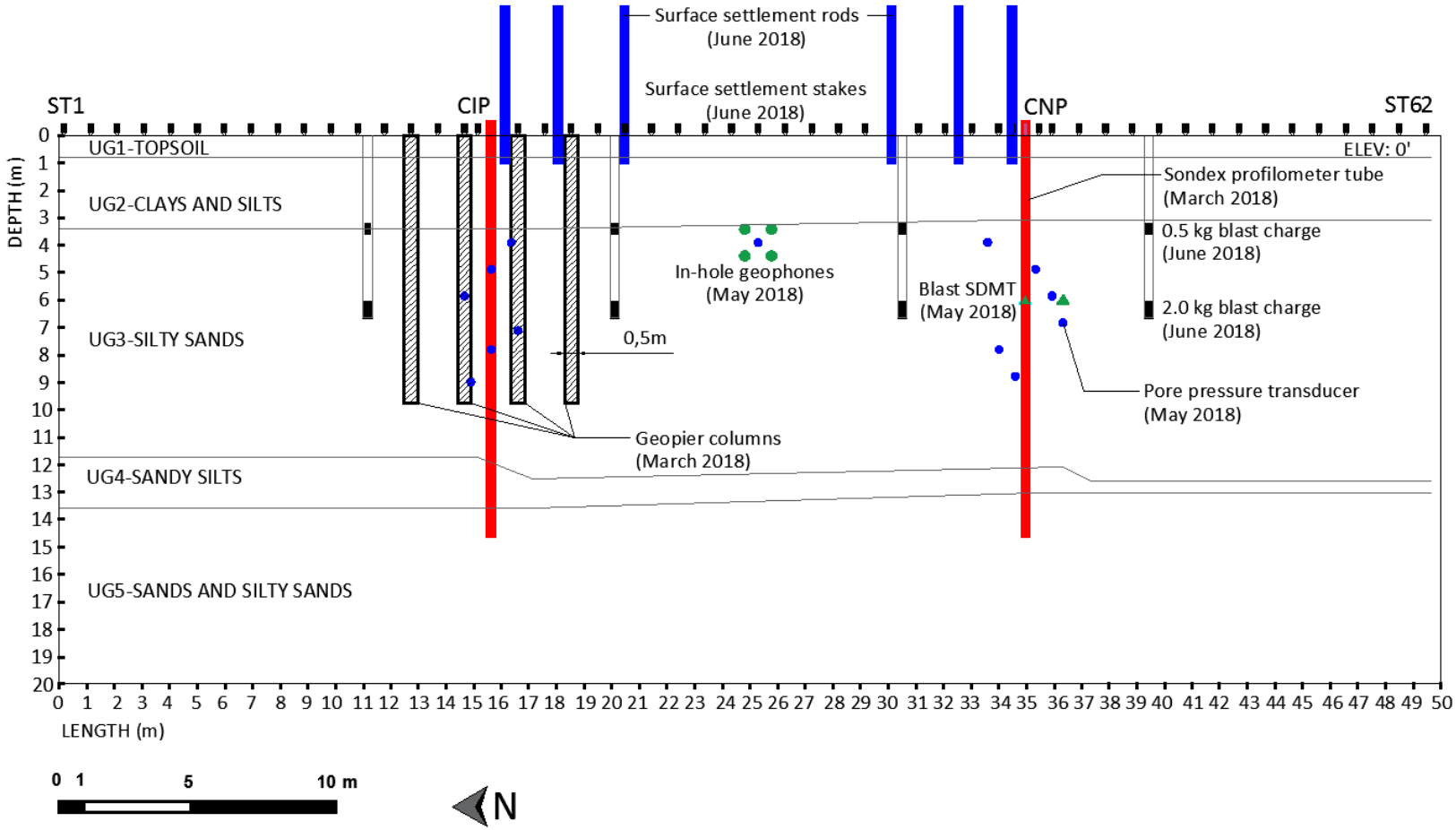

Figure 6.9: Simplified soil profile section B-B' showing the relative positions of the Improved Panel (IP) and the Natural Panel (NP), RAP column positioning, blast holes and other instrumentation at the site.

For each stage of the experiment, three scans were performed from three different points of view, along a side of the test site about 30 m long. Each scan was taken in about 5 minutes, leading to a dense point cloud with a 5 mm sampling step at the acquisition distance (100 m). The point clouds were aligned by means of the surface matching algorithm implemented in PolyWorks software package (Innovmetric 2019), leading to three multi-temporal point clouds subsequently registered into the WGS84 UTM32 reference frame thanks to 11 Ground Control Points (GCPs) whose positions were obtained by means of rapid static GNSS measurements. Point clouds were taken before and after each blast and differenced to obtain settlement after each blast and the total settlement.

At the same time, aerial SfM surveys were independently carried out by means of two Unmanned Aerial systems (UAS) equipped with DJI FC6310 and DJI FC350 camera respectively and flying, in both the cases, at about 20-30 m above the ground. For each flight, 50-60 images were taken and processed by means of the PhotoScan software package (Agisoft 2019), leading to the corresponding point clouds.

6.4 Additional instrumentation

In addition to finding a suitable settlement model for the RAP-treated soil, our research team had also planned to estimate blast-induced shear strains and shear stresses during the experiment. These data would allow our research team to use constitutive relationships to compute the actual in-situ cyclic stress ratio induced by the blast test. In theory, this would enable us to reconstruct the liquefaction assessment using actual stresses and strains and compare against the accuracy of the predictive models. This has never been done before in any previous full-scale blast

testing. If successful, this procedure could lead to advancements in the field of in-situ liquefaction assessment.

To obtain estimations of stresses and strains we relied on their relationships to acceleration, which could be more easily observed in the field. Accelerations were measured by INGV using four in-hole 200g triaxial microelectromechanical (MEMS) accelerometers, or geophones, (ACC1, ACC2, ACC3, ACC4) that were located at approximately the midpoint with respect to the two panels (i.e. about 10 m from CNP and CIP), using a 1 m-squared configuration between 3.5 and 4.5 m deep.

The complete pore pressure and surface settlement instrumentation layout is shown across the test site in Figure 6.8. A simplified soil profile drawing showing the section B-B' from Figure 6.8 of the test site after RAP and instrumentation installation is provided in Figure 6.9.

7 RESULTS FROM BLAST 1 AROUND NATURAL PANEL (NP) AND BLAST 2 AROUND IMPROVED PANEL (IP)

The pore pressure response and resulting settlement in the NP and the IP from the two identical blast events are reviewed, compared and contrasted in the subsequent sections.

7.1 Excess pore pressure measurements

Blast 1 occurred at 12:22:35 on June 4, 2018. During the experiment, as blast detonations occurred transient spikes in the excess pore pressure ratio were present. The transient spikes represent the rapidly arriving compression waves exerted by the blast. Because the transient spikes are relatively unimportant relative to the residual excess pore pressures, we smoothed the raw pore pressure measurements to remove the majority of transient pulses and to better represent the residual pore pressure by using a 100 point moving average.

The vertical effective stresses we determined from the SDMT as discussed above and shown in Table 6.1. An r_u of 1.0 would imply that the pore pressure from the water would equal that of the confining pressure at the depth. With both forces in equilibrium at the particle level liquefaction occurs in sandy soils (Seed and Lee 1966). An excess pore pressure ratio of 0.90 or higher suggests that the soil is essentially liquefied considering uncertainty in soil unit weight and other factors. The excess pore pressure ratio during blast 1 is plotted with time in Figure 7.1. The inset in Figure 7.1 is a zoomed-in scale showing the r_u values during the blast sequence for clarity.

The time is relative to the beginning of each blast sequence occurring at 0 seconds. Figure 7.1 shows that all of the pore pressures dissipate to initial static conditions within approximately 5 minutes after blast 1. The parallel rates of dissipation suggest that the soil profile largely exhibits behavior of a uniform soil type with depth. Fine-grained soil dissipates pore pressures slower than granular soil. Although the maximum excess pore pressures may vary over the depths, the dissipation of pore pressure occurred from the bottom up. This observation is anticipated since deeper depths have higher confining pressures, the magnitude of which are more difficult for the porewater pressure to sustain over time.

The r_u values recorded in the IP during blast 1 are shown in Figure 7.2. Excess pore pressure ratios within the improved area were negligible (less than 15%) during blast 1. The one exception is the sensor at 4 m which had a peak r_u of 30%. This could be due to the placement of the sensor at a depth that is coplanar with the blast charge. It is also likely due to the higher I_c value in this zone where the densification from the RAP column treatment was less effective.

For liquefaction design purposes, the maximum excess pore pressure ratio is the value of interest. When this value is greater than the predetermined liquefaction potential ratio then that soil layer has been liquefied. We plotted the maximum residual excess pore pressures recorded in both the NP and the IP vs. depth for blast 1 in Figure 7.3. In both the NP and the IP the 4 and 6 meter transducers heavily influenced the average peak r_u calculation because the blast charges were coplanar at this depth and caused higher r_u values. In the NP, the average peak r_u, excluding the 4 and 6 meter transducers, was 95%. In the IP the 4-meter transducer appears to have been most affected by the blast energy. The average r_u excluding the 4-meter depth was 15%.

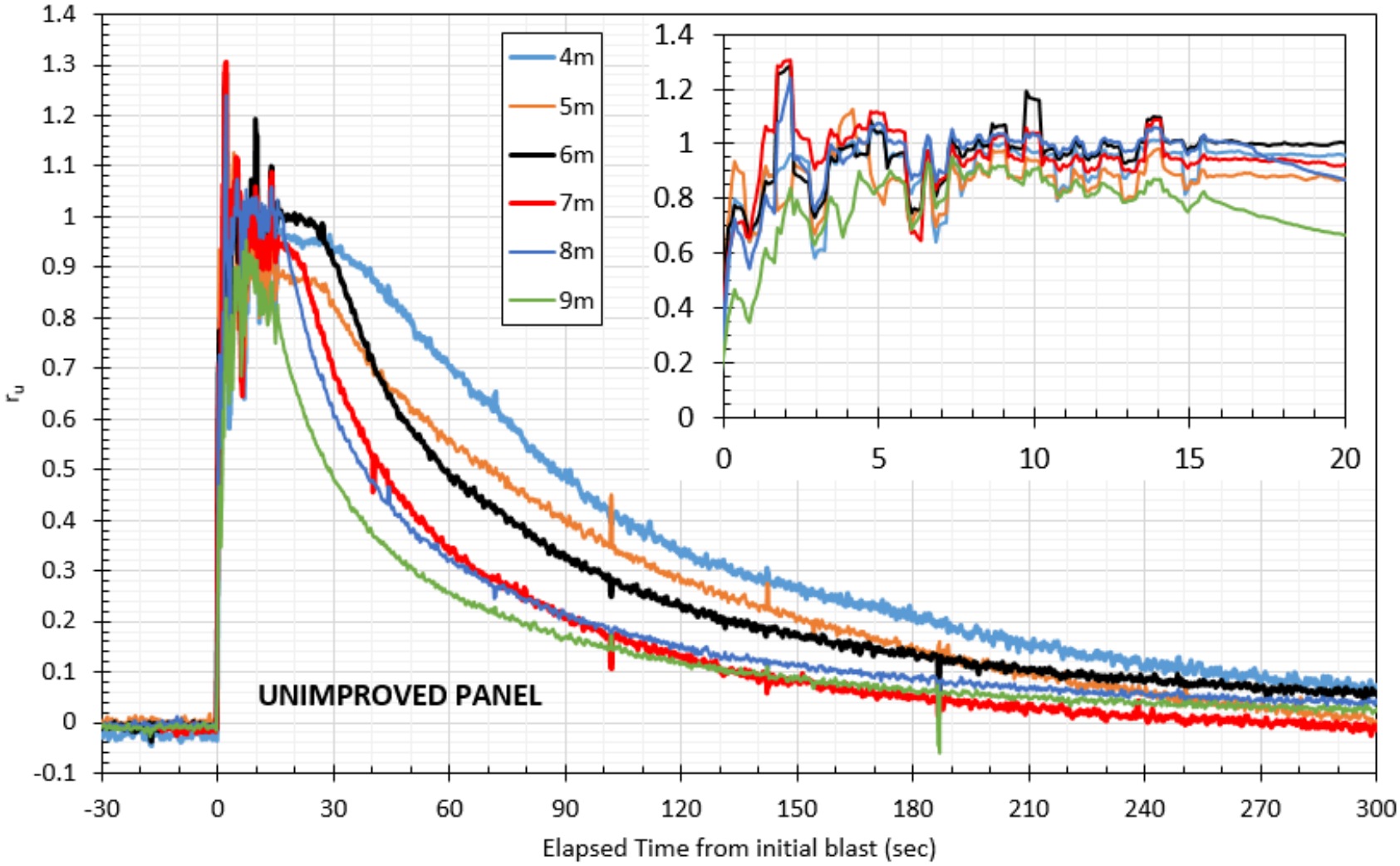

Figure 7.1: Residual excess pore pressure ratio in the NP during blast 1 in the NP at 4, 5, 6, 7, 8, and 9 m depths. Average peak residual pore pressure ratio with depth immediately during blast (shown inset).

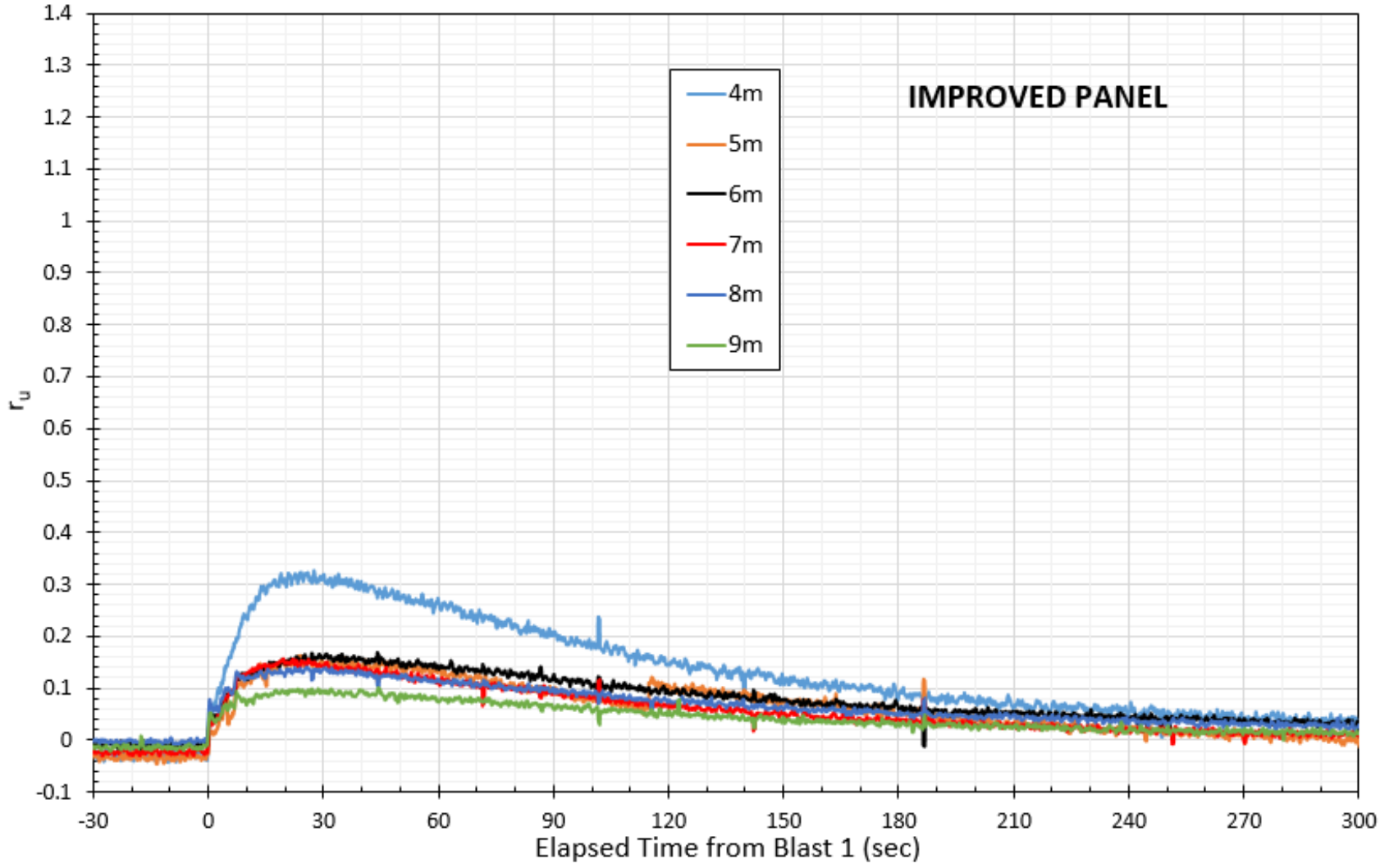

Figure 7.2: Residual excess pore pressure ratio in the IP during blast 1 in the NP at 4, 5, 6, 7, 8, and 9 m depths.

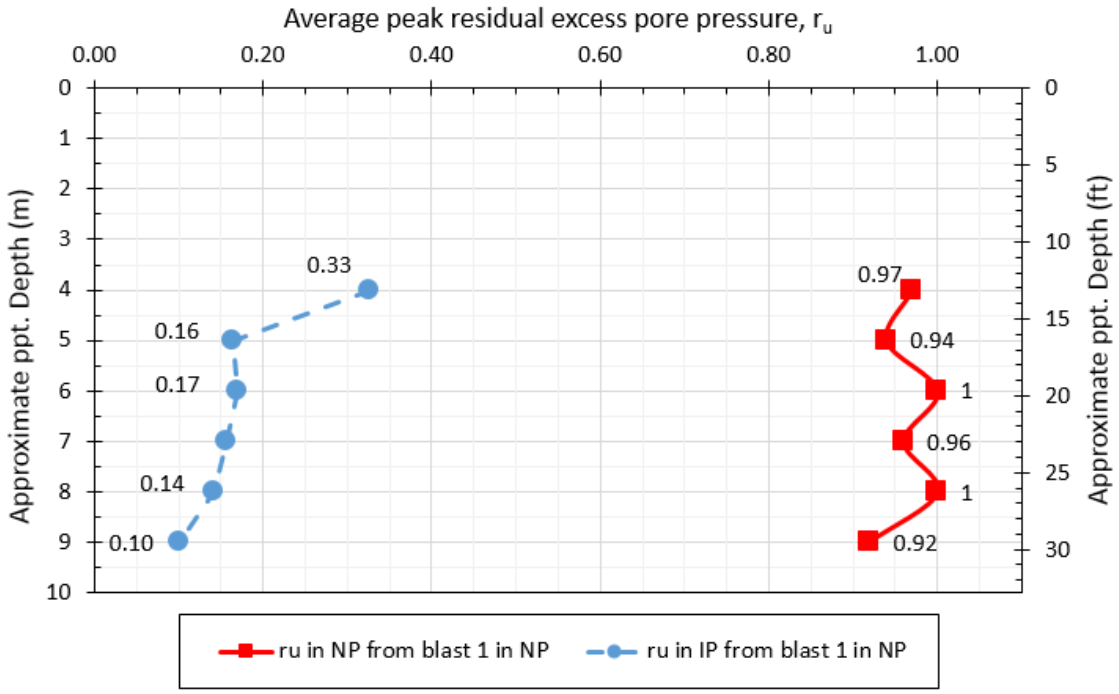

Figure 7.3: Comparison of peak excess pore pressure ratio, r_u, measured during blast 1 in the natural panel (NP) and in the improved panel (IP).

Blast 2 occurred at 15:24:56 on June 4, 2018, approximately 3 hours after blast 1 was triggered. We also smoothed the pore pressure data for Blast 2 to reduce transient spikes by using a 100 point moving average. Figure 7.4 below shows the excess pore pressure ratios vs time for the IP during blast 2. The time is relative to the beginning of blast 2 occurring at 0 minutes. The peak r_u values in the IP during recorded during blast 2 are generally lower than 1.0 indicating that the RAP columns were effective in reducing the generation of excess pore pressures. At depths of 5, 7, and 9 meters, the peak residual r_u was kept below the 80% limit for incipient liquefaction suggested by Studer and Kok (1980). The large r_u values observed at depths of 4 and 6 m are likely due to the placement of the blast charges at nearly corresponding depths. The r_u values dissipated mostly from the bottom upwards.

Figure 7.5 shows the excess pore pressure ratio in the NP during blast 2 in the IP. The r_u values generated in the NP during blast 2 were significantly higher than in the IP for blast 1, though

below the level for incipient liquefaction. Thus, it appears that the RAP treatment had some substantial effect in increasing the liquefaction resistance. The highest r_u values were recorded at 4 and 5 meter depths, near the depths where the charges were detonated.

We plotted the peak residual r_u for the IP and the NP during blast 2 in the IP versus depth in Figure 7.6. In the IP, the average peak r_u excluding the 4 and 6 meter transducers was 78%, which is below the level of incipient liquefaction. In the NP the average r_u value generated during blast 2, excluding the 4-meter transducer, was 25%. The accelerometer placed at the center of the test site, midway between the two panels, recorded r_u values of 100% during both blasts. Thus, it is apparent that the improvement was unable to dissipate the blast energy and excess pore generation felt outside of the treated area.

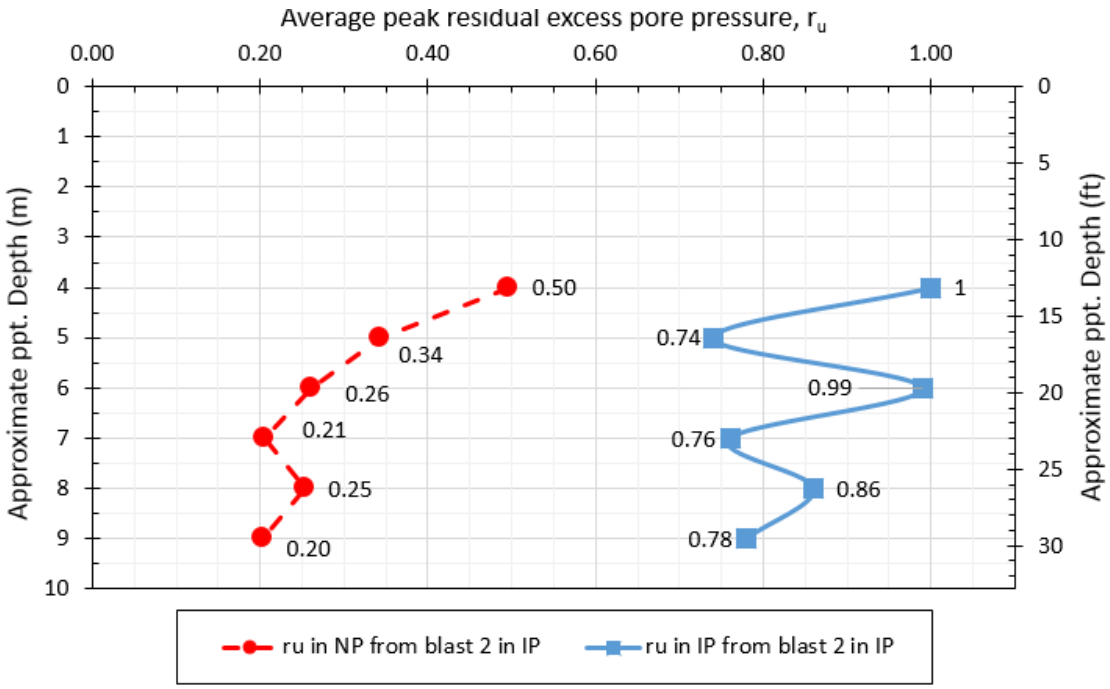

Figure 7.4: Comparison of peak excess pore pressure ratio, r_u, measured during blast 2 in the improved panel (IP) in the natural panel (NP).

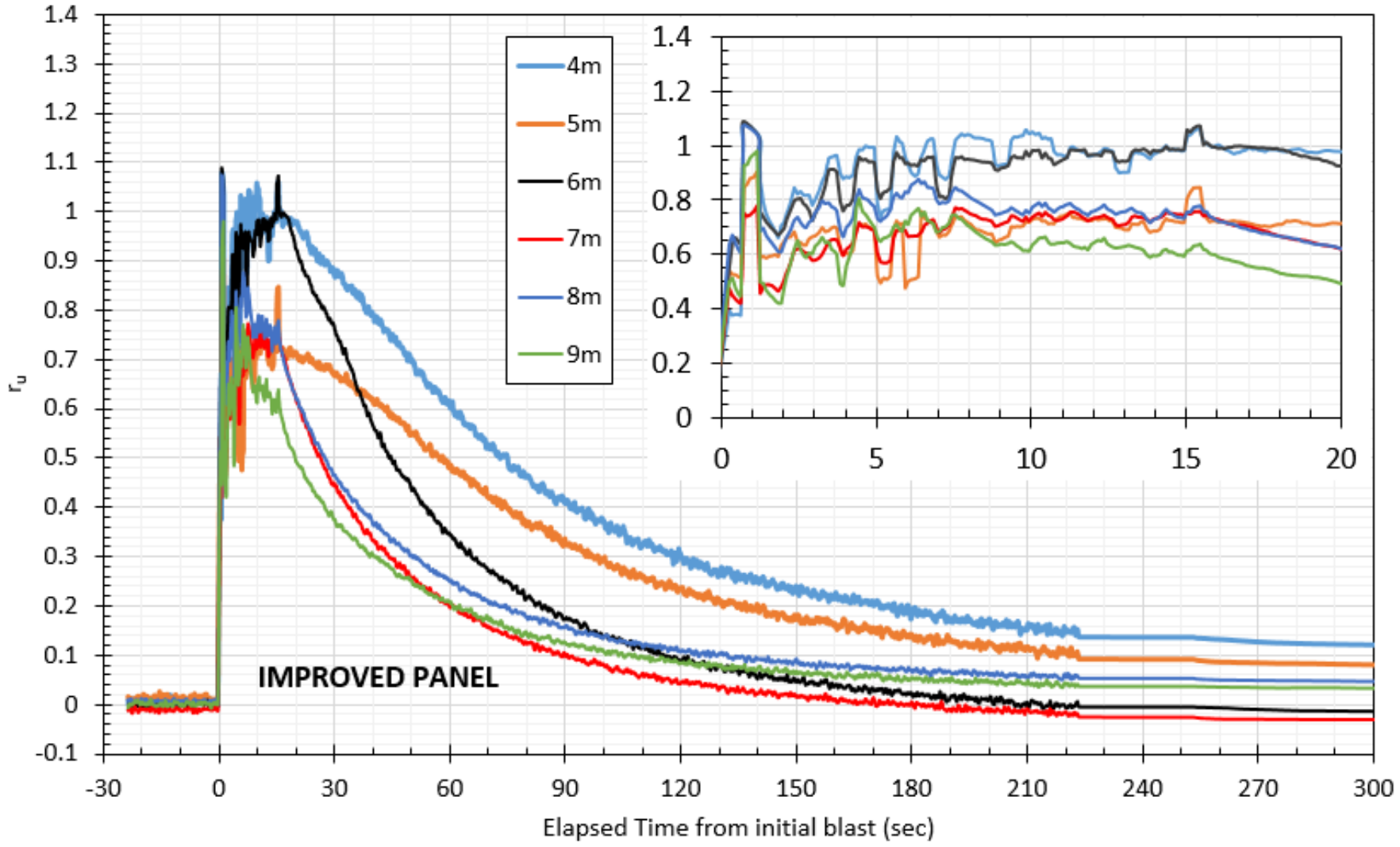

Figure 7.5: Residual excess pore pressure ratio in the IP during blast 2 in the IP at 4, 5, 6, 7, 8, and 9 m depths. Average peak residual pore pressure ratio with depth immediately during blast (shown inset).

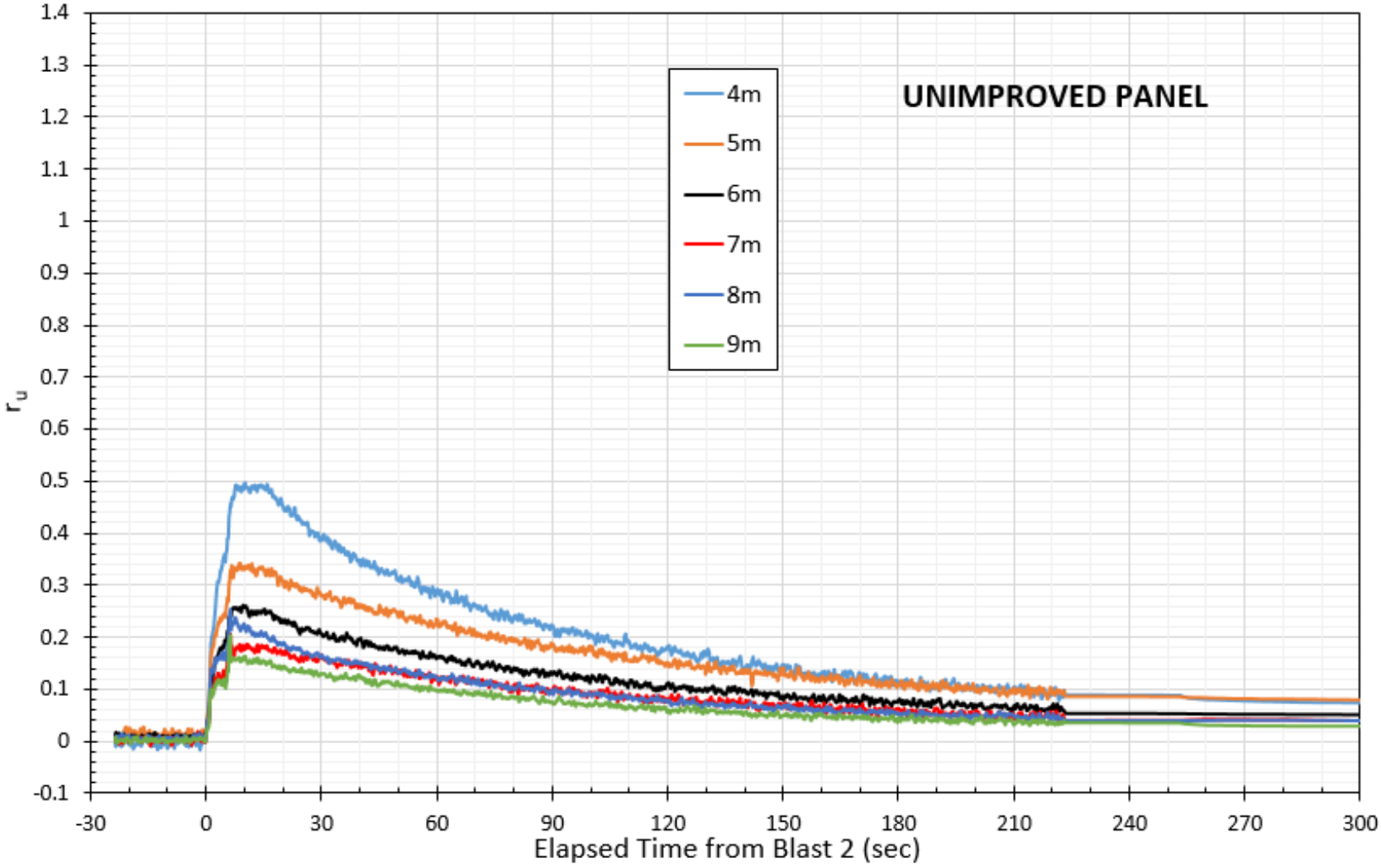

Figure 7.6: Residual excess pore pressure ratio in the NP during blast 2 in the IP at 4, 5, 6, 7, 8, and 9 m depths.

We plotted the peak residual r_u for the IP versus depth relative to the NP in Figure 7.7. In the NP during blast 1 the peak measured r_u values are close to 1.0 from 3 to 9 m indicating liquefaction. In contrast, the peak r_u values in the IP during blast 2 are generally lower than 1.0 indicating that the RAP columns were effective in reducing the generation of excess pore pressures. Significant r_u reductions from NP are seen at depths of 5, 7, and 9 m. At these depths the peak residual r_u was kept below the 80% limit for incipient liquefaction suggested by Studer and Kok (1980). The large r_u values observed at depths of 4 and 6 m are likely due to the placement of the blast charges at nearly corresponding depths. In the NP, the average peak r_u excluding the 4 and 6 meter transducers was 95%, compared to 78% in the IP. During the blast sequence on the opposite side of the field both the NP and the IP did experience some level of r_u generation. Figure 7.7 shows that the r_u values were higher in the NP than in the IP, though they were below the level for incipient liquefaction.

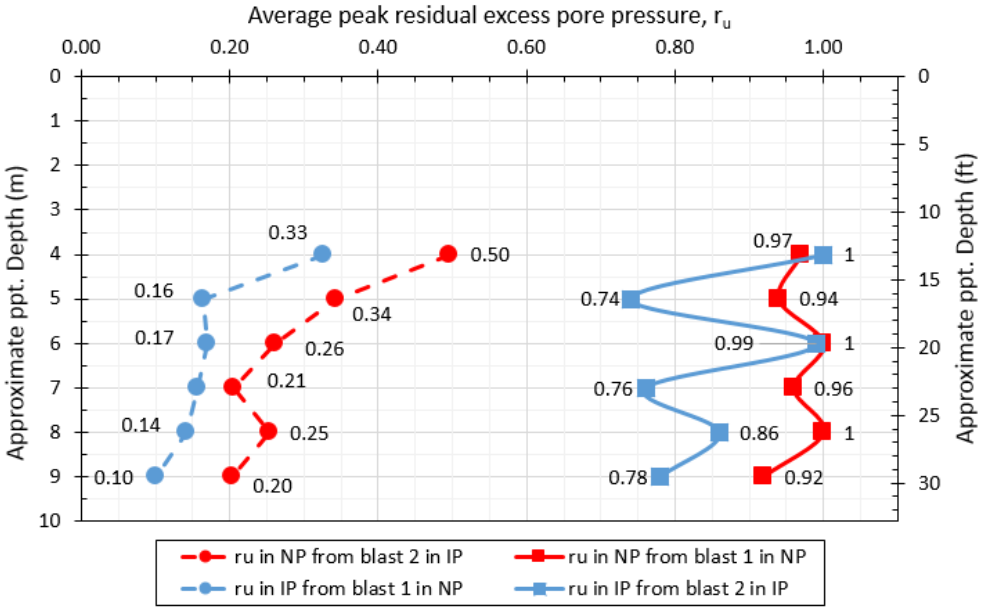

Figure 7.7: Comparison of peak excess pore pressure ratio, r_u, measured during blast 1 in the natural panel (NP) and blast 2 in the improved panel (IP).

At both panels, excess pore pressures rapidly developed after a few seconds and remained at their peak for 15 to 20 seconds before dissipating as shown in Figure 7.8. The r_u values dissipated from the bottom upwards and decreased to essentially static levels within about 6 minutes after blast detonation. In the improved panel, the blasting sequence generated somewhat lower peak r_u values and the dissipation rate was somewhat more rapid in comparison with the natural panel.

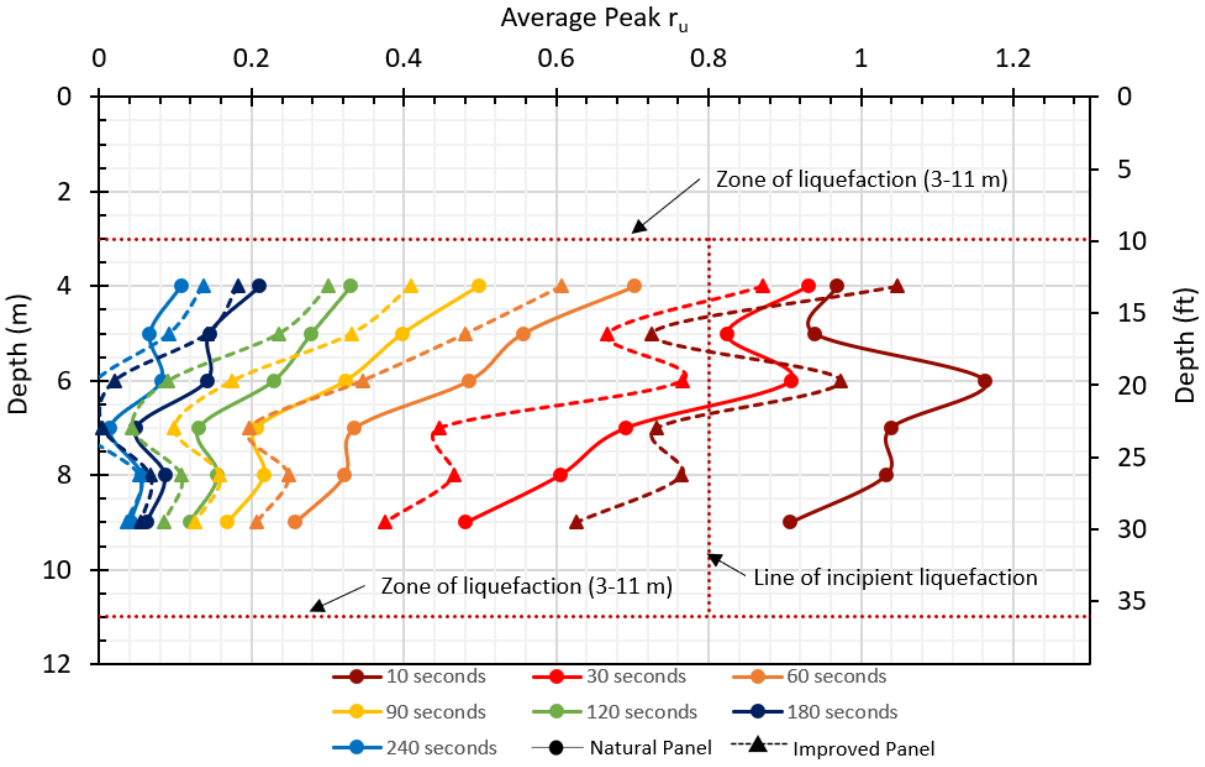

Figure 7.8: Dissipating r_u values with depth between 10 and 240 seconds after triggering blast 1 and blast 2, respectively.

7.2 Sand ejecta

Following blasting, several large sand boils developed within the blast ring in the natural panel as shown in the photo in Figure 7.9. These characteristic liquefaction features graphically confirm the results of the pore pressure measurements. Mineralogical evaluation of the ejecta from

the sand boil with sand from SPT testing indicates that the ejecta likely came from liquefaction in the depth interval between 3 and 9 m. (Fontana et al. 2019).

In contrast to the natural panel, no sand boils formed within the area treated with RAP columns, although smaller sand boils developed outside the treated zone. Considering that the development of ejecta was a major cause of building damage during liquefaction in the Christchurch earthquake sequence (van Ballegooy et al. 2014), this appears to be an important benefit of RAP treatment. Examples of the observed sand boils are shown in Figure 7.9. The location of the sand boils after blast 1 and blast 2 are shown in the aerial survey of Figure 7.10. Many of the sand boils occurred at the blast holes which served as a conduit to the ground surface. These characteristic liquefaction features graphically confirm the results of the pore pressure measurements.

An important contribution of this test is that it serves as another successful case history of using blasting methods to recreate liquefaction effects in a full-scale study.

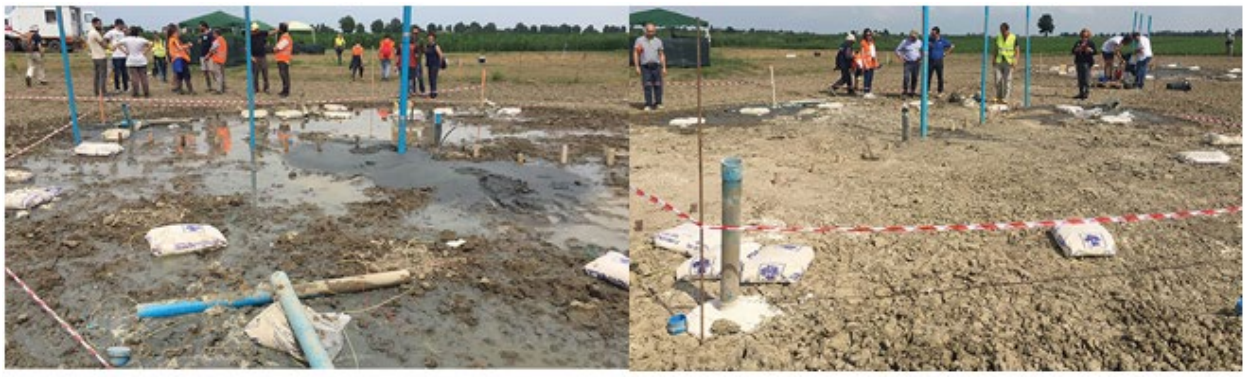

Figure 7.9: Comparison of observable liquefaction effects in the NP (left) after blast 1, and the IP (right) after blast 2 (http://www.releo.it/blast-test-impact-pier.php).

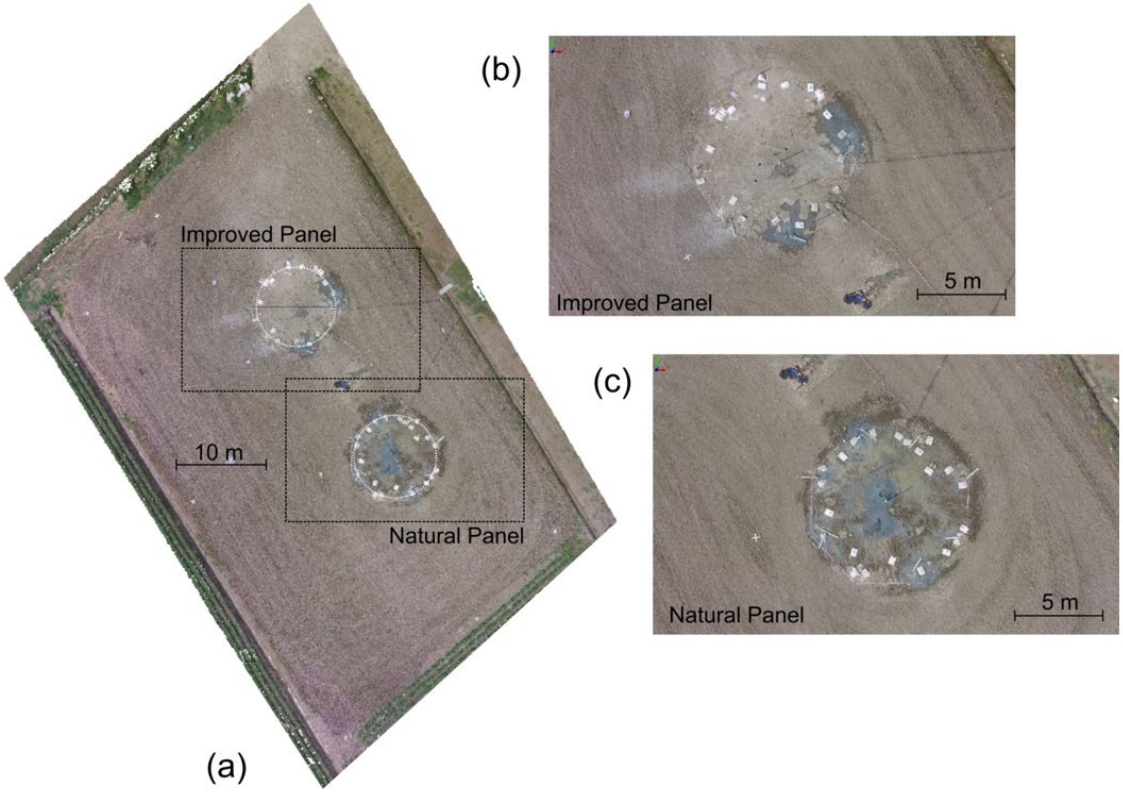

Figure 7.10: (a) Aerial photograph of the test site after both blasts, (b) location of sand boils with respect to the IP, (c) location of sand boils with respect to the NP (after Amoroso et al., 2019).

7.3 Pore pressure induced settlements

This section will report the ground surface settlements measured in real time during and after the blast, the fully developed ground surface settlements, and the settlements observed with depth.

7.3.1 Real time measurements

The real-time measurements from blast 1 cover a period of about 86 minutes after the blast. Figure 7.11 (a) shows a plot of the total recorded settlements with time for blast 1. We took the initial reading before blast 1 and the final reading when incremental settlement readings were below 1%. The slope of the settlement line seems to indicate that given more time the profile may have continued to settle, perhaps several more millimeters. However, our reading taken prior to blast 2, 3 hours after blast 1, determined that less than 0.05 cm additional settlement had taken place. Since the incremental settlement was at the limits of our instrumentational accuracy, we determined that the maximum settlement in the NP had occurred by 86 minutes after blast 1. From these measurements it can be seen that between 65%-80% of the total settlement occurred within the first two minutes, and within 13 minutes approximately 95% of the total settlement occurred.

In a liquefaction event excess porewater pressures (r_u) build and momentarily suspend the soil particles by reducing the effective stress. As the r_u dissipates, reconsolidation of the soil particles occurs and causes settlement. In order to see the rate of settlement against the rate of r_u dissipation, we normalized the same ground settlement from the PVC rods against the maximum recorded settlement and plotted against the average r_u values as recorded by the six PPT in the profile which were discussed previously. After normalization the plots from P1, P2 and P3 plot on top of each other. As seen in Figure 7.11 (c) the average excess pore pressure ratio between 4 m and 9 m depth had dissipated to 60% within 1 minute of the final charge of the blast sequence. By

two minutes after the final blast charge the average r_u was 20%, and 15 minutes after the final blast charge average r_u values were nearly returned to zero. As anticipated, the normalized settlement lines nearly parallel the average r_u line, demonstrating that the recorded settlements were caused by dissipating r_u values.

The second blast measurements cover a shorter period of 30 minutes since the incremental settlements became negligible quicker than they did in blast 1. Figure 7.11 (b) shows a plot of the recorded settlements at the three posts (P4, P5, P6) in the IP. We took the initial reading just before blast 2 and the final reading approximately 30 minutes after the conclusion of the blast sequence. Further recording of the settlements was also complicated by the arrival of a large rainstorm and the necessity to immediately remove equipment from the field to protect it from rain and wind damage.

As with the NP, we recorded the normalized settlement with time after blasting for the IP and is given in Figure 7.11 (d). After normalization the plots from P4, P5 and P6 mirror each other, though not as tightly as do P1, P2, and P3 after Blast 1. In addition to reducing the total settlement, the RAP improvement also reduced the time over which the settlement occurred. Within only 8 minutes approximately 95% of the settlement in the IP was completed, which is approximately 60% of the time required for 95% settlement in the NP. The increased rate of settlement is likely a combination of lower peak excess pore pressures, a lower modulus of compressibility and horizontal drainage to the RAP columns in the improved panel.

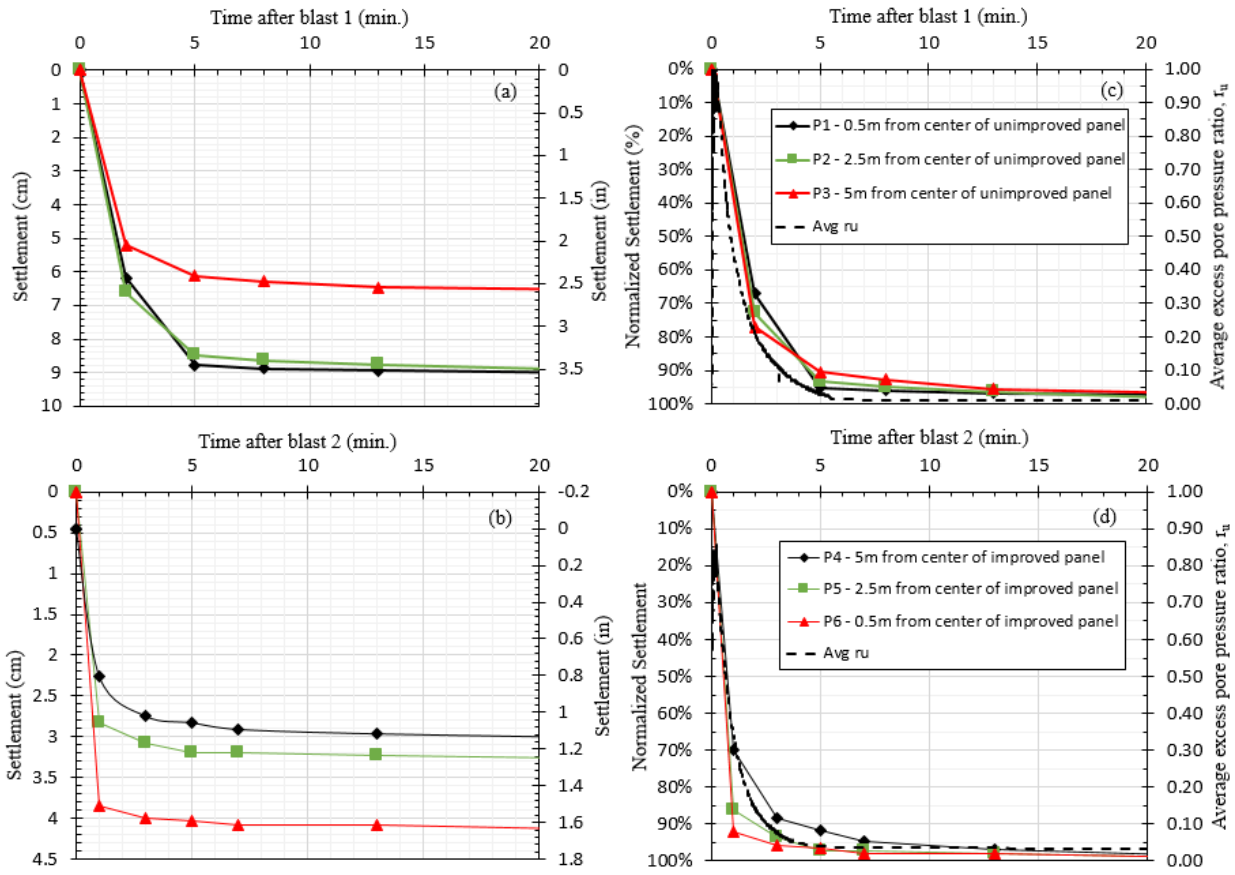

Figure 7.11: (a) Measured ground settlement with time for the NP during blast 1 and (b) for the IP during blast 2. Normalized ground settlement and average r_u for the (c) NP in blast 1 and (d) the IP in blast 2.

7.3.2 Fully developed ground surface measurements

We recorded ground surface settlements at the sixty-two survey stakes (ST). The recordings were made between 30 minutes and 60 minutes after the first blast test was concluded when excess pore pressure had fully dissipated. Reconsolidation following blast-induced liquefaction produced a nearly symmetrical dish-shaped settlement pattern across the NP as shown in Figure 7.12. Maximum settlement at the center of the blast ring was about 95 mm and settlement decreased to zero at a distance of about 12 m from the center of the array. Settlements within the

blast ring were between 70 and 95 mm after blast 1. As anticipated, the location of maximum settlement in the NP corresponds with the highest imparted blast energy, as well as the placement of the profilometer where we recorded settlement with depth.

Elevation change was also measured by INGV using terrestrial laser scanning (TLS) and color contours of settlement after blast 1 (B1-B0) are provided in Figure 7.13. The settlement contours indicate a circular dish-shaped settlement pattern in the natural panel similar to the autolevel, but the TLS settlements are somewhat lower. This is because sand ejecta accumulating at the ground surface decreases the settlement recorded by the TLS relative to that from the survey stakes. The TLS survey also confirms the autolevel readings that no settlement occurred in the IP as a result of blast 1. Additional details about the TLS based settlement are provided in Amoroso et al. (2019).

We re-surveyed the surface stakes between approximately 30 minutes to 60 minutes after the blast sequence around the IP. The settlement caused by the second blast alone is shown in Figure 7.14. The second blast series caused some additional settlement on the side of the NP and within the zone between the NP and the IP, which could have been due to strain softening during the first blast sequence. Within the IP the ground surface settlement from the second blast sequence did not exhibit a symmetric settlement profile, as did the blast sequence in NP. Unlike the NP, the peak settlement value did not occur at the center of the blast ring, or the center of the improvement zone. The maximum amount of settlement occurred at approximately 4 m to the north of the CIP. At the location of maximum settlement approximately 5.2 cm of settlement was recorded, compared to only 4.0 cm at the location of the CIP.

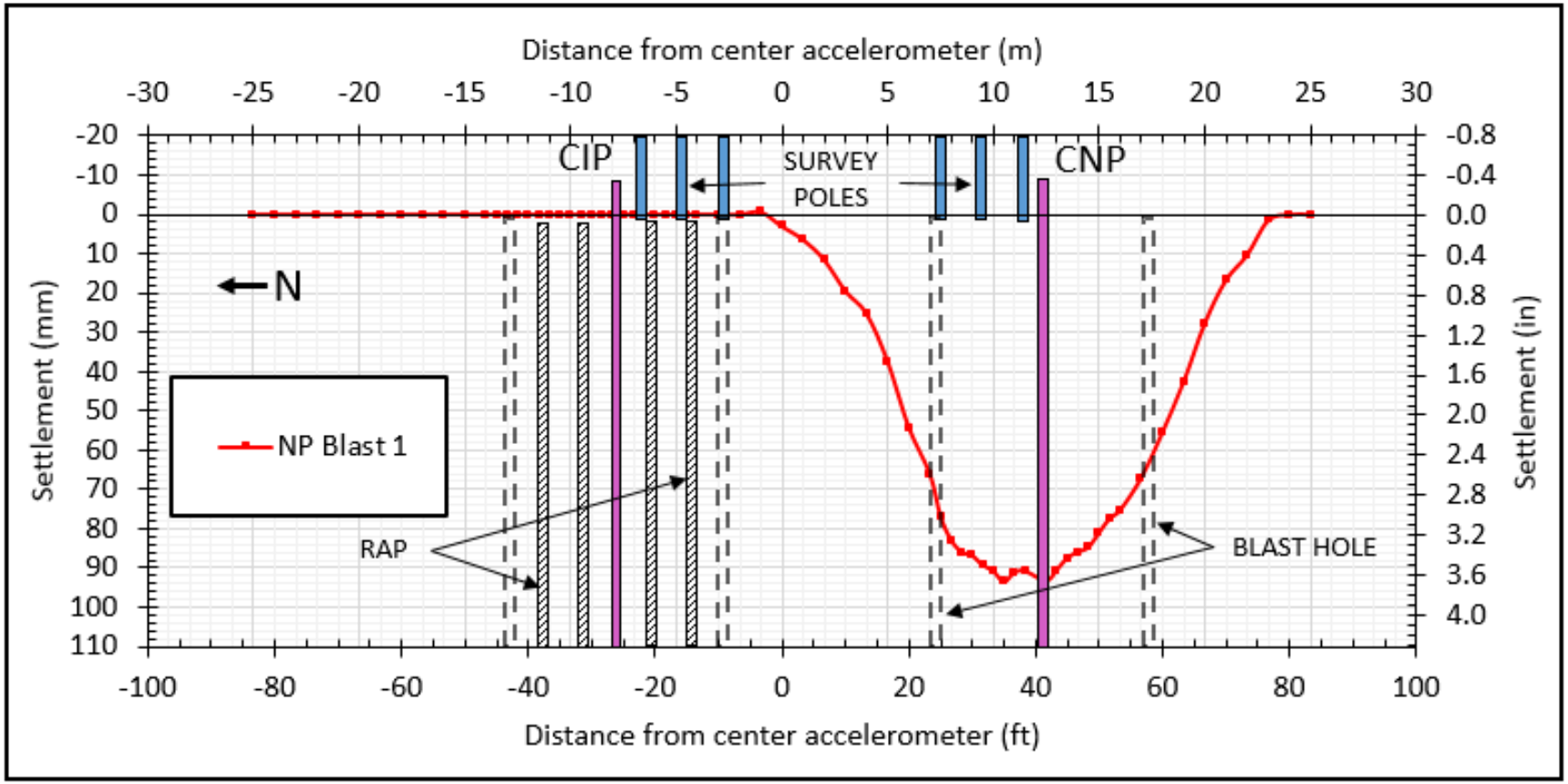

Figure 7.12: Ground surface settlement measurements obtained 30 minutes after blast 1 in the NP.

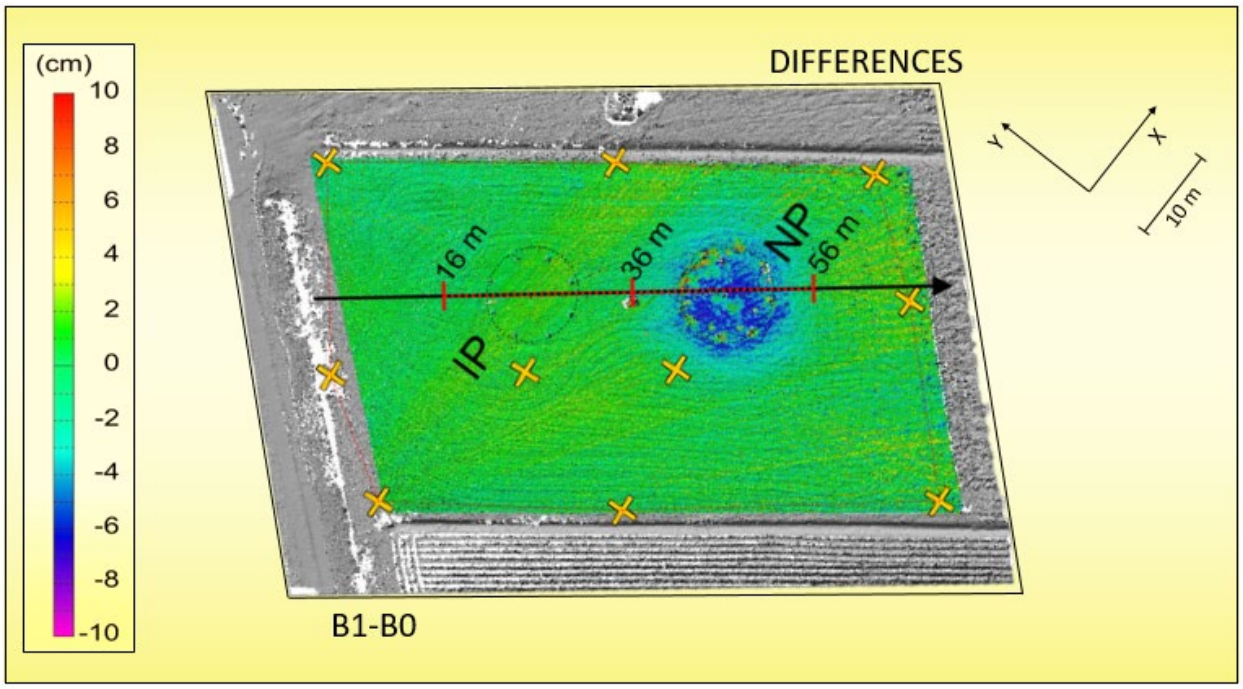

Figure 7.13: Color contour map from TLS surveys of settlement due to blast 1 in the NP (Modified after Amoroso et al., 2019).

The far north side of the IP returned to zero settlement at a rate similar to the far south side of the NP after Blast 1. One likely explanation for these higher settlements is inconsistencies in construction quality during RAP installation. The crowd test results provided in Table 5.1 demonstrate that the RAPs on the northeast side of the IP, that were the first to be constructed, settled more during crowd tests than the other RAPs in the grid. This lower RAP quality apparently led to lower RAP column stiffness and less densification around these columns during treatment. This result points to the need for quality control to ensure consistent ground improvement. It is also possible that variability in the soil profile could account for some of the differential settlement. The cross-sectional view provided by the Electrical Resistivity Tomography lines of Figure 6.9 indicate that the sandy silt layer between 12-13 m depth is slightly thicker on the north side of the RAP group. Due to constraints no in-situ investigations could be made at these locations since the objective of the research was to understand settlements at the center of a RAP group. As such, it

is not understood if the differential thickness of the sandy silt layer was a primary factor in the observed settlement distribution across the test site.

The TLS survey after blast 2 and the settlements due to this isolated blast (B2-B1) were mapped across the test site as shown in Figure 7.15. The TLS survey highlights the higher settlements recorded in the northeast sector of the IP. This survey provides evidence that the earlier constructed RAP columns may not have performed as well as others constructed later in the process. Both the TLS and the autolevel surveys confirm that the settlement in the IP was between 20 and 50 mm, which is considerably less than that in the natural panel. For the purposes of this thesis, we used the measured settlements by the ST and the CIP to perform an analysis of the observed settlement. The TLS readings provided validation for our research team that our measurements were accurate.

The cumulative settlement caused by both blast 1 in the NP and blast 2 in the IP, is plotted across the test site in Figure 7.17. The greatest settlement was produced within the NP, with about 50% less settlement occurring in the IP Another TLS survey was performed after blast 2 and the settlements were topographical elevation difference between after blast 2 and before all blast activities (B2-B0) was calculated. Both the TLS survey from Figure 7.16 and autolevel surveys confirm that the settlement in the IP was between 20 and 50 mm, which is considerably less than that in the natural panel.

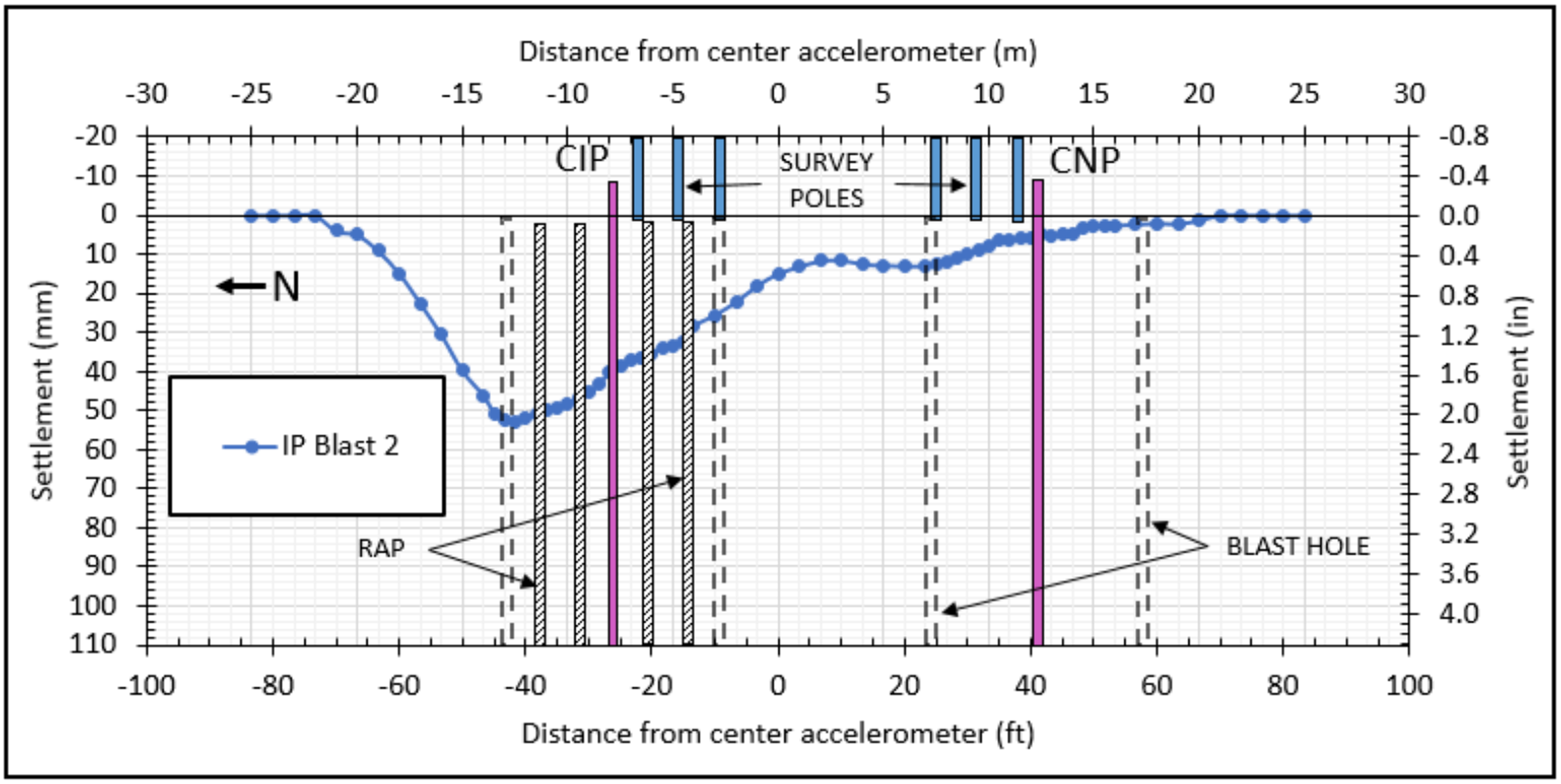

Figure 7.14: Ground surface settlement measurements obtained 30 minutes after blast 2 in the IP.

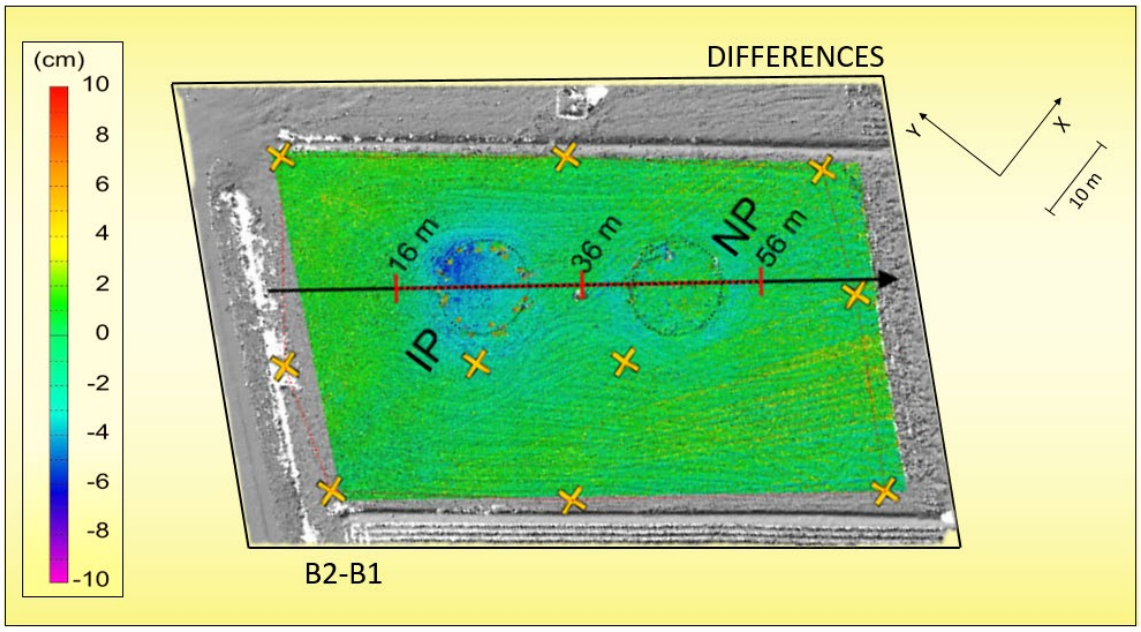

Figure 7.15: Color contour map from TLS surveys of settlement due to blast 2 in the IP (Modified after Amoroso et al., 2019).

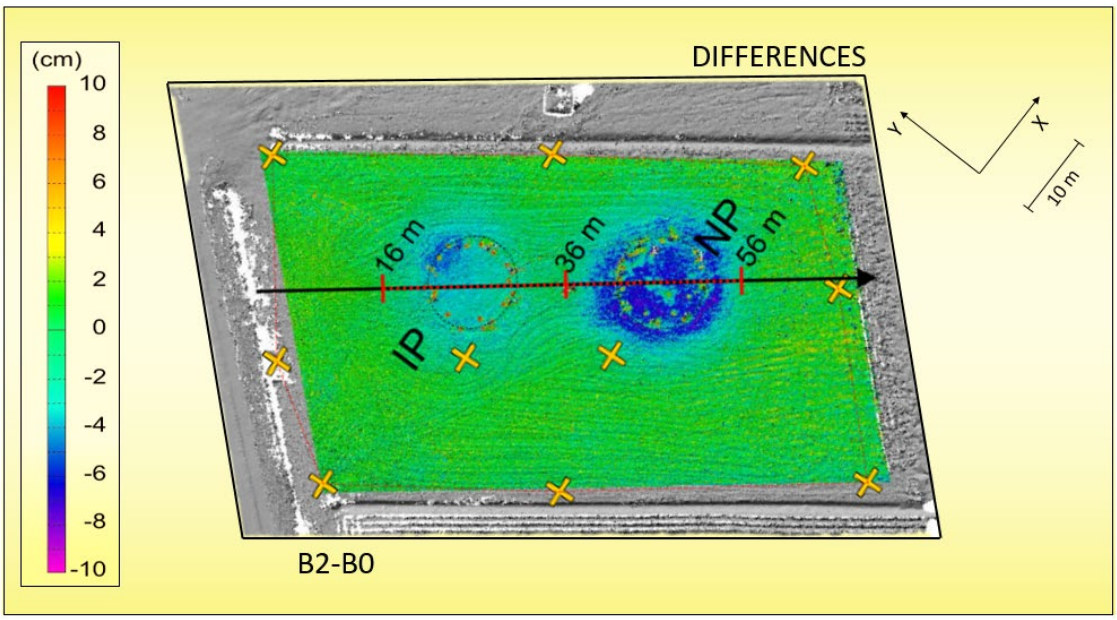

Figure 7.16: Color contour map of cumulative settlement from after the two blast tests from TLS surveys (After Amoroso et al., 2019).

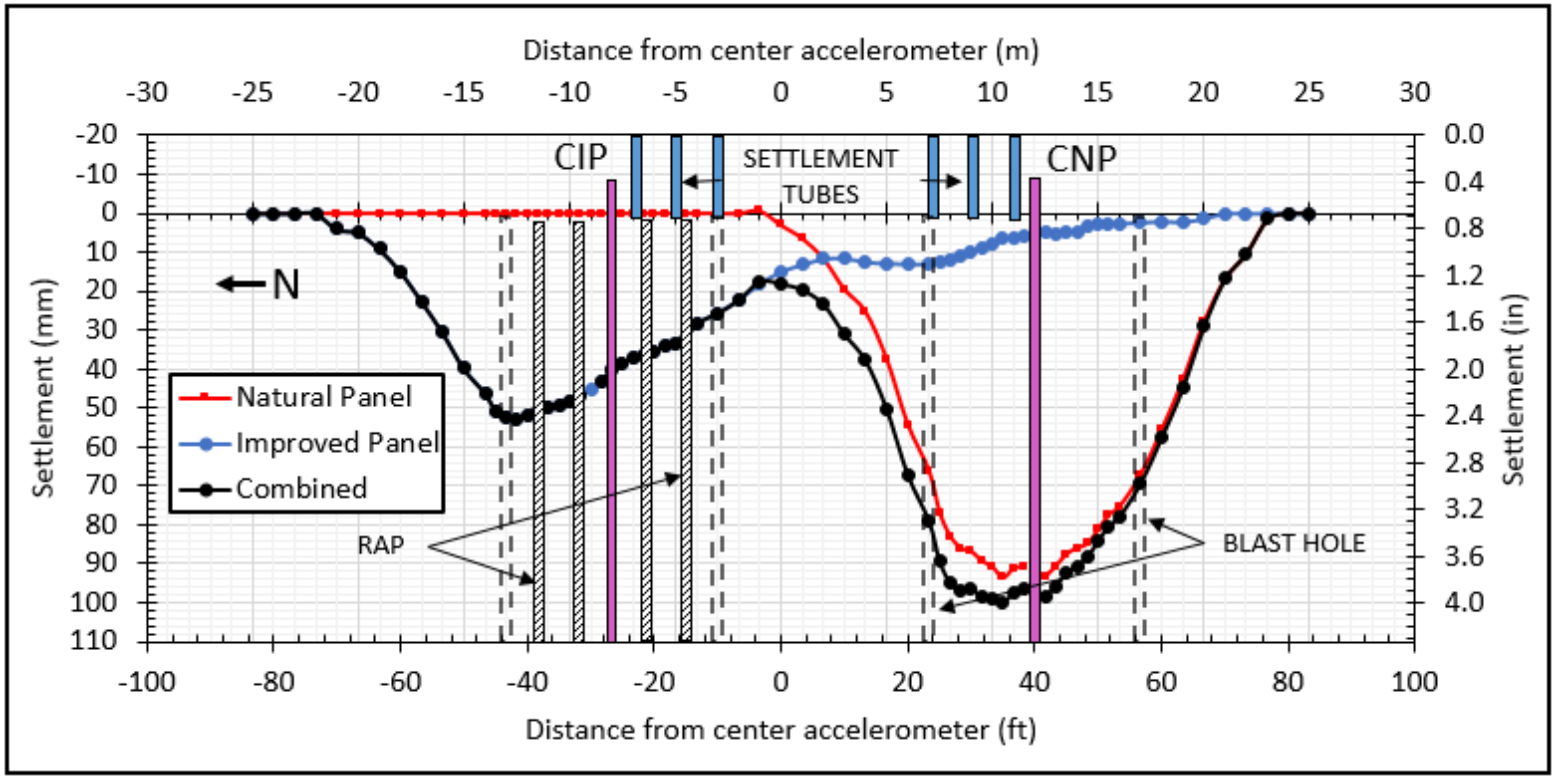

Figure 7.17: A comparison of ground settlement measurements obtained 30 minutes after blast 1 in the NP, and blast 2 in the IP across the test field. The combined settlement from blast 1 and 2 is also plotted.

7.3.3 Subsurface settlement

The settlement with depth recorded by our profilometer is shown in Figure 7.18. The maximum settlement of 10 cm is consistent with that measured with the survey stakes by the autolevel. The Sondex settlement also provided data consistent with expectations based on soil stratigraphy. The clay and organic soil within the top three meters did not compress, but settled along with the underlying sand. Liquefaction-induced settlement occurred within the layers of sandy silt and silty sand between 3 m and 11 m depth. Below 11 m, the Sondex measurements consistently showed that no settlement occurred indicating that pore pressure induced settlement was insignificant below 11 m. Average volumetric strain within the liquefied zone was approximately 1.6% from 3 to 8 m and approximately 0.7% from 8 to 11 m. These liquefaction-induced strains are consistent with what would be expected for a layer with the reported q_c values if liquefied by an earthquake (Tokimatsu and Seed, 1988, Tokimatsu and Yoshimine, 1983). Several inconsistencies exist in the settlement with depth profile as seen in Figure 7.18, such as the points where settlement appears to be less at shallow depth than at a deeper depth. These inconsistencies may be due to measurement error or local slippage of the corrugated pipe.

The Sondex measurements for the CIP and the CNP are plotted together in Figure 7.18. It appears that more irregularities due to extension or compression occurred in the IP than in the NP. Once again, the maximum settlement of 4 cm from the Sondex is consistent with the measurements from the survey stakes. The settlement profile shows a significant reduction in settlement in the zone of RAP treatment (3 m – 9.5 m) and a reduction of maximum surface settlement of approximately 6 cm. However, the measurements indicate that less than 2 cm of settlement occurred within the region of improvement in comparison to 8 cm in the natural panel. In contrast to the profilometer in the NP, the settlement in the IP did not decrease to zero at a depth of 11 m

although pore pressure induced settlement was likely insignificant below this depth as indicated by the natural panel settlement profile. Therefore, some additional mechanism may be responsible for the observed settlement of about one cm below this depth.

When we took the measurements after blast 2, the last metal ring that could be found was the one placed at 14.5 m depth. The settlement measurements with depth seem to indicate that a shift of ~1 occurred to the PVC access pipe for the Sondex tool.

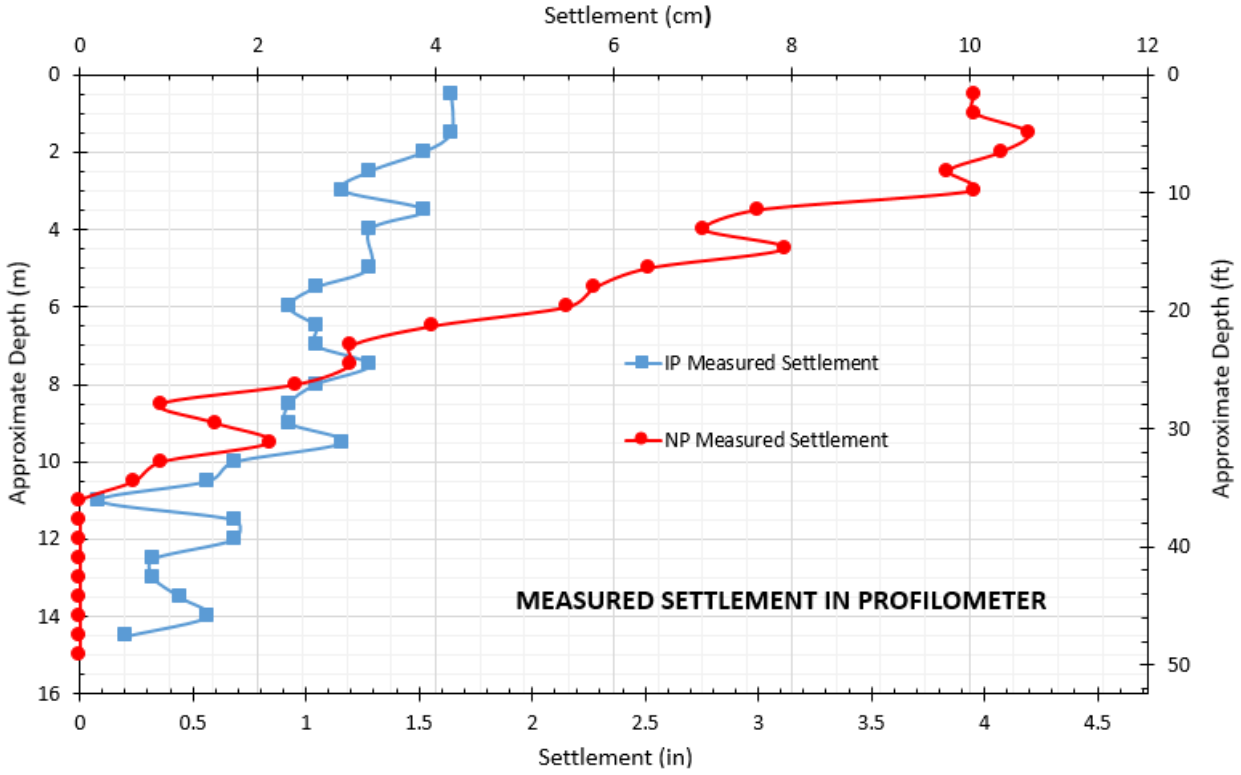

Figure 7.18: Comparison of observed settlement with depth in the NP and the IP as measured by the "Sondex" profilometer after blasts 1 and 2, respectively.

7.3.4 Comparison of measured settlements

We recorded settlement recorded at the surface of the CNP as 10.05 cm. The settlement at the CNP as reported by the ST was approximately 9.4 cm. Given the extensible nature of the

corrugated pipe used for the profilometer, the measurement error between the ST and the CNP is small (~6.5%).

The elevation change recorded between the TLS survey and the autolevel survey stakes show an approximate 30% difference in measured settlement, with the surface stakes reporting a more conservative measurement. Discrepancies in the TLS and survey stakes are likely due to the reference point of each measurement system. The survey stakes were embedded several inches into the ground prior to blast activities. Therefore, the stakes are recording settlement with respect to several inches beneath the initial ground surface. The TLS uses the initial ground surface as the reference point. In this context, the surface stakes may be considered a better indicator of subsurface activity since the data from the TLS is sensitive to surface elevation changes that may have occurred due to ejection of material from sand boils, etc., as shown in Figure 7.19. This seems to be the case when comparing the settlements in Figure 7.12 and Figure 7.18 at the location of the profilometer in the center of NP. The TLS reports a lesser value for settlement at the center of the panel than do the surface stakes. The ejected material from the sand boils would be reflected in the stakes as settlement, yet the TLS would record the build-up of the sand boils at the surface, depicting less settlement.

The three methods provided good validation for the actual observed settlement that we could use in the creation of a simplified settlement model. In order to perform settlement modeling analyses, we considered the effects of the two blast sequences separately and individually. We used the settlement that occurred during blast 1 to represent the total settlement in the NP, and the incremental settlement that occurred during blast 2 represents the total settlement in the IP. This nomenclature will be used through the remainder of this thesis as an analysis of settlement is later discussed.

Figure 7.19: Multiple sand boils and ejecta, evidence of liquefaction, observed during blast 1 near the center of the unimproved natural panel (NP).

The TLS and surface stake surveys confirm that the settlement in the IP was about 40% of the settlement in the NP. Figure 7.20 superimposes the pore pressure induced settlement uniquely caused by blast 1 and blast 2, respectively. This figure highlights the asymmetric settlement profile in the IP and its contrast with the settlement profile in the control NP.

The asymmetric settlement profile was likely due to variations in the thickness of the liquefiable layer on the North side. The second potential factor for the higher settlement is inconsistencies in construction during RAP installation. The crowd test results provided in Table 5.1 demonstrate that the RAPs on the north side of the IP settled more during crowd tests and were not constructed to the same depth as the other RAPs in the grid. This may have accounted for the additional ~5 mm of settlement on the north side of the IP. The observed settlements from the TLS survey in Figure 7.16 are better understood when the crowd test results from Table 5.1 are taken into consideration.

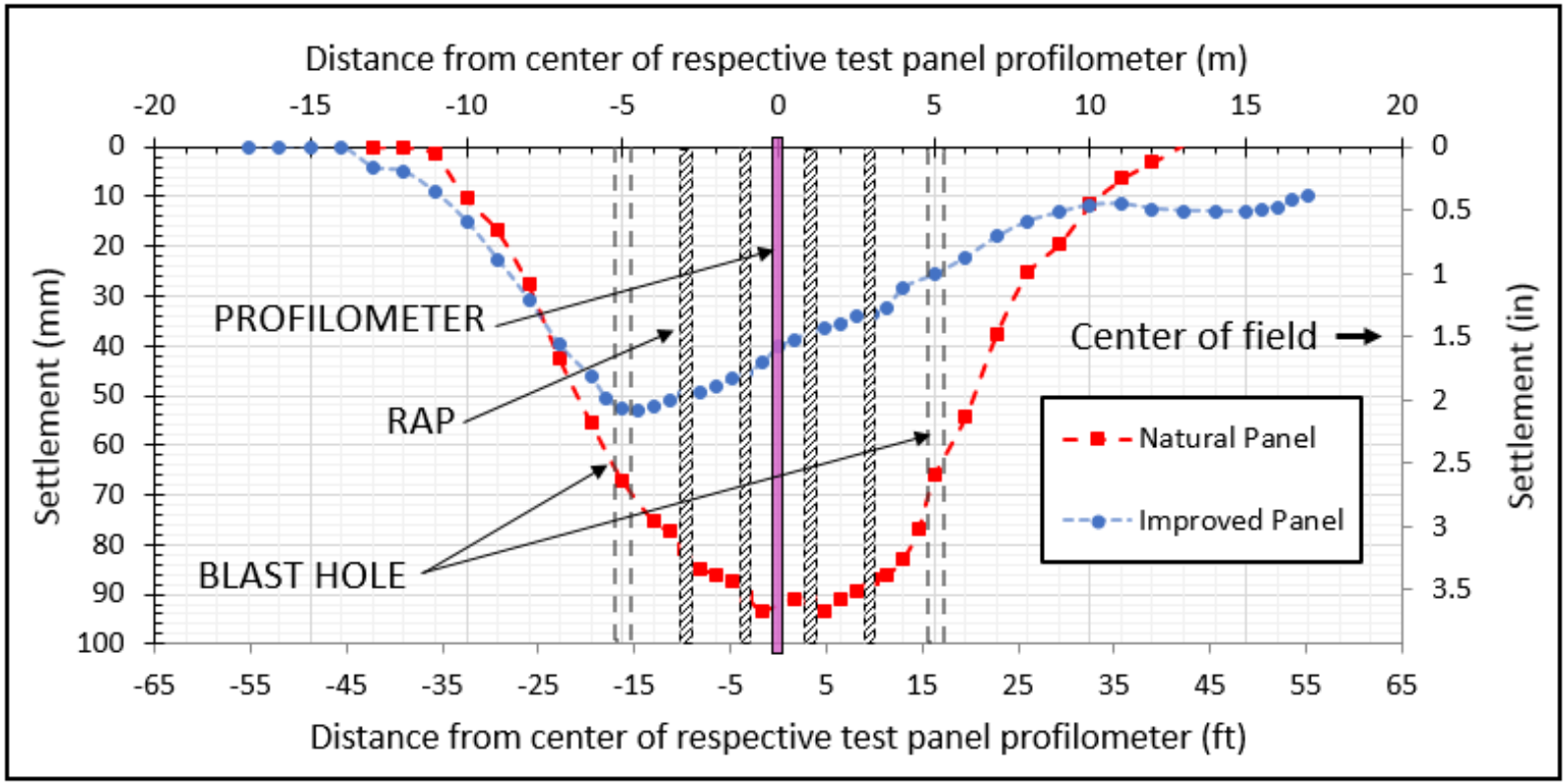

Figure 7.20: A superimposed comparison of the settlements between blast 1 in the NP and blast 2 in the IP.

7.4 Accelerometer results

INGV placed four triaxial accelerometers in between the NP and the IP. Each accelerometer was programmed to record motion in the time domain in the X, Y, and Z directions. Figure 7.21 shows the relative placement of the accelerometers to the X-Y coordinate plane along with the detonation shot sequence in each panel. ACC1 and ACC3 were placed at 4.5 m depth, while ACC2 and ACC4 were placed at 3.5 m depth. The detonations are characterized by a very impulsive signal of short duration (about 0.02 s) and high amplitude followed by a coda having a lower amplitude and a frequency content below 25 Hz. For each detonation the entire recorded signal does not exceed 0.4 s (Amoroso et al., 2019). The signal pulses from the deeper (6.5 m), and heavier (2 kg) charges produced very energetic signals that are clearly recognizable in both the time and the frequency domains. By contrast, the signals at 3.5 m depth (0.5 kg) have lower amplitude and are difficult to detect in the recorded time-series (Amoroso et al., 2019).

An example of the accelerometer time-history recorded by INGV in the X, Y, and Z directions is provided in Figure 7.22. This record is consistent with the accelerogram records from the three other accelerometers. The accelerogram records show that 12 of the 16 detonation pulses are easily identifiable by the transient spikes. The maximum peak acceleration recorded by the in-hole sensors was about 45g and 52g during blast #1 (NP) and blast #2 (IP), respectively (Amoroso et al., 2019). In either case, the largest acceleration was recorded by ACC2 in the Y-direction.

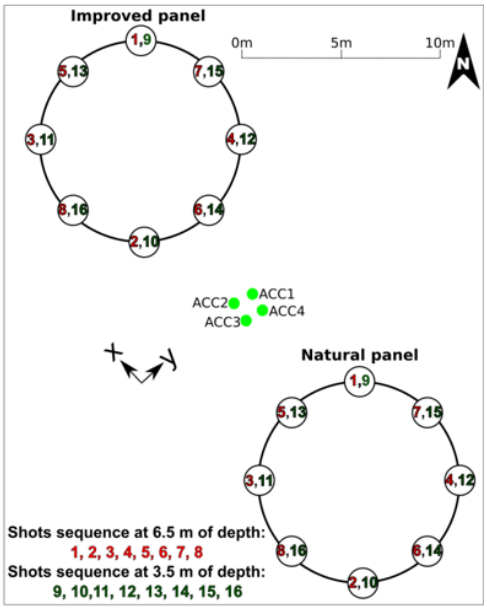

Figure 7.21: Relative placement of the four triaxial accelerometers with respect to the NP and the IP. The detonation shot sequence is also shown (after Amoroso et al., 2019).

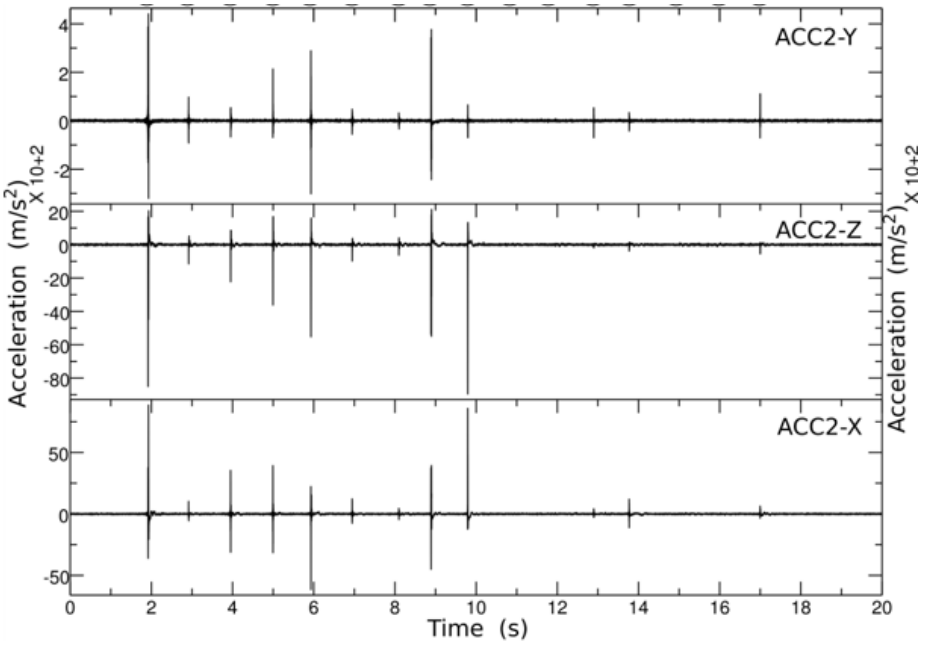

Figure 7.22: An example accelerogram from ACC2 during blast #1 (see Error! Reference source not found.**) recorded in the time domain in the X, Y, and Z directions (after Amoroso et al., 2019).**

We received the raw acceleration time history records from INGV for our own computations. A typical set of acceleration time history records in the x, y and z direction for one blast detonation is shown in Figure 7.23. All accelerometers remained in good working condition throughout the duration of each blast sequence. The accelerometers were able to record data to one thousandth of a m/s^2, however, approximately 1 m/s^2 of noise existed within the recorded data. The extraneous frequencies were filtered out using a Fourier transform algorithm within a MatLab program written by Jared Baxter, a colleague of mine from the Electrical Engineering department at BYU.

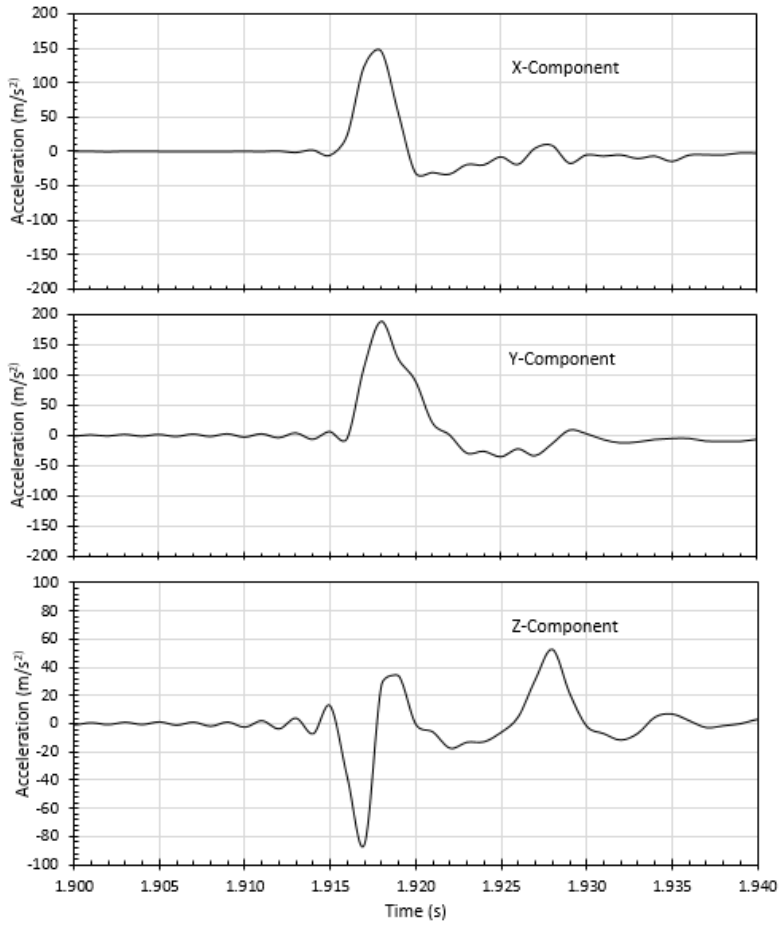

Figure 7.23: Time history of accelerations in the x, y and z directions from ACC2 during the first 2.0 kg detonation of blast #1.

8 ANALYSIS OF RESULTS

8.1 Settlement analysis

8.1.1 Initial observations and predicted settlements based on CPT resistance

In order to perform settlement modeling analyses, we considered the effects of the two blast sequences separately and individually. The settlement that occurred during blast 1 was used to represent the total settlement in the NP, and the incremental settlement that occurred during blast 2 represents the total settlement in the IP.

The observed settlement profile in the natural panel indicates that liquefaction-induced settlement occurred between 3 m and 11 m depth, as evidenced by Figure 7.18. Little to no settlement occurred within the 3-m thick cohesive surface layer and no settlement occurred below 11 m in the natural panel. Within the liquefied layers from 3 to 11 m, the CPT-based settlement approach proposed by Zhang et al. (2002) was used to compute liquefaction-induced settlement relative to measured settlement in both the natural panel and the improved panel prior to the installation of the RAP columns. We performed these calculations to: (1) confirm that liquefaction induced settlement would be similar for both sites prior to improvement and (2) to evaluate the ability of the method to match the measured settlement versus depth profile.

The Zhang et al. (2002) approach requires an estimate of the factor of safety against liquefaction. Although liquefaction was produced by blasting, indicating a factor of safety against

liquefaction less than 1.0, the exact blast-induced factor of safety is not known because the method does not produce a cyclic stress ratio (CSR). However, an approximation for the factor of safety may be gained by comparing computed and observed settlement values. We computed settlement vs. depth plots for the CPTu data at the NP area using the established volumetric strain equations assuming liquefaction safety factors of 1.0 and 0.9. The volumetric strain equations for FS are empirically derived as explained in section 2.6 and are dependent on the clean sand equivalent of the corrected cone tip resistance. The volumetric strain equations for FS_L=1.0 and FS_L=0.9 are given in equations 8.1.1, 8.1.2, and 8.1.3, respectively.

$$if\ FS = 1.0, \varepsilon_v = 64(q_{c1N})_{cs}{}^{-.93}, for\ 33 \leq (q_{c1N})_{cs} \leq 200 \quad (8.1.1)$$

$$if\ FS = 0.9, \varepsilon_v = 102(q_{c1N})_{cs}{}^{-.82}, for\ 33 \leq (q_{c1N})_{cs} \leq 60 \quad (8.1.2)$$

$$if\ FS = 0.9, \varepsilon_v = 1430(q_{c1N})_{cs}{}^{-1.48}, for\ 60 \leq (q_{c1N})_{cs} \leq 200 \quad (8.1.3)$$

Using these equations, we computed volumetric strains and associated ground settlements for each layer in the soil profile from 11 m to 3.5 m. The soil profile and normalized cone tip resistance ($q_{c1N,cs}$) profile are shown in Figure 8.2 (a) and (b), respectively. Figure 8.2 (c) shows the computed settlement vs. depth profile relative to the measured settlement profile. As shown in Figure 8.2 (c), the computed settlement vs. depth curves for FS_L equal to 1.0 and 0.9 bound the observed values. This result suggests that the true factor of safety is between these two limits, on average. By interpolating between the volumetric strain equations for FS_L of 0.9 and 1.0, we obtained excellent agreement between the measured and computed settlement vs. depth curves using a FS_L of 0.93, as shown in Figure 8.2 (c). Also shown in Figure 8.2 (d) are the computed settlement vs. depth curves for the NP and IP pre-improvement using the same FS of 0.93. These estimates are within 6% of each other because there are only minor variations (1-2%) in the

respective $q_{c1N,cs}$ profiles. The volumetric strain equation used for the interpolated FS_L=0.93 was as follows:

$$\varepsilon_v = 102(q_{c1N})_{cs}{}^{-.82}, for\ 33 \leq (q_{c1N})_{cs} \leq 60 \quad (8.1.4)$$

$$\varepsilon_v = 1430(q_{c1N})_{cs}{}^{-1.51}, for\ 60 \leq (q_{c1N})_{cs} \leq 200 \quad (8.1.5)$$

We also computed the liquefaction-induced settlement following RAP installation using the Zhang et al. (2002) procedure but with the post-installation $(q_{c1N})_{cs}$ CPTu profile. Because the average peak residual r_u following the blast in the IP was approximately 0.8, the factor of safety was apparently greater than 1.0. We estimated the factor of safety against liquefaction in this case to be 1.05 based on the relationship between excess pore pressure ratio and factor of safety against liquefaction in sand developed by Tokimatsu and Yoshimi (1983) as shown by Figure 8.1. The higher factor of safety of the IP in comparison with the NP (FS_L = 0.93) can be attributed to both increased density and increased lateral earth pressure of the stabilized soil. The liquefaction-induced volumetric strain for FS = 1.05 was then interpolated from the curves for FS of 1.0 and 1.1 provided by Zhang et al. (2002). The equations for FS_L=1.1 and FS_L=1.05 are provided as equations 8.1.6 and 8.1.7.

$$if\ FS = 1.1, \varepsilon_v = 11(q_{c1N})_{cs}{}^{-.65}, for\ 33 \leq (q_{c1N})_{cs} \leq 200 \quad (8.1.6)$$

$$if\ FS = 1.05, \varepsilon_v = 37.5(q_{c1N})_{cs}{}^{-.88}, for\ 33 \leq (q_{c1N})_{cs} \leq 200 \quad (8.1.7)$$

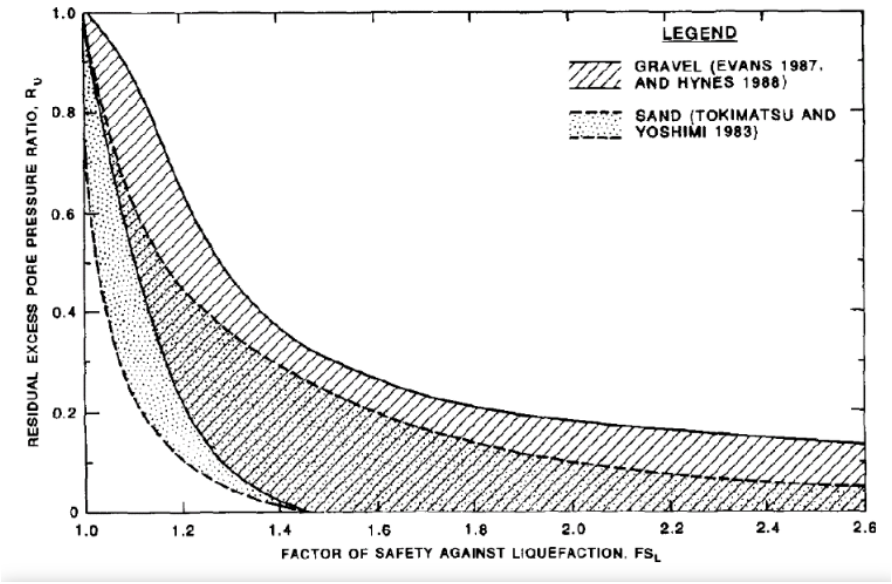

Figure 8.1: Typical factors of safety against liquefaction versus residual excess pore pressure ratio (After Marcusson and Hynes, 1990).

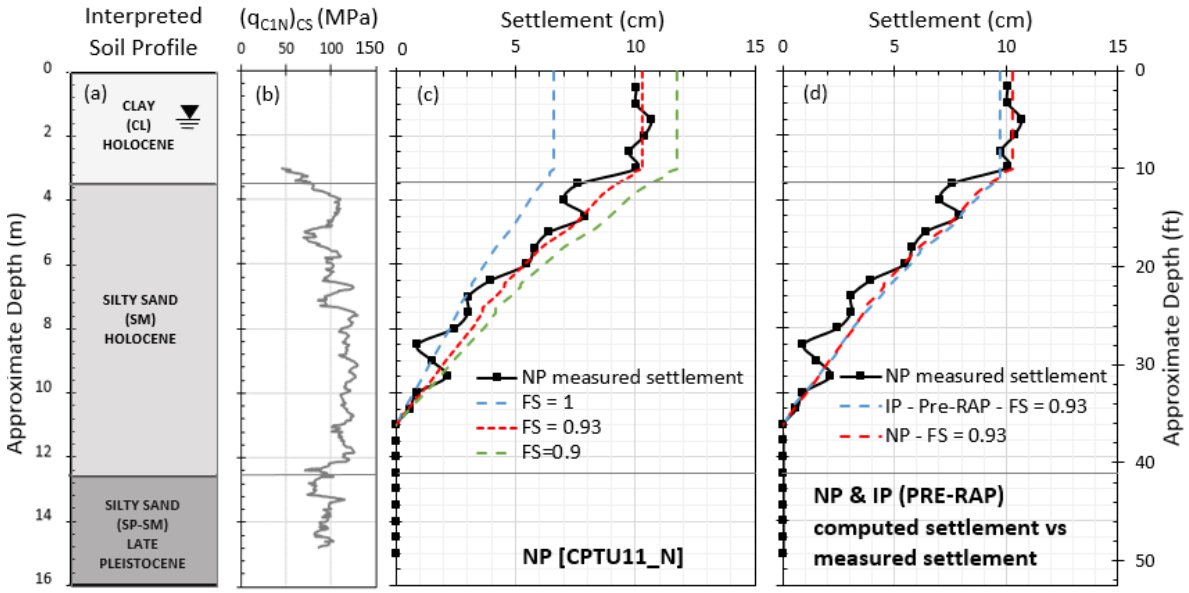

Figure 8.2: (a) Simplified interpreted soil profile, (b) normalized CPT tip resistance with applied clean sand correction (c) Comparison of measured settlement vs. depth curve in unimproved panel with computed settlement vs. depth curves for FS = 1.0, 0.93 and 0.9 using the Zhang et al. (2002) CPT-based approach (d) Measured vs. computed settlement for NP and IP (Pre-RAP).

We again used the Zhang et al. (2002) method to compute the volumetric strain for the RAP-reinforced zone of the improved panel for a factor of safety of 1.05 (3 to 9.5 m.) and a factor of safety of 0.93 applied beneath the RAP-reinforced zone (9.5-11 m) where the settlement vs. depth curve from the profilometer shows a slope parallel to that observed within the liquefiable layer in the NP (see Figure 7.18). The computed curve significantly underestimates the observed settlement from 9.5 to 15 m, but overestimates settlement within the zone treated with the RAP columns.

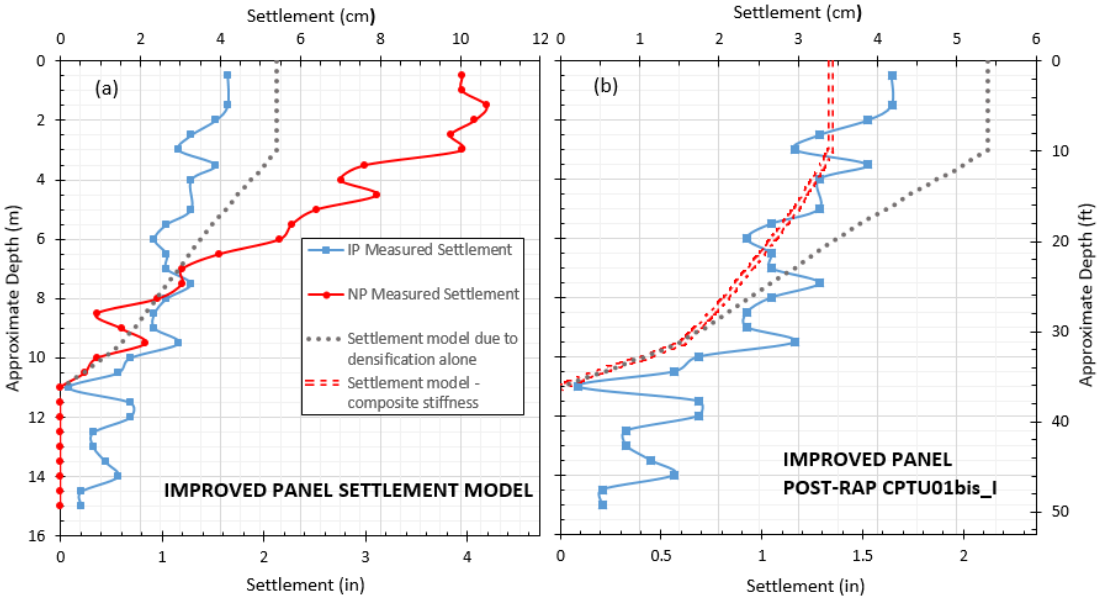

Figure 8.3: (a) Measured settlement in the NP and the IP compared with computed settlement using the Zhang et al. (2002) approach considering RAP densification only and (b) Comparison of measured settlement in the IP with the settlement model considering composite stiffness.

8.1.2 Settlement profile using a composite stiffness approach

To consider the stiffening effect that the RAP columns may have had on the treated soil from 3 to 9.5 m, we assumed the native soil and RAP columns to act as a composite as suggested

by Smith and Wissman (2018). In this approach, the elastic modulus of the RAP (E_{pier}) is multiplied by its replacement ratio (R_a) in a unit cell, while the elastic modulus of the natural soil after the generation of excess pore pressure ($E_{natural}$), is multiplied by (1-R_a) to compute a composite elastic modulus ($E_{composite}$) as given by the equation,

$$E_{composite} = E_{natual}(1 - R_a) + E_{pier}(R_a) \quad (8.1.2.1)$$

Elastic theory can then be used to compute the settlement, S, of this layer using the equation,

$$S = \frac{\Delta\sigma' H}{E_{composite}} \quad (8.1.2.2)$$

where Δσ is the change in effective stress (r_u*σ') as the excess pore pressure dissipates to zero and H is the thickness of the composite layer with RAP columns. Incrementally, the equation can be written as a summation where $\Delta\sigma'_i$, H_i, $(r_u)_i$ and $(E_{composite})_i$ are values at each depth interval

$$S = \sum \frac{(r_u)_i \, \sigma'_i H_i}{(E_{composite})_i} \quad (8.1.2.3)$$

The elastic modulus for each increment of the native soil after pore pressure generation could then be estimated using the equation

$$(E_{natural})_i = \frac{(r_u)_i \sigma'_i H_i}{S_i} \quad (8.1.2.4)$$

where S_i is the incremental settlement of the natural soil after RAP installation using the Zhang et al. (2002). For this case, H_i was the measurement interval of the CPT or 20 mm, the replacement ratio, R_a, for the RAPs was 5%, E_{pier} was 200 MPa (4000 ksf) based on a full-scale field test data base (Wissman et al., 2001), and S_i' is the predicted settlement using Zhang et al. (2002) with a FS=1.05 as reported previously.

Using this procedure, the elastic modulus of each pier greatly stiffens the soil at shallow depths and the composite modulus of elasticity increases with depth as the soil experiences greater confining stresses. Throughout the depth of improvement, the piers were, on average, responsible for 53% of the composite elastic modulus. With an area replacement ratio of only 5%, the piers improved the estimated stiffness by a factor of 2.1. This model assumes that the liquefiable layer between 9.5 m and 11 m remains unchanged.

A plot of computed settlement versus depth using this procedure is provided in Figure 8.3 (b), relative to the measured curve. The effect of composite stiffness is evident in the steeper slope of the settlement vs. depth curve within the zone treated with RAPs, which also provides a better fit to the shape of the measured settlement curve in this depth range. Approximately 2 cm less settlement occurs within the liquefiable layer from 3 m to 9.5 m by considering composite action rather than densification only as shown in Figure 8.3 (b).

8.1.3 Settlement analysis beneath the RAP improved zone

The settlement vs. depth profile for the IP, observed in Figure 7.18, is difficult to interpret beyond a depth of 11 m. The measurements which we obtained between a depth of 9 and 11 m, as shown in Figure 7.18, show that the settlement behavior within this zone was consistent between the IP and the NP. The consistent composition of the profile within this region, as well as the consistent settlement behavior lead us to believe that the amount of settlement between discrete readings should also be consistent. In the NP between 10.5 and 11 m depth approximately 0.6 cm of settlement occurred. Within this same zone in the IP approximately double the settlement, or 1.2 cm, occurred. We believe that the discrepancy can be accounted for by local slippage of the

corrugated pipe, or measurement error, as explained previously. As such, we estimate that settlement at a depth of 11 m in the IP should be more appropriately between 0.8 and 1.0 cm.

To compute the settlement at the base of the pier, we assume that the composite stiffness of the sand-RAP system transfers some load to the base of the RAP group. Mobilized settlements that occur external to the reinforced block can generate downward shear forces along the interface between the RAP reinforced volume and the surrounding liquefied sand. We estimated the downward shear force using empirical correlations for the residual shear strength of liquefied sands provided by Olson and Stark (2002), and verified using those proposed by Idriss and Boulanger (2007) and was computed as ~13% of the initial vertical effective stress. We applied the residual shear strength of the silty sand around the perimeter of the RAP group, and within the zone of RAP improvement (3-9.5 m). The estimated undrained shear strength of the soft clay layer (0-3 m) was also included in this load estimation from CPTu as proposed by Mayne (2016). We assumed this load to be resisted primarily by the 16 RAP columns.

We then computed the end-bearing settlement that was induced by this load using elastic methods, as explained by Vesic (1977), considering the settlement caused by the load carried at the toe of a single pier in sand:

$$Se = \frac{\pi}{4}(1 - v^2)\frac{q_{max}B}{E_s} \tag{8.1.3.1}$$

where q_{max} is the pressure exerted by the residual shear strength at the base of the RAP, v is Poisson's ratio of the soil, assumed to be 0.2 for sand, B is the footing width (0.5 m), and E_s is the average modulus of elasticity of the sandy soil between 11 m and 12 m.

Using this equation, we computed the elastic settlement for a single pier to be 0.74 cm. We assumed the computed settlements to take place within two diameters of an individual pier or 1 m, in this case. This settlement is comparable to the expected settlement of 1 cm at 11 m.

8.1.4 Summary of computed settlement model

We summarize the computed settlements in the improved panel for the various approaches incrementally in Figure. 8.4 (a) and as a function of depth relative to the measured curve in Figure. 8.4 (b). No settlement occurred within the top layer of clay and organic material as expected. The liquefiable zone between 3 m and 11 m depth is divided into two portions, the improved zone (3 m to 9.5 m) and the non-improved zone (9.5 m to 11 m). Settlement below 11 m is also shown.

Within the improved zone (3 m to 9.5 m), we compare three distinct settlement models. The largest of the three represents the predicted settlement within this layer if the RAP columns had not been installed which amounts to approximately 8.2 cm. If only the effects of densification from RAP installation are considered, settlement in this interval decreases to 3.9 cm. Including the effects of densification and composite behavior together yields a settlement of 1.86 cm which is very close to the measured settlement range of about 2 cm in this interval. Therefore, composite action in the RAP treated zone significantly reduced settlement despite the high r_u values.

In the liquefied zone beneath the RAP columns, we predict 1.5 cm of settlement using the Zhang et al. (2002) method with FS = 0.93, which is in reasonable agreement with the observed settlement in both the natural panel and improved panel.

At a depth of 11 m, where liquefaction did not cause settlement in the natural panel, we observed about 1 cm of settlement in the improved panel. This settlement appears to result from the RAPs transferring the cumulative residual shear strength of the soil in the treated zone from 0

to 9.5 m down to the base of the RAP group and inducing a computed settlement of 0.74 cm based on elastic methods to a depth of 2 pier diameters below the base of the footing at a depth of 12 m. Using this approach produces good agreement with the measured settlement of 1 cm in this interval.

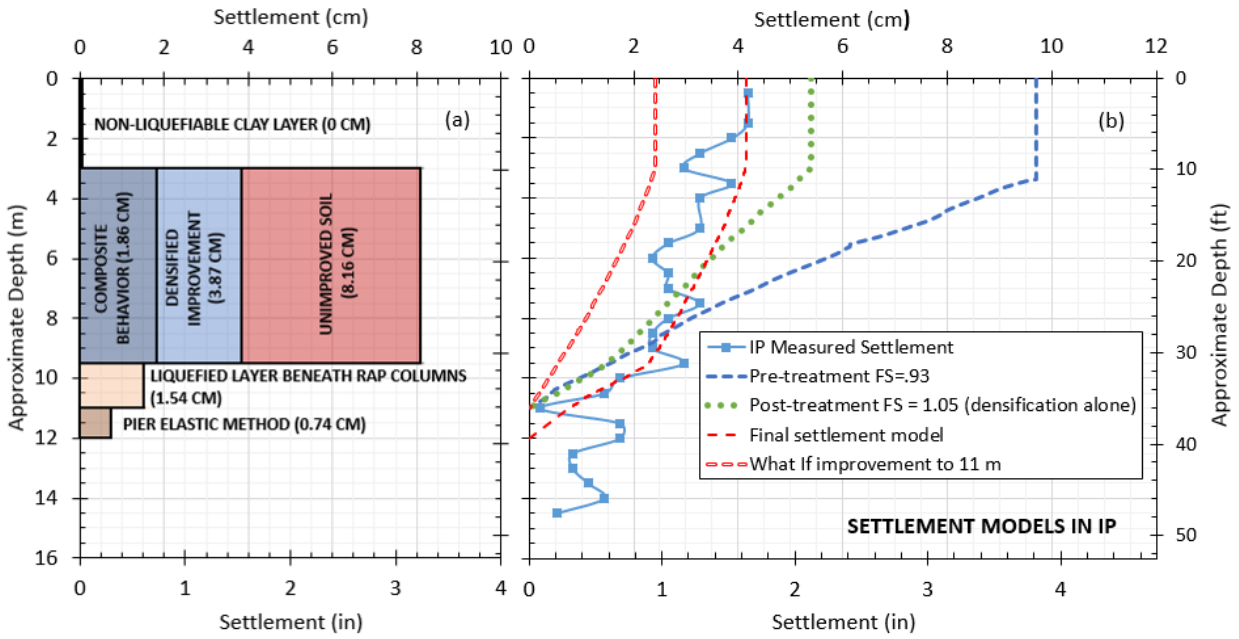

Figure. 8.4: (a) Comparison of computed settlement in various depth intervals within the IP. (b) Comparison of measured settlement vs. depth in the IP with settlement predicted using the interpolated Zhang et al. (2002) approach, densification alone, and composite stiffness model.

8.1.5 Settlement profile assuming RAP treatment through liquefiable layer

One important question resulting from this experiment is the impact of extending the RAP columns to deeper depths. In this case study, the blasting technique induced liquefaction to a depth of 11 m, yet the improvements were only installed to 9.5 m depth. How would the surface settlement and settlement vs. depth profile appear if the RAPs extended through the bottom of the liquefiable layer? In this case, densification and composite action would be expected to

significantly reduce settlement in the depth interval from 9.5 m to 11 m. Figure. 8.4 (b) also presents the predicted settlement vs. depth curve if RAP improvement was continued to 11 m in depth. Improving the liquefiable layer between 9.5 and 11 m, and extending the settlement slope of the improved zone, an additional 1.7 cm of settlement could potentially be eliminated. Therefore, the ground surface settlement would be reduced from 9.7 cm without treatment to 2.4 cm with RAPs extending through the liquefied zone. This represents a reduction in settlement of 75%.

8.2 Equivalent earthquake

As described in chapter 4, the blast liquefaction test was designed with the intent to produce a zone of liquefaction similar to that would be expect for a M_w 6.14 earthquake and PGA = 0.22g. Under these design circumstances we computed the FS_L with depth and is shown in Figure 4.6 (b). Liquefaction was considered possible between 3 and 8 m depth, and was *expected* between 6 and 9 m depth. The PPT data recorded during both blast 1 and blast 2 demonstrate that incipient liquefaction likely occurred throughout the entirety of the profile between 4 and 9 m depth. Our estimated FS_L in the NP was approximately 0.93, according to the excess pore pressure ratio relationship proposed by Tokimatsu and Yoshimine (1983). Using CLiq software and this FS_L we computed the combinations of earthquake magnitude and peak ground acceleration which could have produced an equivalent observed FS_L during the experiment. This plot of equivalent FS_L is provided in Figure 8.5. In order to perform parametric comparative analyses, we chose a Mw, PGA pair of 7.5, 0.15, respectively.

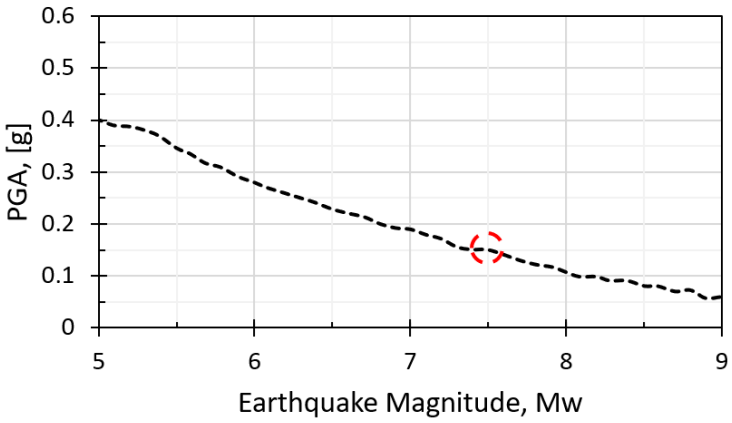

Figure 8.5: Combinations of earthquake magnitude, M_w, and peak ground acceleration, PGA, that would produce equivalent FS_L observed during blast-testing.

8.3 Additional analysis of RAP improvement on liquefaction mitigation

The predictive settlement equations from Zhang et al. (2002) provide a convenient way to quantitatively measure the effects of RAP improvement in the IP. When compared with the excess pore pressure ratio relationship proposed by Tokimatsu and Yoshimine (1983), the average observed r_u values are indicative of a FS_L = 1.05. This varies substantially, however, from the predictive FS_L when using CLiq software. When subjected to a Mw = 7.5 and amax = 0.15 we predict the post-improvement FS_L to be much higher throughout the zone of improvement, as shown in Figure 8.6. It is possible that the average r_u of 78%, and correspondingly a FS_L=1.05 underestimate the performance in the IP. The FS_L profile in Figure 8.6 shows that weak layers of soil were present near the discrete depths of 4, 5, 6, 7, 8 and 9 m where the PPT were placed. Had we placed the PPT within different layers it is possible that the average recorded r_u, and corresponding FS_L, could likely be different.

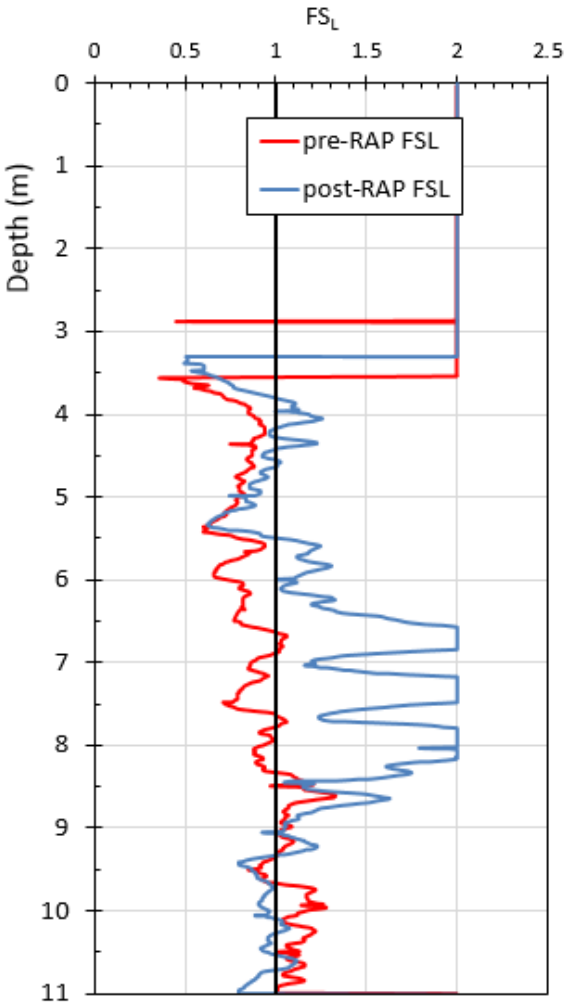

Figure 8.6: Predicted FS_L in the pre-RAP and post-RAP improved soil assuming a Mw = 7.5 and amax = 0.15.

Another commonly used indicator of liquefaction potential was shown in Figure 8.7 and shows the CRR plotted against corrected cone tip resistance, q_{c1}. Based on numerous historical records Idriss and Boulanger (2008) fit a polynomial which separates expected liquefaction from non-liquefaction. The polynomial function is expressed as,

$$CRR_{M=7.5,\sigma'_v=1atm} = \exp\left(\frac{q_{c1,Ncs}}{113} + \left(\frac{q_{c1,Ncs}}{1000}\right)^2 - \left(\frac{q_{c1,Ncs}}{140}\right)^3 + \left(\frac{q_{c1,Ncs}}{137}\right)^4 - 2.8\right) \quad (8.3.1)$$

We plotted the $q_{c1N,cs}$ and CSR pairs against this polynomial in Figure 8.7. According to Idriss and Boulanger (2008), it appears that RAP installation improved the profile at all depths, with the greatest improvement from RAP occurring in the 6-8 m region for the assumed ground motion, as seen in Figure 8.7 (c).

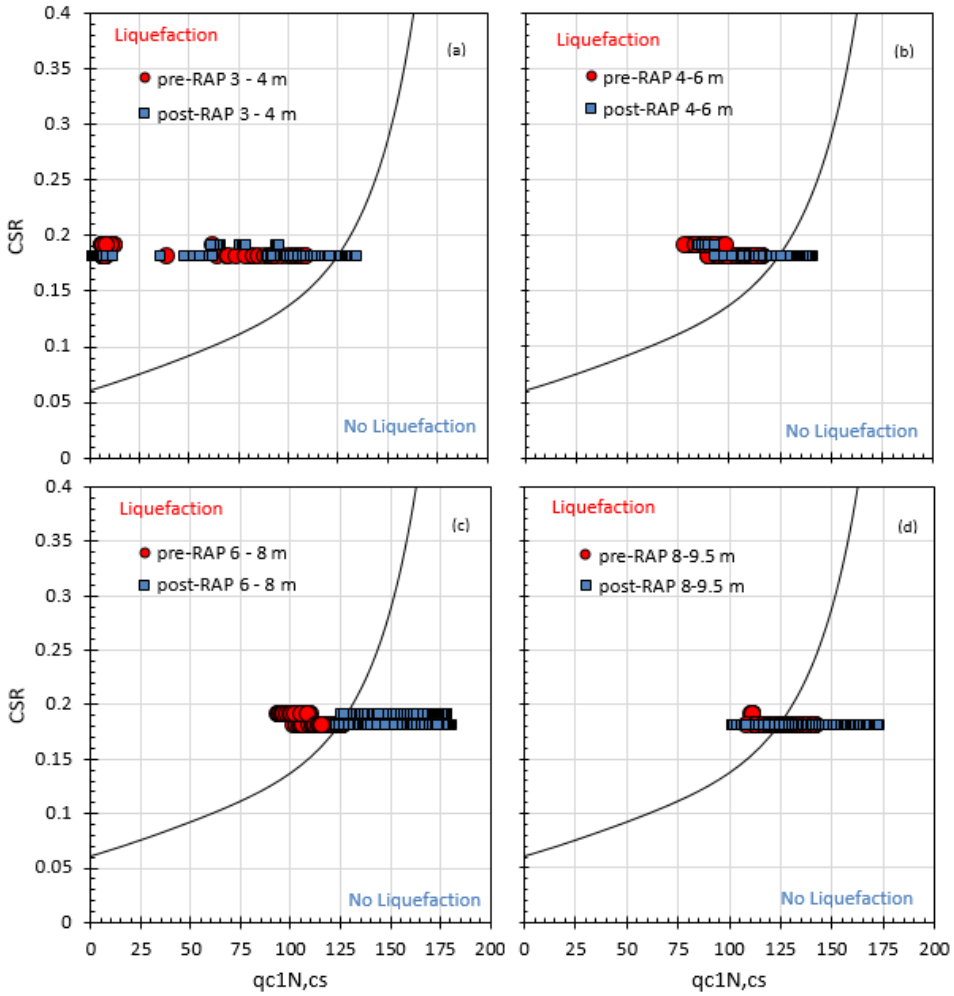

Figure 8.7: Pairs of $q_{c1N,cs}$ and CSR for depths of (a) 3-4 m, (b) 4-6 m, (c) 6-8 m and (d) 8-9.5 m pre- and post-RAP improvement.

Neither the Idriss and Boulanger (2008), nor the Zhang et al. (2002) procedures consider the effects of K_0 on liquefaction triggering. Nevertheless, by applying the K_0 multiplier from equation 3.5.1 we see that the predicted CRR and FS_L are improved substantially by the increased lateral earth pressures, as shown in Figure 8.8 (a) and (b), respectively.

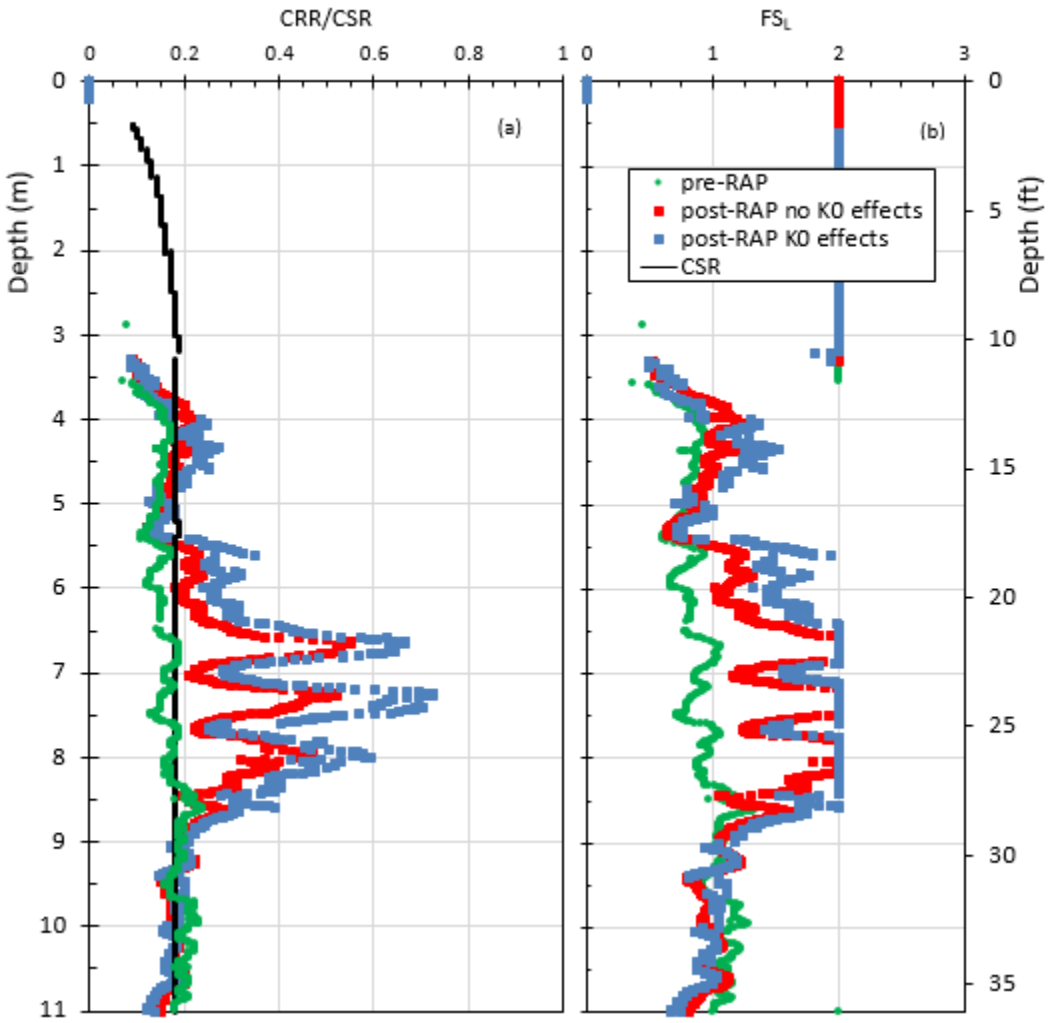

Figure 8.8: (a) CRR and CSR, and (b) FS_L plotted for pre-RAP, post-RAP without K_0 effects, and post-RAP with K_0 effects considered.

Presently no conclusive data exists that correlates the effects of K_0 with decreased liquefaction induced settlement. This makes quantifying the effects K_0 a more difficult task than using the composite stiffness method described in section 8.2.2. However, when considering the FS_L profile of Figure 8.8 (b), in conjunction with the average measured r_u of 78%, the effects of increased K_0 may explain the reduction in r_u, and associated settlements where previous CPT-based FS_L relationships cannot. Between the depths of 3.5 and 5.5 m, Figure 8.8 (b) shows that the

post-RAP improved FS_L is less than 1, indicating that liquefaction should occur and r_u values should be in excess of one. By contrast, the post-RAP FS_L considering K_0 effects from Figure 8.8 (b) plots above one, which is more consistent with the average observed r_u during blasting in the IP. This data points to the effectiveness of increasing lateral earth pressures to mitigate liquefaction. Further research will undoubtedly lead to the ability to quantifiably incorporate these effects into predictive techniques for liquefaction-induced settlement.

8.4 Measured accelerations and computed shear strain

We used the recorded accelerometer data to estimate the shear strains occurring within the ground at the center of the two panels as a result of the energy from each detonation. The placement of multiple accelerometers at the center of the two panels made it possible to compute the strain caused in the direction of each blast wave independently. The constitutive relationship between shear, radial, and tangential strain, provided in equation 8.4.1 is the basis of this computation.

$$\Upsilon = \varepsilon_r - \varepsilon_\theta \tag{8.4.1}$$

Where Υ is shear strain, ε_r is radial strain, and ε_θ is tangential strain. The radial and tangential strain are determined by the following relationships

$$\varepsilon_r = \frac{u_{r1} - u_{r2}}{dR} \tag{8.4.2}$$

$$\varepsilon_\theta = \frac{u_{r1} + u_{r2}}{R_1 + R_2} \tag{8.4.3}$$

where u_{r1} and u_{r2} are radial displacements obtained by the double integrated accelerations recorded by two accelerometers in the direction of the blast charge, dR is the distance between the two

accelerometers in the direction of the blast, and R_1 and R_2 are the distances of each accelerometer from the blast source. Figure 8.9 below helps to illustrate these variables.

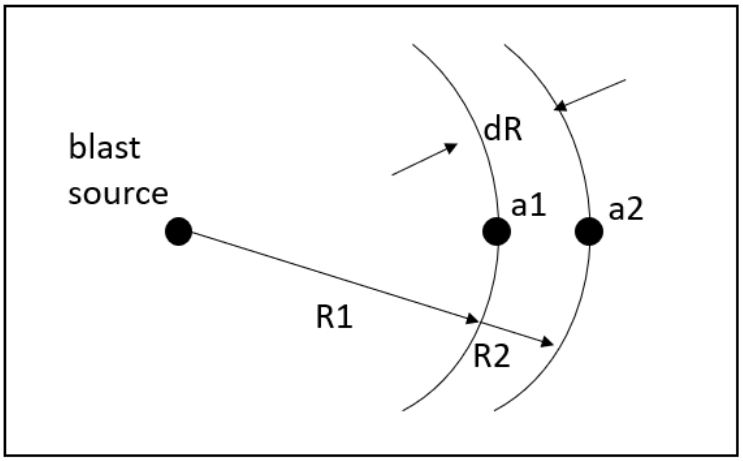

Figure 8.9: A simplified diagram showing the necessary variables to compute shear strain.

We measured the distance from each blast source to each accelerometer as reliably as possible using Google Earth, and established unit vectors in the direction of each detonation. We then double integrated the acceleration records in the direction of each blast between each of the accelerometers to obtain displacement records for each accelerometer. We then used Equation 8.4.1 to compute shear strain with the displacement records substituted into 8.4.2 and 8.4.3. To eliminate the effects of noise in the accelerometer record, only the displacements within the 0.4 s duration of each recorded signal were considered. At the end of each signal duration the displacements were re-zeroed. The incremental cyclic shear strain (CSS) was between 0.5% and 2.5% per cycle.

The incremental computed shear strains from 13 of the 16 blast charges are plotted relative to the average incremental r_u values across all depths in Figure 8.10. Each detonation was

considered as an independent cycle of loading. Both the shear strain, as well as the r_u values demonstrate the differences between blast-induced ground motions, and ground motions associated with real earthquake sequences. In a real earthquake, the excess pore pressure ratio increases more slowly and over more cycles of loading. In contrast, the r_u values spike to above 60% on the first cycle of loading for both the blast detonations around the NP and the IP. The shear strains induced by blasting are also much larger per cycle than for a typical earthquake ground motion. The CSS from the blast test is on average larger than the typical earthquake CSS by between two or three orders of magnitude.

We plotted the cumulative CSS values with increasing r_u in Figure 8.11. Figure 8.11 shows that the cumulative shear strains caused by blasting in the NP and in the IP are essentially parallel. From Figure 8.11 it appears that the energy transmitted by the two blast sequences was approximately equal. It also appears that the RAP columns did not reduce the blast energy that was transmitted outside the treated area.

A secondary approach towards estimating shear strains is summarized by Kinney (2018). This method considers the effects of shear modulus degradation with changing excess pore pressure ratios. We used the measured r_u and accelerogram values to plot shear strains using this approach and plotted them in Figure A.2 in Appendix A. We did this in order to confirm that the magnitude of the shear strains between the two methods were consistent.

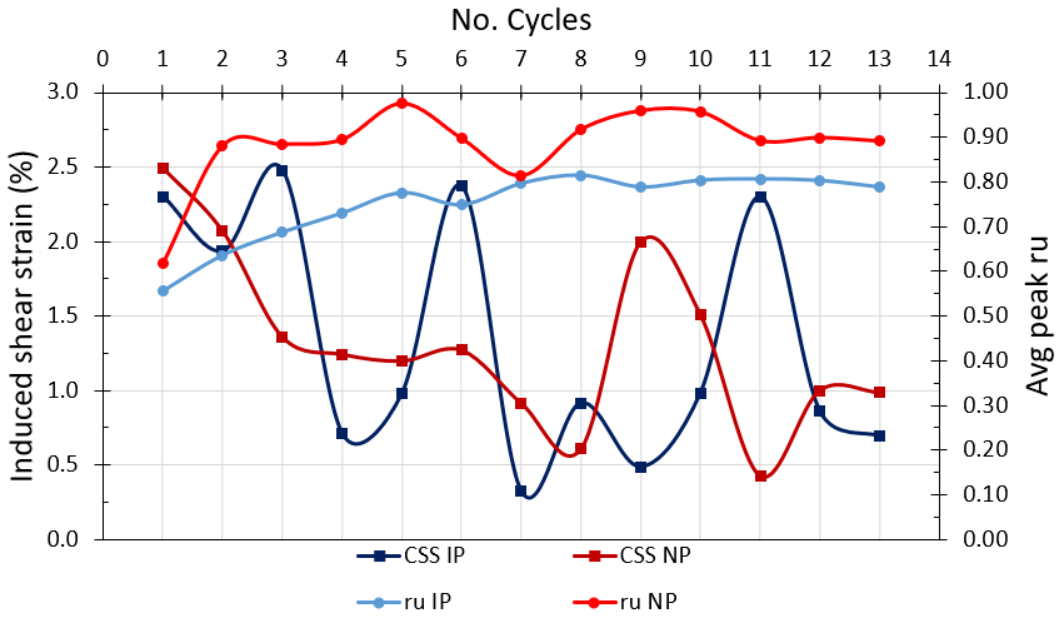

Figure 8.10: Incremental values of cyclic shear strain (CSS) and r_u during blast 1 (NP) and blast 2 (IP).

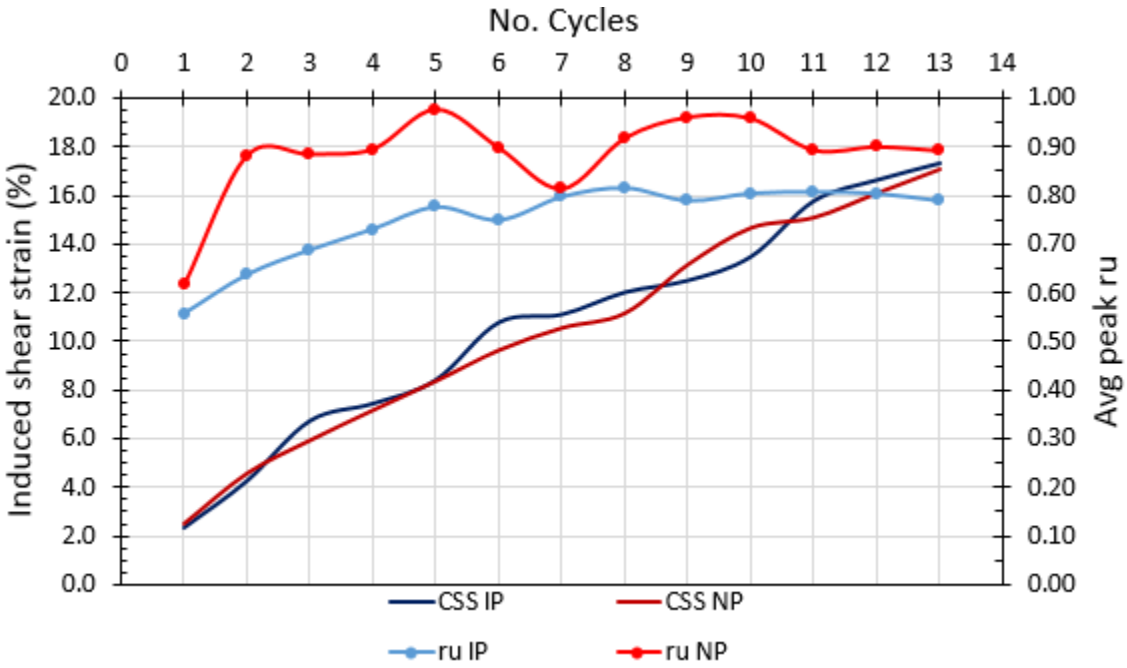

Figure 8.11: Cumulative CSS and r_u plotted against the number of cycles (blast detonations) during blast 1 (NP) and blast 2 (IP).

Using the constitutive relationship between shear stress and shear strain it is theoretically possible to use accelerogram records, along with values for the bulk and shear modulus of the soil, to estimate the induced shear stresses using the following procedure. First, the induced shear stress, τ is computed using the equation:

$$\tau = \frac{1}{2}(\sigma_r - \sigma_\theta) \tag{8.4.4}$$

where σ_r is the radial stress, and σ_θ is the tangential stress. Assuming the sand is subject to a spherically symmetrical three-dimensional loading, the radial and tangential stresses are given by the following equations:

$$\sigma_r = \rho * dR * \frac{a_1 + a_2}{2} \tag{8.4.5}$$

$$\sigma_\theta = \lambda * \varepsilon_r + 2(\lambda + G)\frac{u_r}{r} \tag{8.4.6}$$

where

$$\lambda = B - \frac{2}{3} \tag{8.4.7}$$

and where a is the acceleration recorded in the direction of the blast, u_r is the average displacement recorded by two independent accelerometers, r is the average radius from the blast source to the accelerometers, G is the shear modulus of the soil, and B is the bulk modulus water. The shear

modulus, G, was obtained from DMT correlations and were estimated as 38.4 MPa (5.6 ksi) and 14.7 MPa (2.1 ksi), respectively. Substituting equations 8.4.5 and 8.4.6 into 8.4.4, the shear stress is computed as:

$$\tau = \frac{3}{4}[\sigma_r - B\left(\varepsilon_r + \frac{2u_r}{r}\right)] \tag{8.4.8}$$

Once the cyclic shear stress is computed it can be normalized by the vertical effective stress to obtain the cyclic stress ratio (CSR). We computed the cyclic stresses for each of the blast charges using this procedure and they are plotted in Figure 8.13, which shows that the average induced shear stress was on the order of 0.1 to 0.55 MPa (0.01 to 0.08 ksi). Since the in-situ vertical effective stress at the depth of the accelerometers was between 45 and 60 kPa (.0087 ksi) the computed values of shear stress would result in CSR ratios between 1 and 9. The CRR ratios for the given soil are approximately 0.2. Given that the CSR is so much larger than the CRR, it is not known if the values for shear stress computed using this method are reliable at this time. The prospect of back-calculating CSR from blast testing has, to this point, not been effectively implemented in any research and would be of great benefit to the industry. This would mean that researchers could more reliably compare ground motions from blast charges to earthquake ground motions for liquefaction analyses. This research serves as another data point in the library of blast-induced liquefaction that can help propel this discovery.

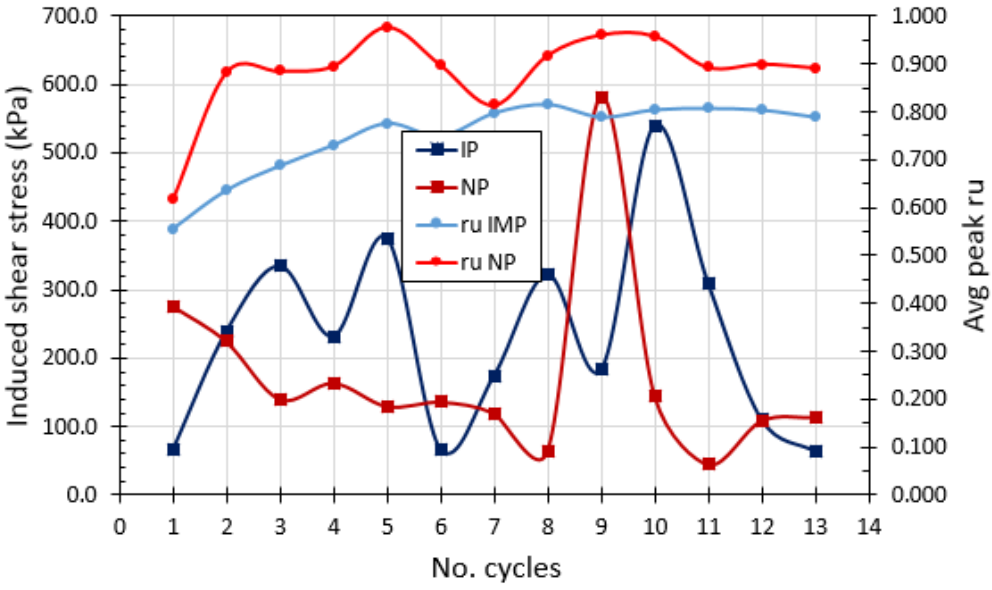

Figure 8.12: Induced shear stress from blast 1 (NP) and blast 2 (IP) with the average peak excess pore pressure ratio at additional cycle of loading.

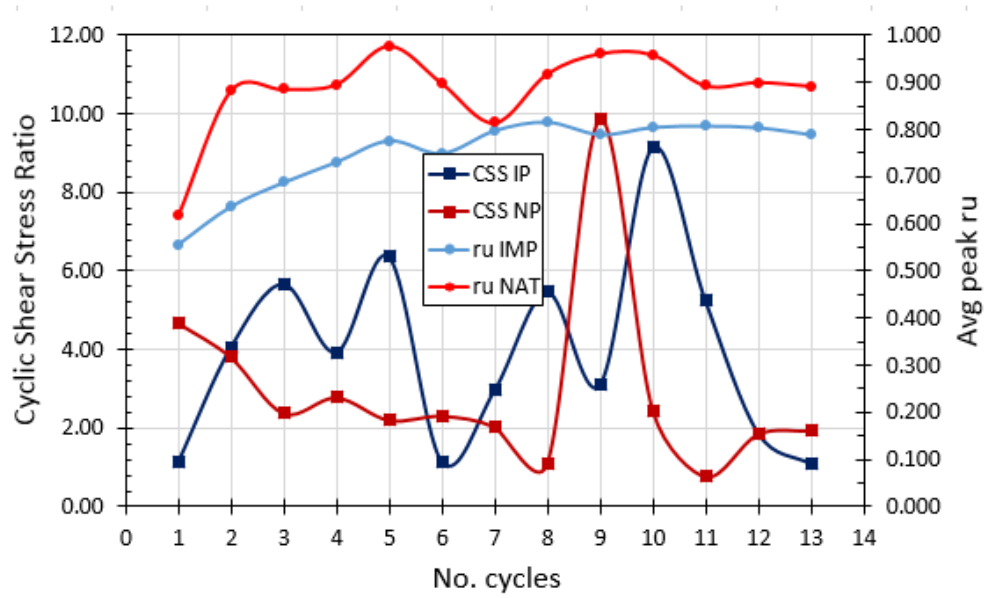

Figure 8.13: Cyclic stress ratio (CSR) from blast 1 (NP) and blast 2 (IP) with average peak excess pore pressure ratio at additional cycle of loading.

9 SUMMARY AND CONCLUSIONS

Full-scale blast-induced liquefaction tests were carried out in Bondeno, Italy to evaluate the effectiveness of Rammed Aggregate Pier (RAP) treatment in mitigating liquefaction hazards in silty sands. Tests were performed on treated and untreated panels at a test site where silty sands liquefied and produced numerous sand boils during the 2012 M_w 6.1 Emilia Romagna earthquake. The controlled blasting experiment was successful at inducing liquefaction in the liquefiable layer (3 m – 11 m) composed of natural untreated silty sands (FC ≈ 15-45%) and produced surface settlements of 70 to 100 mm along with several large sand boils. The consistent nature of the soil profile between the NP and the IP provided an excellent window for observing the mitigating effects of RAP improvement during liquefaction. RAP treatment increased the relative density and at-rest earth pressure coefficient for the silty sand. The improvement limited maximum settlement after improvement to less than 5 cm and reduced sand ejecta within the treated zone.

Based on analysis of the settlement data, the following conclusions can be drawn:

1. The blast energy imparted to the untreated, natural panel (NP), and the treated, improved panel (IP) produced ground motions that were similar to an equivalent earthquake of magnitude Mw=7.5 and PGA = 0.15 g.

2. Liquefaction-induced settlement in the NP was consistent with the computed settlement versus depth curve using the Zhang et al. (2002) approach assuming an appropriate factor of safety (0.93 in this case).

3. RAP installation densified the silty sand and increased the K_0 value, but r_u values of 80% still developed consistent with a liquefaction safety factor of 1.05 following blasting. However, computed liquefaction-induced settlement using the Zhang et al. (2002) significantly overestimated measured settlement when considering densification effects alone.

4. The measured settlement versus depth profile within the RAP treatment zone was reasonably well computed assuming that the RAPs and the surrounding sand resist elastic compression as a composite following pore pressure dissipation.

5. Downward shear along the RAP-sand composite transfers load to the base of the RAP columns which induces elastic settlement below the base of the RAPs.

6. Elastic compression from the toe of the RAP group appears to be consistent with settlement using elastic methods to account for settlement below the base of the RAPs.

7. The effects of K_0 are evident in the predictive FS_L for the design ground motions. While these effects are real, no direct relationship exists between K_0 and settlement predictions at this time.

This research experiment also demonstrates the need for further study of key areas such as the true effects of lateral earth pressures and quantifying these effects towards liquefaction settlement analyses. Also, further study is recommended to more accurately estimate blast-induced shear strains and stresses, and associated CSR, using accelerogram records.

REFERENCES

Alarcon-Guzman, A., Leonards, G.A., Chameau, J.L. 1988. "Undrained monotonic and cyclic strength of sands." *Journal of Geotechnical Engineering*, ASCE, 114(10): 1089-1109. https://doi.org/10.1061/(ASCE)0733-9410(1988)114:10(1089)

Alexander, G., Arefi, J., and Geoffrey, R. M. 2017. "Performance of a Stone Column Foundation System Subjected to Severe Earthquake Shaking." In, *Proc., 3rd International Conference on Performance-based Design in Earthquake Geotechnical Engineering – PBD-III,* Vancouver, British Columbia, Canada, July 16-19, 2017.

Amoroso, S., Rollins, K., Andersen, P., Gottardi, G., Tonni, L., Garcia Martinez, M., Wissman, K., Minarelli, L., Comina, C., Fontana, D., Marco De Martini, P., Monaco, P., Pesci, A., Sapia, V., Vassallo, M., Anzidei, M., Carpena, A., Cinti, F., Civico, R., Conforti, D., Doumaz, F., Giattanasio, F., Di Giulio, G., Foti, S., Loddo, F., Lugli, S., Manuel, M., Marchetti, D., Mariotti, M., Materni, M., Materni, V., Metcalfe, B., Milana, G., Pantosti, D., Pesce, A., Salocchi, A., Smedile, A., Stefani, M., Tarabusi, G., Teza, G. 2019. "Blast-induced liquefaction for full scale testing of ground improvement methods: Insights from a multidisciplinary study." *Engineering Geology* 265. https://doi.org/10.1016/j.enggeo.2019.105437

Amoroso, S., Rollins, K., Andersen, P., Gottardi, G., Tonni, L., Garcia Martinez, M.F., Wissman, K., Minarelli, L. 2018. "Full-Scale Testing of Liquefaction Mitigation using Rammed Aggregate Piers in Silty Sands." In, *Proc., 7th International Conference on Earthquake Geotechnical Engineering*, Rome, Italy, June 17-20, 2019.

Amoroso, S., Milana, G., Rollins, K., Comina, C., Minarelli, L., Manuel M., Monaco P., Franceschini, M., Anzidei, M., Lusvardi, C., Cantore, L., Carpena, A., Casadei, S., Cinti, F., Civico, R., Cox, B., Marco De Martini, P., Di Giulio, G., Di Naccio, D., Di Stefano, G., Facciorusso, J., Famiani, D., Fiorelli, F., Fontana, D., Foti, S., Madiai, C., Marangoni, V., Marchetti, D., Marchetti, S., Martelli, L., Mariotti, M., Muscolino, E., Pancalsdi, D., Pantosti, D., Passeri, F., Pesci, A., Romeo, G., Sapia, V., Smedile, A., Stefani, M., Tarabusi, G., Teza, G., Vassallo, M., Villani, F. 2016. "The first Italian blast-induced liquefaction test (Mirabello, Emilia-Romagna, Italy): description of the experiment and preliminary results." *Annals of Geophysics* 60(5): 19 pp. https://doi.org/10.4401/ag-7415

Andrus, R.D., Stokoe, K.H. 1997. "Liquefaction resistance based on shear wave velocity." NCEER Workshop on Evaluation of Liquefaction Resistance of Soils, Salt Lake City, UT, Technical Report NCEER-97-0022, T.L. Youd and I.M. Idriss, eds., National Center for Earthquake Engineering Research, Buffalo, NY, 89-128.

Andrus, R.D., Stokoe, K.H. 2000. "Liquefaction resistance of soils from shear wave velocity." *Journal of Geotechnical and Geoenvironmental Engineering*, ASCE, 126(11): 1015-1025. https://doi.org/10.1061/(ASCE)1090-0241(2000)126:11(1015)

Andrus, R.D., Stokoe, K.H., Juang, C.H. 2004. "Guide for Shear-Wave-Based Liquefaction Potential Evaluation." *Earthquake Spectra* 20(2). https://doi.org/10.1193/1.1715106

Babasaki, R., Suzuki, K., Saitoh, S., Suzuki, Y., and Tokitoh, K. 1991. "Construction and testing of deep foundation improvement using the deep cement mixing method." *Deep Foundation Improvements: Design Construction and Testing,* ASTM STP 1089, ASTM, Philadelphia, pp. 224-233.

Baziar, M.H., Dobry, R., and Elgamel, A.W.M. 1992. "Engineering evaluation of permanent ground deformations due to seismically-induced liquefaction." *Technical Report NCEER-92-0007,* National Center for Earthquake Engineering Research, State University of New York, Buffalo.

Brown, R.E. 1977. "Vibroflotation compaction of cohesionless soils." *Journal of Geotechnical and Geoenvironmental Engineering* 103(GT12): 1437-51.

Casagrande, A. 1976. "Liquefaction and cyclic mobility of sands: a critical review." *Harvard Soil Mechanics*, Boston Society of Civil Engineers, 1940, pp. 257-276.

Castro, G. 1969. "Liquefaction of sands." *PhD Dissertation,* Harvard University; reprinted as *Harvard Soil Mechanics Series*, 81: 112 pp.

Castro, G., Poulos, S.J. 1977. "Factors affecting liquefaction and cyclic mobility." *Journal of the Geotechnical Engineering Division*, ASCE, 106(GT6): 501-506.

Cetin, K.O., Seed, R.B., Der Kiureghian, A., Tokimatsu, K., Harder L.F., Kayen, R.E., Moss, R.E.S. 2004. "Standard penetration test-based probabilistic and deterministic assessment of seismic soil liquefaction potential." *Journal of Geotechnical and Geoenvironmental Engineering*, ASCE, 130(12): 1314-340.

Chang, K.T. 1978. “An Analysis of damage of Slope Sliding by Earthquake on the Paiho Main Dam and its Earthquake Strengthening.” *Tseng-hua Design Section*, Dept. of Earthquake-Resistant Design and Flood Control Command of Miyna Reservoir, Peoples Republic of China.

Coulter, M., Migliaccio, L. 1966. “Effects of the earthquake of March 27, 1964 at Valdez, Alaska.” *Professional Paper 542-C*, U.S. Geological Survey, U.S. Department of the Interior, Washington, D.C.

Cox, B.R., Stolte, A.C., Stokoe, K.H. II, Wotherspoon, L.M. 2018. “A Direct-Push Crosshole Test Method for the In-Situ Evaluation of High-Resolution P- and S-wave Velocity.” *Geotech. Test. J.,* 32 pp., First on line, doi: 10.1520/GTJ20170382.

D’Appolonia, E. 1954. “Loose Sands - Their Compaction by Vibroflotation.” in *Symposium on Dynamic Testing of Soils*, edited by Committee D-19 on Soils (West Conshohocken, PA: ASTM International, 1954), 138-162.

Demir, S., Ozener, P., Kirkit, M. 2017. “Experimental and Numerical Investigations of Behavior of Rammed Aggregate Piers.” *Geotechnical Testing Journal*, 40(3): 411-425.

Dobry, R., Ladd, R.S. 1980. Discussion to “Soil liquefaction and cyclic mobility evaluation for level ground during earthquakes.” by H.B. Seed and “Liquefaction potential: science versus practice,” by R.B. Peck, *Journal of the Geotechnical Engineering Division,* ASCE, 196(GT6): pp. 720-724.

Dobry, R., Ladd, R.S., Yokel, F.Y., Chung, R.M., Powell, D. 1982. “Prediction of pore water pressure buildup and liquefaction of sands during earthquakes by the cyclic strain method.” *NBS Building Science Series 138*, National Bureau of Standards, Gaithersburg, Maryland, 150 pp.

Dobry, R., MOhamad, R., Dakoulas, P., Gazetas, G. 1984. “Liquefaction evaluation of earth dams - a new approach.” *Proceedings, 8th World Conference on Earthquake Engineering*, Vol. 3, pp. 333-340.

Elvis, Ishimwe 2018. “Liquefaction-induced Dragload and/or Downdrag on Deep Foundations within the New Madrid Seismic Zone.” Doctoral dissertation, University of Arkansas, Fayetteville, Fayetteville, AR.

Emergeo Working Group. 2013. “Liquefaction phenomena associated with the Emilia earthquake sequence of May-June 2012 (Northern Italy).” *Natural Hazards and Earth System Sciences* 13 (4): 935-947.

Finn, W.D.L., Bransby, P.L., Pickering, D.J. 1970. "Effect of strain history on liquefaction of Sands." *Journal of the Soil Mechanics and Foundations Division*, ASCE, 96 (SM6): 1917-1934.

Fontana, D., Amoroso, S., Minarelli, L. & Stefani M. 2019. "Sand liquefaction phenomena induced by a blast test: new insights from composition and texture of sands (late Quaternary, Emilia, Italy)." *Journal of Sedimentary Research*, 89(1):13-27, https://doi.org/10.2110/jsr.2019.1

Fox, N.S. and Cowell, M.J. (1998). Geopier Foundation and Soil Reinforcement Manual. Geopier Foundation Company, Inc., Scottsdale, Arizona.

Geopier.com.2020. *Frequently Asked Questions*. Geopier US. [online] Available at: <https://www.geopier.com/FAQs> [Accessed 14 May 2020].

Golesorkhi, R., Seed, H.B. 1989. "Factors Influencing the Computational Determination of Earthquake-Induced Shear Stresses in Sandy Soils." Dept. of Civil and Environmental Engineering, University of California at Berkeley.

Green, R.A., Olgun, C.G., Wissmann, K.J. 2008. "Shear Stress Redistribution as a Mechanism to Mitigate the Risk of Liquefaction." *Journal of Geotechnical Earthquake. Engineering & Soil Dynamics*, ASCE, IV GSP 181.

Hanzawa, H., Itoh, Y., Suzuki, K. 1979. "Shear characteristics of a quick sand in the Arabian Gulf." *Soils and Foundations*, 19(4): 1-15.

Hwang, S., Roberts, J.N., Stokoe, K.H. II, Cox, B.R., van Ballegooy, S., Soutar, C. 2017. "Utilizing Direct-Push Crosshole Seismic Testing to Verify the Effectiveness of Shallow Ground Improvements: A Case Study Involving Low-Mobility Grout Columns in Christchurch, New Zealand." *Proceedings of Grouting 2017*, Honolulu, Hawaii, July 9-12, 2017, pp. 415-424.

Idriss, I.M. 1999. "An Update to the Seed-Idriss Simplified Procedure for Evaluating Liquefaction Potential." *Proc. of TRB Workshop on New Approaches to Liquefaction*, Federal Highway Administration, Washington D.C.

Idriss, I.M., Boulanger, R.W. 2004. "Semi-empirical procedures for evaluating liquefaction potential during earthquakes." *Proc., 11th International Conf. on Soil Dynamics and Earthquake Engineering, and 3rd International Conf. on Earthquake Geotechnical Engineering*, D. Doolin et al., eds., Stallion Press, Vol. 1, pp. 32-56.

Idriss, I.M., Boulanger, R.W. 2007. "SPT- and CPT- Based Relationships for the Residual Shear Strength of Liquefied Soils." *Earthquake Geotechnical Engineering*, pp. 1-22.

Idriss, I.M., Boulanger, R.W. 2007. "Residual shear strength of liquefied soils." 27th USSD Annual Meeting, March.

Idriss, I.M., Boulanger, R.W. 2008. "Liquefaction-Induced Ground Deformations Evaluation Based on Cone Penetration Tests (CPT)." *EERI Publication*, Monograph MNO-12, Earthquake Engineering Research Institute, Oakland, California.

Idriss, I.M., Boulanger, R.W. 2014. "CPT and SPT Based Liquefaction Triggering Procedures." *Center for Geotechnical Modeling*, Report No. UCD/CGM-14/01, Dept. of Civil and Environmental Engineering, University of California at Davis.

Ishihara, K., Tatsuoka, F., Yasuda, S. 1975. "Undrained deformation and liquefaction of sand under cyclic stresses." *Soils and Foundations*, 15(1): 29-44.

Ishihara, K. 1984. "Post-earthquake failure of a tailings dam due to liquefaction of the pond Deposit." *Proceedings, International Conference on Case Histories in Geotechnical Engineering*, University of Missouri, St. Louis, Vol. 3, pp. 1129-1143.

Ishihara, K. 1985. "Stability of natural deposits during earthquakes." *Proceedings, 11th International Conference on Soil Mechanics and Foundation Engineering*, Vol. 1, pp 321-376.

Ishihara, K., Yoshimine, M. 1992. "Evaluation of settlements in sand deposits following liquefaction during earthquakes." *Soils and Foundations*, 32(1): 173-188.

Ishihara, K. 1993. "Liquefaction and flow failure during earthquakes." *Geotechnique*, Vol. 43, No. 3, pp. 351-415.

Jamiolkowski, M., Ladd, C.C., Germaine, J.T., Lancellotta, R. 1985. "New developments in field and laboratory testing of soils." *Proc. of the 11th International Conf. on Soil Mechanics and Foundation Engineering*, San Francisco, CA.

Jamiolkowski M., Lo Presti D.C.F. & Manassero M. 2003. "Evaluation of Relative Density and Shear Strength of Sands from Cone Penetration Test and Flat Dilatometer Test." *Soil Behaviour and Soft Ground Construction*; GSP 119: 201-238.Majchrzak, M., Farrell, T. & Metcalfe, B. 2009.

Janes, H.W. 1973. "Densification of sand for drydock by Terra-probe." *Journal of the Soil Mechanics and Foundations Division*, ASCE, 99(SM6): 451-470.

Kayen, R.E., Mitchell, J.K., Seed, R.B., Lodge, A., Nishio, S., Cotinho, R. 1992. "Evaluation of SPT-, CPT-, and shear wave-based methods for liquefaction potential assessment using Loma Prieta data." *Proceedings, 4th U.S. - Japan Workshop on Earthquake Resistant Design of Lifeline Facilities and Countermeasures for Soil Liquefaction*, Vol. 1, pp. 177-204.

Kimmerling, Robert E. 1994. "Blast Densification for Mitigation of Dynamic Settlement and Liquefaction." *Report WA-RD 348.1*. Washington (State) Department of Transportation. Olympia, Washington, USA, March 1994.

Kinney, Landon Scott 2018. "Pore Pressure Generation and Shear Modulus Degradation during Laminar Shear Box Testing with Prefabricated Vertical Drains." Master Thesis, Brigham Young University, Provo, UT.

Kishida, H. 1967. "Ultimate bearing capacity of piles driven into loose sand." *Soils and Foundations*, 7(3): 20-29.

Kramer, S.L. 1996. *Geotechnical Earthquake Engineering*, Prentice Hall, Inc., Upper Sadle River, NJ, 653 pp.

Kramer, S.L., and Seed, H.B. 1988. "Initiation of soil liquefaction under static loading condition." *Journal of Geotechnical Engineering,* ASCE, 114(4): 412-430.

Ladd, R.S. 1974. "Specimen preparation and liquefaction of sands." *Journal of the Geotechnical Engineering Division*, ASCE, 100(GT10): 1180-1184.

Lawton, E., Warner, B. 2004. "Performance of a Group of Geopier Elements Loaded in Compression Compared to Single Geopier Elements and Unreinforced Soil." Final Report No. UUCVEEN 04-12, University of Utah, Salt Lake City, UT.

Majchrzak, M., Farrell, T. & Metcalfe, B. 2009. *Soft Ground Construction*; GSP 119: 201-238.

Marchetti, S. 1980. "In-Situ Tests by Flat Dilatometer." *Journal of the Geotechnical Engineering Division*, 1979, 106(3): 299-321.

Marchetti, S. 1982. "Detection of liquefiable sand layers by means of quasi-static penetration tests." *Proc., 2nd Europoean Symp. on Penetration Testing*, Amsterdam, pp. 689-695.

Marchetti, S., Monaco, P., Totani, G., Calabrese, M. 2001. "The Flat Dilatometer Test (DMT) in soil investigations – A Report by the ISSMGE Committee TC16."

Marcusson, W.F. III, Hynes, M.E. 1990. "Stability of slopes and embankments during earthquakes." *Proceedings, ASCE/Pennsylvania Department of Transportation Geotechnical Seminar,* Hershey, Pennsylvania.

Mayne, P.W. 2016. "Evaluating effective stress parameters and undrained shear strength of soft-firm clays from CPT and DMT." *Australian Geomechanics Journal* 51 (4): 27-55.

Meletti C., Galadini F., Valensise G., Stucchi M., Basili R., Barba S., Vannucci G., Boschi E.; 2008: A seismic source zone model for the seismic hazard assessment of the Italian territory. Tectonophysics, 450, 85– 108.

Mitchell, J.K. 1982, Soil improvement state of the art, Proc.10th Intl. Conf. on Soil Mech. And Foundation Engrg., ICSMFE, Vol. 4: 509-565.

Mitchell, J.B. 1995. "Performance of improved ground during earthquakes." In R. Hryciw (Ed.), *Soil Improvement for Earthquake Hazard Mitigation*, 1-36. San Diego, CA, ASCE Convention.

Muhunthan, B., Vijayathasan, N.V., Abbasi, B. 2017. "WA-RD 865.1: Liquefaction-Induced Downdrag on Drilled Shafts." Washington State Department of Transportation.

Mulilis, J.P., Chan, C.K., Seed, H.B. 1975. "The effects of method of sample preparation on the cyclic stress-strain behavior of sands." *Report EERC 75-18*, Earthquake Engineering Research Center, University of California, Berkeley.

Nagase, H., Ishihara, K. 1988. "Liquefaction-induced compaction and settlement of sand during earthquakes." *Soils and Foundations*, 28(1): 65-76.

Narin van Court, W.A. 1997. "Investigation of the mechanisms and predictive methodologies for explosive compaction." *Civil and environmental engineering*, Univ. of California at Berkeley, Berkeley, Calif.

Olsen, R.S. 1997. "Cyclic Liquefaction based on the Cone Penetrometer Test." *Proceedings of the NCEER Workshop on Evaluation of Liquefaction Resistance of Soils*, Technical Report NCEER-97-0022, edited by T. Leslie Youd and Izzat M. Idriss, National Center for Earthquake Engineering Research, State University of New York at Buffalo, Buffalo, NY, pp. 225-276.

Olson, S.M., Stark, T. 2002. "Liquefied strength ratio from liquefaction flow failure case Histories." *Canadian Geotechnical Journal*, Vol. 39, pp. 629-647.

Olson, S.M., Stark, T.D. 2003. "Yield strength ratio and liquefaction analysis of slopes and embankments." *Journal of Geotechnical and Geoenvironmental Engineering,* ASCE 129(8):727-737.

Ohsaki, Y. 1969. "The effects of local soil conditions upon earthquake damage." *Proceedings of Specialty Session 2*, *7th International Conference on Soil Mechanics and Foundation Engineering*, Mexico City.

Poulos, S.J. 1981. "The steady state of deformation." *Journal of the Geotechnical Engineering Division*, ASCE, 107(GT5): 553-562.

Poulos, S.J., Castro, G., and France, J.W. 1985. "Liquefaction evaluation procedure." *Journal of Geotechnical Engineering*, ASCE, 111(6): 772-792.

Priebe, Heinz J. 1995. "The Design of vibro replacement." *Ground Engineering*, 28(10): 31-37.

Priebe, H.J. 1995. "The design of vibro replacement." *Ground Engineering: 31-46*.

Priebe, H.J. 1998. "Vibro replacement to prevent earthquake induced liquefaction." *Ground Engineering*, London.

Priebe, H.J. 2001. "Vibro Replacement – Design Criteria and Quality Control." *Deep Foundation Improvements: Design, Construction, and Testing*, *ASTM STP 1089*, ASTM, Philadelphia.

Rayamajhi, Deepak & Tamura, Shuji & Khosravi, Mohammad & Boulanger, Ross & Wilson, Daniel & Ashford, Scott & Olgun, Guney. (2015). Dynamic Centrifuge Tests to Evaluate Reinforcing Mechanisms of Soil-Cement Columns in Liquefiable Sand. Journal of Geotechnical and Geoenvironmental Engineering. 141. 04015015. 10.1061/(ASCE)GT.1943-5606.0001298.

Regione Emilia-Romagna, Servizio Geologico Sismico e dei Suoli, ENI-AGIP 1998. Riserve idriche sotterranee della Regione Emilia-Romagna, scala 1:250.000, Bologna (in Italian).

Reyna, F., Chameau, J.L. 1991. "Dilatometer based liquefaction potential of sites in the Imperial Valley." *Proc., 2nd International Conference on Recent Advances in Geotechnical Earthquake Engineering and Soil Dynamics*, St. Louis, Missouri, Vol. 1, pp. 385-392.

Reynolds, O. 1885. “On the dilatancy of media composed of rigid particles in contact.” *Phil. Mag.,* Vol. 20, pp. 469-81.

Robertson, P.K. 2004. “Evaluating Soil Liquefaction and Post-earthquake deformations using the CPT.” *Proceedings, 2nd Geotech. Geophys. Site Charact., ISC ‘3,* Millpress, Rotterdam, 1:233-252.

Robertson, P.K. 2007. “Seismic Design for Liquefaction.” https://www.cpt-robertson.com/PublicationsPDF/seisdesign_liq07.pdf

Robertson, P.K. 2009. “Performance based earthquake design using the CPT.” *Proceedings, IS-Tokyo 2009*, June 2009, Tokyo, Japan.

Robertson, P.K., Campanella, R.G., Wightman, A. 1983. “SPT-CPT Correlations.” *Journal of Geotechnical Engineering*, 109(11): 1449-1459.

Robertson, P.K., Campanella, R.G., Wightman, A. 1986. “Estimating liquefaction potential of sands using the flat dilatometer.” *Geotechnical Testing Journal*, ASTM, 9(1): 38-40.

Robertson, P.K., Woeller, D.J., Finn, W.D.L. 1992. “Seismic Cone Penetration Test for Evaluation Liquefaction Potential under Cyclic Loading.” *Canadian Geotechnical Journal*, 29(3): 686-695.

Robertson, P.K., Wride, C.E. 1998. “Seismic Soil Liquefaction for Deterministic and Probabilistic Approach Based on in Situ Test (CPTU) Data.” *Canadian Geotechnical Journal*, Vol. 35, pp. 442-459.

Robertson, P.K., Cabal, K.L. 2015. “Guide to Cone Penetration Testing for Geotechnical Engineering.” 6th Edition, Gregg Drilling & Testing, Inc.

Robertson, P.K. & Wride, C.E. 1998. “Evaluating cyclic liquefaction potential using the cone penetration test.” *Canadian Geotechnical Journal* 35(3): 442-459.

Robinsky, E.I., Morrison, D.E. 1964. “Sand displacement and compaction around model friction piles.” *Canadian Geotechnical Journal*, 1(2): 81

Rollins, K.M., Price, B.E., Dibb, E., Higbee, J., 2006, Liquefaction mitigation of silty sands in Utah using stone columns with wick drains. Procs. GeoShanghai Intl. Conf, Geotechnical Special Publication 152, Ground Modification and Seismic Mitigation, ASCE, 343-348.

Rollins, K.M., Strand, S.R. 2006. "Downdrag forces due to liquefaction surrounding a pile." *Proceedings 8th US National Conference on Earthquake Engineering*, San Francisco, CA, paper 1646.

Rollins, K.M., Wright, A., Sjoblom, D., White, N., Lange, C. 2012. "Evaluation of liquefaction mitigation with stone columns in interbedded silts and sands." *Proceedings, 4th International Conference on Geotechnical and Geophysical Site Characterization*, Taylor and Francis Group, London, Vol. 2, p. 1469-1475.

Ryan, C.R., and Jasperse, B.H. 1989. "Deep soil mixing at the Jackson Lake Dam." in *Foundation Engineering: Current Principles and Practices*, Geotechnical Special Publication 22, ASCE, New York, Vol. 1, pp. 354-367.

Saftner et al, D.A., Zheng, J., Green, R.A., Hryciw, R., Wissman, K. 2018. "Rammed aggregate pier installation effect on soil properties." *Institution of Civil Engineers-Ground Improvement; Proc.* 171(2):63-73. London: ICE Publishing.

Seed, H.B. 1979. "Soil liquefaction and cyclic mobility evaluation for level ground during Earthquakes." *Journal of the Geotechnical Engineering Division*, ASCE, 106(GT6): 724.

Seed, H.B. 1986. "Design Problems in Soil Liquefaction." *Journal of Geotechnical Engineering*, ASCE, 113(8): 827-845.

Seed, H.B., Booker, J.R. 1977. "Stabilization of potentially liquefiable sand deposits using gravel Drains." *Journal of the Geotechnical Engineering Division, ASCE* 103(GT7): 757-768.

Seed, H.B., and De Alba, P. 1986. "Use of SPT and CPT tests for evaluating the liquefaction resistance of soils." *Proceedings*, *In Situ '86*, ASCE.

Seed, H.B., and Harder, Leslie F. 1990. "SPT-Based Analysis of Cyclic Pore Pressure generation and Undrained Residual Strength." *Proceedings, H.B. Seed Memorial Symposium,* Bi-Tech Publishing Ltd., Vol. 2, pp. 351-376.

Seed, H.B., Idriss, I.M. 1971. "Simplified procedure for evaluating soil liquefaction potential." *Journal of the Soil Mechanics and Foundation Division*, ASCE, 107(SM9): 1249-1274.

Seed, H.B., Idriss, I.M., Makdisi, F., Banerjee, N. 1975. "Representation of irregular stress time histories by equivalent uniform stress series in liquefaction analyses." *EERC 75-29,* Earthquake Engineering Research Center, University of California, Berkeley.

Seed, H.B., Idriss, I.M. 1982. *Ground Motions and Soil Liquefaction During Earthquakes,* Earthquake Engineering Research Institute, Berkeley, California, 134 pp.

Seed, H.B., Idriss, I.M., Arango, I. 1983. "Evaluation of liquefaction potential using field performance data." *Journal of Geotechnical Engineering*, ASCE, 109(3): 458-482.

Seed, H.B., Lee, K.L. 1966. "Liquefaction of saturated sands during cyclic loading." *Journal of the Soil Mechanics and Foundations Division*, ASCE, 92(SM3): 25-58.

Seed, H.B., Peacock, W.H. 1971. "Test procedures for measuring soil liquefaction characteristics." *Journal of the Soil Mechanics and Foundations Division*, ASCE, 97(SM8): 1099-1119.

Seed, R.B., Riemer, M.F., Dickenson, S.E. 1991. "Liquefaction of Soils in the 1989 Loma Prieta Earthquake." *Proc: 2nd International Conf. on Recent Advances in Geotechnical Earthquake Engineering and Soil Dynamics,* March 11-15, 1991, St. Louis, Missouri, Paper No. Lp02.

Silver, N.L., Seed, H.B. 1971. "Volume changes in sands during cyclic loading." *Journal of the Soil Mechanics and Foundations Division*, ASCE, 97(SM9): 1171.

Smith, M., Wissmann, K. 2018. "Ground Improvement Reinforcement Mechanisms Determined for the M_w 7.8 Muisne, Ecuador, Earthquake." *Geotechnical Earthquake Engineering and Soil Dynamics V*, June 10-13.

Solymar, Z.V., Reed, D.J. 1986. "A comparison of foundation compaction techniques." *Canadian Geotechnical Journal*, 23(3): 271-280.

Studer, J., Kok, L. 1980. "Blast-induced excess porewater pressure and liquefaction; experience and application." *International Symposium on Soils Under Cyclic and Transient Loading*, Swansea, U.K., 1980, Proceedings, v. 1, pt. 2, p. 581-593.

Suzuki, Y., Tokimatsu, K., Koyamada, K., Taya, Y., Kubota, Y. 1995. "Field correlation of soil liquefaction based on CPT data." *Proceedings of the International Symposium on Cone Penetration Testing*, Linkoping, Sweden, Vol. 2, pp. 583-588.

Sykora, D.W. 1987. "Creation of a data base of seismic shear wave velocities for correlation analysis." *Geotech. Lab. Miscellaneous Paper GL-87-26*, U.S. Army Engineer Waterways Experiment Station, Vicksburg, Miss.

Taki, D. and Yang, D.S. 1991. “Soil-cement mixed wall technique.” *Geotechnical Engineering Congress*, Geotechnical Special Publication 27, ASCE, New York, Vol. 1, pp. 298-309.

Tatsuoka, F., Ochi, K., Fujii, S., Okamoto, M. 1986. “Cyclic undrained triaxial and torsional shear strength of sands for different sample preparation methods.” *Soils and Foundations,* 26(3): 23-41.

Tatsuoka, F., Zhou, S., Sato, T., Shibuya, S. 1990. “Method of evaluating liquefaction potential and its application.” In *Report on seismic hazards on the ground in urban areas*, Ministry of Education of Japan, Tokyo (in Japanese).

Toki, S., Tatsuoka, F., Miura, S., Yoshimi, Y., Yasuda, S., Makihara, Y. 1986. “Cyclic undrained triaxial strength of sand by a cooperative test program.” *Soils and Foundations*, 26(3): 117-128.

Tokimatsu, K., Yoshimi, Y. 1983. “Empirical Correlation of Soil Liquefaction Based on SPT N-Value and Fines Content.” *Soils and Foundations*, 23(4): 56-74.

Tsai, P., Lee, D., Kung, G.T., Juang, C.H. 2009. “Simplified DMT-based methods for evaluation liquefaction resistance of soils.” *Engineering Geology*, Vol. 102: 13-22.

van Ballegooy, S., Malan, P., Lacrosse, V., Jacka, M.E., Cubrinovski, M., Bray, J.D., O'Rourke, T.D., Crawford, S.A. & Cowan, H. 2014. “Assessment of Liquefaction-Induced Land Damage for Residential Christchurch.” *Earthquake Spectra*, 30(1): 31-55.

Vasquez-Herrera, A., Dobry, R., Baziar, M.H. 1990. “Re-evaluation of liquefaction triggering and flow sliding in the Lower San Fernando Dam during the 1971 earthquake.” *Proceedings, 4th U.S. National Conference on Earthquake Engineering*, Palm Springs, California, pp.783-792.

Vasquez-Herrera, A., Dobry, R. 1988. “The behavior of undrained contractive sand and its effect on seismic liquefaction flow failures of earth structures.” *Report to U.S. Army Corps of Engineers*, Renssalaer Polytechnic Institute, Troy, New York, 510 pp.

Vautherin, E., Lambert, C., Barry-Macaulay, D., and Smith, M. 2017. “Performance of Rammed Aggregate Piers as a Soil Densification Method in Sandy and Silty Soils: Experience from the Christchurch Rebuild.” *Proceedings of 3rd International Conference on Performance-based Design in Earthquake Geotechnical Engineering* – PBD-III, Vancouver, British Columbia, Canada, July 16-19, 2017.

Vesic, A.S. 1977. *Design of Pile Foundations*, National Cooperative Highway Research Program Synthesis of Practice No. 42, Transportation Research Board, Washington, D.C.

Whitman, R.V. 1971. "Resistance of soil to liquefaction and settlement," *Soils and Foundations*, 11(4): 59-68.

Wissman, K., Fox, N., Martin, P. 2000. "Rammed Aggregate Piers Defeat 75-Foot Long Driven Piles." presented at the *Specialty Conference on Performance Confirmation of Constructed Geotechnical Facilities*, Amherst, Massachusetts, 9 April, pp. 198-210.

Wissmann, K. and Fox, N. 2000. "Design and Analysis of Short Aggregate Piers Used to Reinforce Soil for Foundation Support." presented at the *Geotechnical Colloquium,* Darmstadt, Germany, 25 March, Technical University Darmstadt, Darmstadt, Germany, pp. 1-10.

Wissman, K.J., Moser, K., Pando, M. 2001. "Reducing Settlement Risks in Residual Piedmont Soils Using Rammed Aggregate Pier Elements." *Proc. ASCE Specialty Conf.*, Blacksburg, Virginia, 9-13 June 2001.

Wissman, K.J., van Ballegooy, S., Metcalfe, B.C., Dismuke, J.N., Anderson, C.K. 2015. "Rammed aggregate pier ground improvement as liquefaction method in sandy and silty Soils." *6th International Conference on Earthquake Geotechnical Engineering, 6ICEGE: Proc. Intern. Conf.,* Christchurch, 1-4 November 2015.

Wissman, K.J., Moser, K., Pando, M. 2001. "Reducing Settlement Risks in Residual Piedmont Soils Using Rammed Aggregate Pier Elements." *Proc. ASCE Specialty Conf.*, Blacksburg, Virginia, 9-13 June 2001.

Wong, W. 1984. "Earthquake damages to earth dams and levees in relation to soil liquefaction and weakness in soft clays." *Proceedings, International Conference on Case Histories in Geotechnical Engineering*, Vol. 1, pp. 511-521.

Wotherspoon, L.M., Cox, B.R., Stokoe, K.H. II, Ashfield, D.J., Phillips, R.A. 2015. "Utilizing Direct-Push Crosshole Testing to Assess the Effectiveness of Soil Stiffening Caused by Installation of Stone Columns and Rammed Aggregate Piers." *Proceeding of 6th International Conference on Earthquake Geotechnical Engineering – 6ICEGE,* Christchurch, New Zealand, 1-4 November 2015.

Wu, J. 2002. "Liquefaction triggering and post liquefaction deformation of Monterey 0/30 sand under uni-directional cyclic simple shear loading." *PhD Dissertation*, University of California, Berkeley.

Yoshimi, Y., Tokimatsu, K., Hasaka, Y. 1989. "Evaluation of liquefaction resistance of clean sands based on high-quality undisturbed samples." *Soils and Foundations,* 29(1): 93-104.

Youd, T.L. 1972. "Compaction of sands by repeated shear straining," *Journal of the Soil Mechanics and Foundations Division*, ASCE, 98(SM7): 709-725.

Youd, T.L. 1973. "Liquefaction, flow, and associated ground failure." *Geological Survey Circular*, No. 688, U.S. Geological Survey.

Youd, T.L., Hoose, S.N. 1977. "Liquefaction susceptibility and geologic setting." *Proceedings, 6th World Conference on Earthquake Engineering*, New Delhi, Vol. 3, pp. 2189-2194.

Youd, T.L. 1984. "Recurrence of liquefaction at the same site." *Proceedings, 8th World Conference on Earthquake Engineering*, Vol. 3, pp. 231-238.

Youd, T.L. 1991. "Mapping of earthquake-induced liquefaction for seismic zonation." *Proceedings, 4th International Conference on Seismic Zonation*, Earthquake Engineering Research Institute, Stanford University, Vol. 1, pp. 111-147.

Zhang, G., Robertson, P.K., Brachman, R.W.I. 2002. "Estimating liquefaction-induced ground settlements from CPT for level ground." *Canadian Geotechnical Journal*, 39(5):1168-1180.

APPENDIX A. ADDITIONAL RESOURCES

Table A.1: Relationship between postliquefaction volumetric strain and equivalent clean sand normalized CPT tip resistance for different factors of safety (After Zhang et al, 2002).

[A1]	if FS ≤ 0.5,	$\varepsilon_v = 102(q_{c1N})_{cs}^{-0.82}$	for $33 \le (q_{c1N})_{cs} \le 200$
[A2]	if FS = 0.6,	$\varepsilon_v = 102(q_{c1N})_{cs}^{-0.82}$	for $33 \le (q_{c1N})_{cs} \le 147$
[A3]	if FS = 0.6,	$\varepsilon_v = 2411(q_{c1N})_{cs}^{-1.45}$	for $147 \le (q_{c1N})_{cs} \le 200$
[A4]	if FS = 0.7,	$\varepsilon_v = 102(q_{c1N})_{cs}^{-0.82}$	for $33 \le (q_{c1N})_{cs} \le 110$
[A5]	if FS = 0.7,	$\varepsilon_v = 1701(q_{c1N})_{cs}^{-1.42}$	for $110 \le (q_{c1N})_{cs} \le 200$
[A6]	if FS = 0.8,	$\varepsilon_v = 102(q_{c1N})_{cs}^{-0.82}$	for $33 \le (q_{c1N})_{cs} \le 80$
[A7]	if FS = 0.8,	$\varepsilon_v = 1690(q_{c1N})_{cs}^{-1.46}$	for $80 \le (q_{c1N})_{cs} \le 200$
[A8]	if FS = 0.9,	$\varepsilon_v = 102(q_{c1N})_{cs}^{-0.82}$	for $33 \le (q_{c1N})_{cs} \le 60$
[A9]	if FS = 0.9,	$\varepsilon_v = 1430(q_{c1N})_{cs}^{-1.48}$	for $60 \le (q_{c1N})_{cs} \le 200$
[A10]	if FS = 1.0,	$\varepsilon_v = 64(q_{c1N})_{cs}^{-0.93}$	for $33 \le (q_{c1N})_{cs} \le 200$
[A11]	if FS = 1.1,	$\varepsilon_v = 11(q_{c1N})_{cs}^{-0.65}$	for $33 \le (q_{c1N})_{cs} \le 200$
[A12]	if FS = 1.2,	$\varepsilon_v = 9.7(q_{c1N})_{cs}^{-0.69}$	for $33 \le (q_{c1N})_{cs} \le 200$
[A13]	if FS = 1.3,	$\varepsilon_v = 7.6(q_{c1N})_{cs}^{-0.71}$	for $33 \le (q_{c1N})_{cs} \le 200$
[A14]	if FS = 2.0,	$\varepsilon_v = 0.0$	for $33 \le (q_{c1N})_{cs} \le 20$

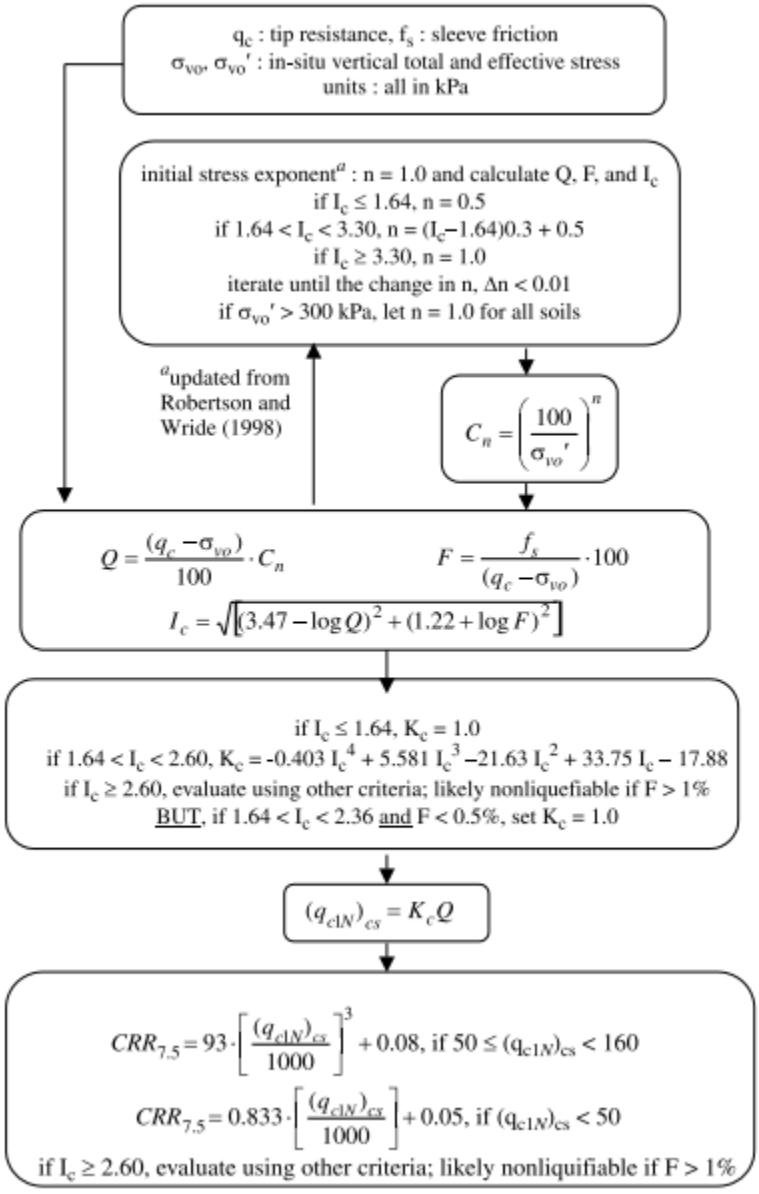

Figure A.1: Flowchart for evaluation of $CRR_{7.5}$ using Robertson and Wride (1998) CPT-based method (after Zhang et. al, 2002).

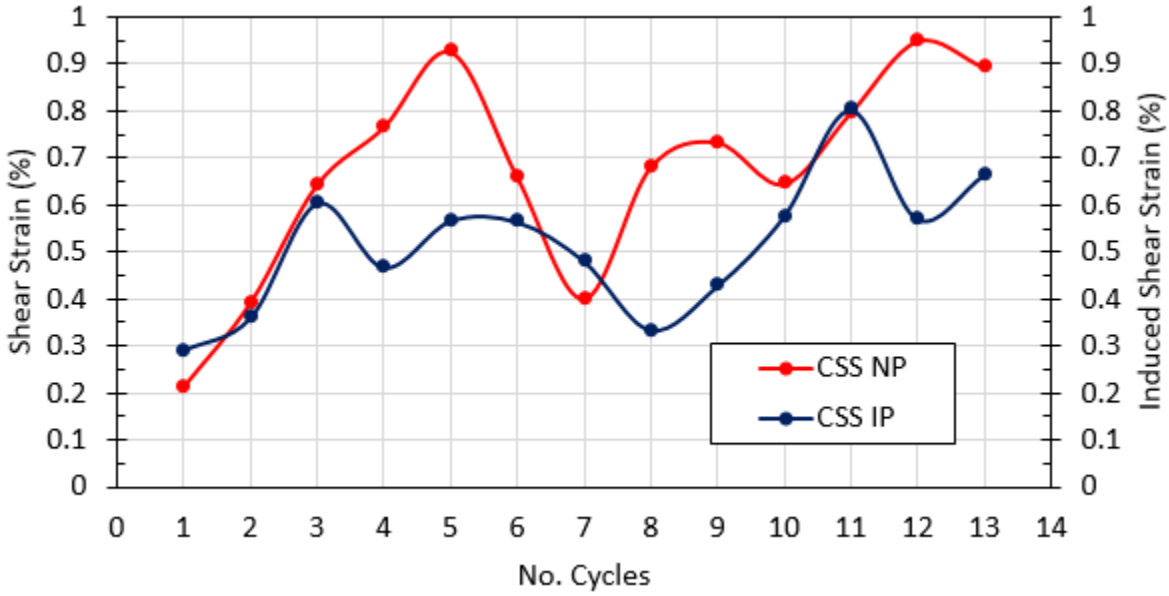

Figure A.2: Computed shear strain after the manner of Kinney (2018).